Advanced FBG fabrication for challenging applications

Steffan Keith Walters
Aston University
September 2018
MPhil

Summary

This thesis describes work performed for both advancing the fabrication process of fibre Bragg gratings and for a potential application for gratings inscribed by a system employing the improved methods. The aim of the discussed research is to increase the potential for fabricated grating variations whilst maintaining a grating accurate to the initial design and compensating for errors in fabrication. In addition, simulations for a system for detecting nanoparticles is sought, making use of the improvements to the fabrication setup and highlighting an example of the improved fabrication system's flexibility.

As a part of the development of the fabrication system, an increase in the efficiency of grating fabrication is a desired result, primarily via the reduction of grating iterations required to produce a high quality grating. To perform this, automated control of an optical vector analyser was created, for use in a feedback process in which the grating is observed during inscription and compared to simulations for the detection of fabrication errors. This will not only increase the likeness of gratings to their design but will also assist in repeatability of inscription by the system. Other improvements to the fabrication system have also been progressed, such as the inclusion of an optional interferometer inscription head and the ability to fabricate gratings of up to one metre in length. These two discussed factors will increase the flexibility of grating designs that can be written, enabling a greater variety of grating-based research to be available from a single fabrication setup.

Potential fabrication designs to demonstrate the capabilities of the system were investigated, leading to the development of a simulation for a nanoparticle detector. Observations of the transmission spectrum as nanoparticles pass through the beam path in an orthogonally aligned microchannel demonstrate alterations to the spectrum which may be used to identify the presence of nanoparticles and some select attributes. How the changes in the wavelength of a valley within the spectrum are affected by variations in parameters is overviewed as well as improvements to the simulations to further develop the accuracy to a physical detection system.

Keywords: *Fiber Bragg gratings, Fiber optics, Fiber optics sensors, Fiber Bragg gratings design and fabrication, Nanoparticles*

Contents

Abbreviations

AOM- Acoustic Optical modulator

AIPT- Aston Institute of Photonic Technologies

DUT- Device under test

FBG- Fibre Bragg grating

FWHM- Full width half maximum

LPG- Long period grating

OVA- Optical vector analyser

SMF- Single mode fibre

UV- Ultraviolet

WSS- Wavelength selective switch

VI- Virtual interface

List of Figures

1. Introduction

The introduction of fibre Bragg gratings (FBGs), first discovered by Hill in 1978 [1], had a great impact in many sectors, with many adaptations of their designs and fabrication techniques since their discovery. This progress has continued, with advances in recent years that have enabled some of the more advanced fabrication and sensor research discussed and performed in this report.

Such advanced fabrication calls for more developed techniques to inscribe gratings, building on methods already employed. Though work on improving individual setups has been continuous in literature, the development of a process to counter systematic and random errors in fabrication to increase the precision of fabrication and via this the flexibility of grating designs possible has not seen as much work.

This report covers a number of different research topics, mainly focussed around the improvement of the in house fabrication system, for both this system and in ways that can be used in different setups for reducing errors, as well as the development of simulations for a potential nanoparticle detection system. The production of a series of programs for controlling the measurement phase of a fabrication feedback technique, with the aim of providing an efficient method for probing the spectrum and sending this data to the rest of the feedback system for analysis. In addition to this, the construction of an interferometer inscription head for integrating into the existing fabrication system as an optional inscription head is covered, alongside further development of this via possible integration with the feedback system for greater control.

The potential for a nanoparticle detector, based on the alteration of transmission spectra due to the presence of nanoparticle passing through a microchannel across the fibre, is a development of research into creating microchannels through an optical fibre. This research makes use of a brief investigation into splitting longer grating designs into segments of fabrication also contained in this work. The potential for such a nanoparticle detector in applications such as virion detection and for electromagnetic field sensing (via the detection of a field-sensitive particle), guided the development of the simulation thus-far, with a description of what has been performed and what further additions and improvements could be made to the detector simulations

1.1. Summary of content

This dissertation comprises four chapters, of which the first introduces the topic of research. The second chapter reviews the theory behind the research, including a literature review of FBGs, as well as simulation and fabrication approaches. Aspects such as the fabrication techniques, the variations, advantages and disadvantages of them, as well as coupled mode theory are explored among other areas, providing a basis and justification for the research topics covered in this work.

The third chapter focusses on the research performed for this work, overviewing the fabrication setup employed, highlighting the constraints and improvements made to it. In particular, the addition of an optional inscription head and a fabrication feedback system are discussed. Following on from this, chapter three also covers the development of a simulation for a nanoparticle detection system following the logic of phase shifted gratings. A description of the setup and theory is provided prior to the simulations and a discussion of the results of these simulations and future work.

The fourth chapter concludes the dissertation, summarising the work performed and potential future work.

2. Introduction to fibre Bragg gratings

2.1. Optical fibres as waveguides

2.1.1. Brief history of waveguides

The ability for objects to guide light through them was first observed at the time of mankind's first use of glass. Though not their concern at the time, glass blowers would have observed this effect when blowing glass. Only by the 19th century did research turn to this phenomena to aid in the transmission of light over long distances [2].

The use of glass fibre was initially used as decorations as far back as 1600BC and was specialised in east Mediterranean countries [3], though the use of a blowpipe from around 50BC made the process faster, and more feasible to perform. Such a use for glass fibre was the norm up to the 18th century, where the use of more complex decorations and spinning it into fabric was performed [2].

Waveguides specifically for the purpose of guiding light were initially used by scientists during lectures as a method to dazzle audiences, usually by using cascades of water to trap light within using total internal reflection. Progressing from this, glass rods were used to guide light into otherwise constrained areas in medical fields, having the distinct advantage in comparison to other light sources of not heating the area lit as the fibre did not transmit heat.

Beyond primitive methods such as smoke signals, the first use of light for communication over large distances was via telegraphs, developing signal modulation via frequency and amplitude. Following the discovery that light and radio signals are different frequencies of electromagnetic waves, the dependence of the frequency of the carrier was identified as a key aspect of the communication's capacity and, in the 20th century, that light could provide a great capacity for telecommunications [2].

Optical waveguide filters were first observed following exposure of the core of a Germanium doped optical fibre to an argon ion laser by Hill in 1978 [1], forming a fibre grating. Following this discovery research into fibre Bragg gratings proceeded, with a focus on photosensitivity in doped optical fibre, leading to Sasaki's discovery of sum frequency generation by use of a YAG laser [4]. Stone continued the research into fibre sensitivity by demonstrating the sensitivity of most fibre to argon laser radiation [5].

2.1.2. Optical fibres

Optical fibres are dielectric waveguides, guiding light down their length via total internal reflection. Usually made of either glass or plastic, the fibre's structure is divided into a core and a cladding, each of different refractive indexes. As the cladding of the fibre is designed to have a lower refractive index than the core, the light passing through the fibre is trapped within the core of the fibre via total internal reflection, presuming the light enters the fibre longitudinally.

In general, the core and cladding boundary has a noticeable difference in refractive index, known as a step index fibre [6]. This drop in refractive index from the core to the cladding and then to the surroundings is one of the more common fibre structures and relies on Snell's law in points where a mode of the inbound light passes near the core-cladding boundary.

Alternatively, the refractive index can be made to change gradually from the core to the cladding in a structure known as a graded-index fibre. In this case, the gradual change in refractive index causes the inbound light's modes to be internally reflected more gradually.

Other aspects that can be altered in fibre designs include the diameter of the core. Described in more detail below, an increase in core diameter will enable more modes of the inbound light to propagate through the fibre.

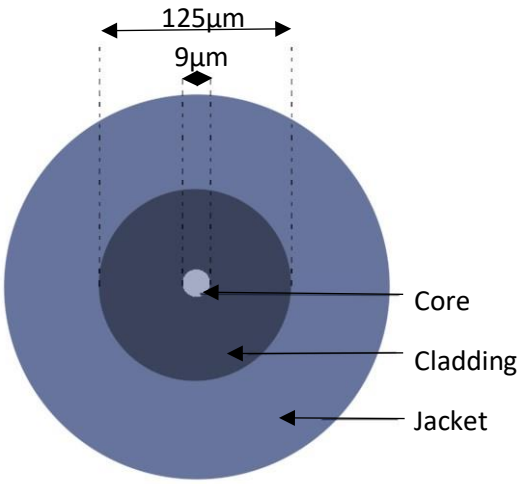

Fig. 2.1: Cross-sectional diagram of an SMF28 optical fibre, the most commonly used fibre within this thesis.

2.1.3. Fibre and Grating modes

Light propagating through an optical fibre can do so in varying ways, dependent on the structure of the fibre. Each of these different propagation 'paths' forms a time independent and spatial distribution of optical energy that may occur in one or more dimensions, known as a mode. The number of modes, as well as which modes propagate, is mainly dependent on the radius of the fibre core, with single mode fibres having relatively thin cores of roughly 8µm in diameter and a cladding of 125µm diameter. Multimode fibre on the other hand has a much larger core of 50-100µm, enabling more modes to travel through the fibre.

The main difference between single and multimode fibres as a result of the diameter change is the number of modes that may propagate through the fibre. In general, single mode fibre will only enable the transmission of a single mode, though an exception does exist. Should two modes occur along the same 'path' with orthogonal polarisations, then it is possible for both modes to propagate through a single mode fibre [7].

As the name implies, multimode fibres allow the transmission of multiple modes through them. As a result of the larger core diameter, some modes passing though the fibre may travel more directly than others, resulting in them travelling a larger distance through the fibre's length than less direct modes. This varying in propagation velocities results in modes spreading out over the course of transmission and a distortion of the signal. This dispersion can be compensated for via alterations to the core, including the use of fibre gratings and is discussed among the applications for fibre Bragg gratings.

There are several means of modelling the propagation of modes through a fibre, including ray optics, though this report makes use of coupled mode theory for this task. As much of the use of coupled mode theory in this report is related to its use with gratings, a full description shall be provided in section 2.3.

In terms of the propagation of light through a plain optical fibre, the interaction of modes is dependent on the phase matching condition for the copropagating and counterpropagating modes. This is dependent on the propagation constant of the boundwave generated by a material's polarisation response, β [8]. Groupings of modes can be determined by β and can be referred to as core, cladding and radiation modes.

When the phase matching condition of $\frac{n_{cl}}{\lambda} < \beta < \frac{n_{co}}{\lambda}$ is met, with n_{cl} and n_{co} are the refractive indices of the cladding and core respectively, the modes with polarisation modes matching this remain exclusively in the core. These core modes are not limited to copropagation, but may be counterpropagating, as long as they remain within the core. Similarly, cladding modes exist under a phase matching condition of $\frac{n_{air}}{\lambda} < \beta < \frac{n_{cl}}{\lambda}$, though they occur in the same propagation direction as the light. Cladding modes not only interact with other cladding modes but may also interact with core modes. Should the phase matching condition fall within $\beta < \frac{n_{air}}{\lambda}$, modes may be coupled into the fibre's surroundings from the cladding. As an often negligible proportion of modes entering the surroundings re-enter the fibre, this is usually considered as a loss, with fibres being designed to minimise this occurrence.

In the presence of a grating, the core to cladding mode interaction can be treated by considering the coupling of the core mode with multiple cladding modes at a given wavelength simultaneously [9]. Erdogan describes that only the coupling modes between the core and cladding that are nonzero involve cladding modes with an azimuthal order l=1. The equations presented within [9] consider the coupling of the LP_{01} core mode to itself, as is the case for counterpropagating modes, as well as co-propagating cladding modes with l=1.

$$\frac{dA^{co}}{dz} = iq_{01-01}^{co-co}A^{co} + i\frac{m}{2}q_{01-01}^{co-co}B^{co}exp(-2i\delta_{01-01}^{co-co}z) + i\sum_{\mu}\kappa_{1\mu-01}^{cl-co}B_{\mu}^{cl}exp\left(-2i\delta_{1\mu-01}^{cl-co}z\right) \quad (2.1)$$

$$\frac{dB^{co}}{dz} = -iq_{01-01}^{co-co}B^{co} - i\frac{m}{2}q_{01-01}^{co-co}A^{co}exp(2i\delta_{01-01}^{co-co}z) \quad (2.2)$$

$$\sum_{\mu}\left[\frac{dB^{co}}{dz} = -i\kappa_{1\mu-01}^{cl-co}A^{cl}exp\left(2i\delta_{1\mu-01}^{cl-co}z\right)\right] \quad (2.3)$$

Where A^{co} and B^{co} are the amplitudes for the core mode and B_{μ}^{cl} is the amplitude for the μ^{th} cladding mode. q_{01-01}^{co-co} and $\kappa_{1\mu-01}^{cl-co}$ respectively describe the coupling coefficient for the LP_{01} core modes and the cross coupling coefficient for the LP_{01} core mode with the μ^{th} cladding mode. More detail on coupling coefficients are given in section 2.3. 0≥m≥1 is the induced fringe modulation in the grating. δ describes the detuning parameter corresponding to [9]:

$$\delta_{01-01}^{co-co} = \frac{1}{2}\left(2\beta_{01}^{co} - \frac{2\pi}{\Lambda}\right) \quad (2.4)$$

$$\delta_{1\mu-01}^{cl-co} = \frac{1}{2}\left(\beta_{01}^{co} + \beta_{1\mu}^{cl} - \frac{2\pi}{\Lambda}\right) \quad (2.5)$$

Where β is the polarisation response (with $\beta=(2\pi/\lambda)n_{eff}$) and Λ is the grating period. These equations hold for wavelengths that provide near-zero detuning for the grating period specified. Based on this

detail, it can be stated that the wavelength at which $\delta_{01-01}^{co-co} = 0$ is the Bragg wavelength and the wavelength at which $\delta_{1\mu-01}^{cl-co} = 0$ is the resonant wavelength for the core to μ^{th} cladding mode coupling [9, 10].

2.2. Fibre Bragg gratings

Since the discovery of fibre Bragg gratings in 1978 [1], the development of gratings for use as sensors and advanced wavelength filters has propelled research into optical fibre technology. Fibre Bragg gratings are sections within an optical fibre which contain a pattern of perturbations in the fibre's refractive index.

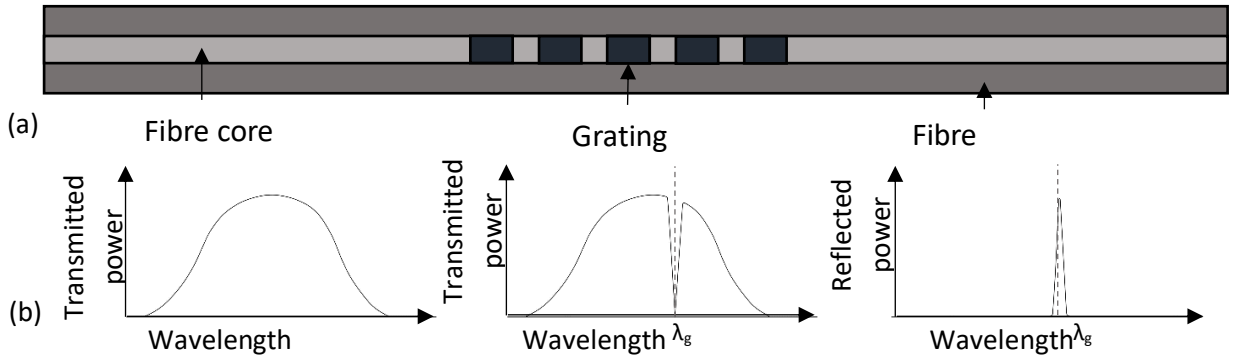

Fig. 2.2: The basic structure of a fibre Bragg grating (a), and diagrams of the affected spectra's power for a grating design (b) with an unmodified fibre (left), the transmitted spectrum through an example grating (centre) and the reflected spectrum due to a grating (right). The target wavelength of the grating is displayed with a dashed line.

Based on the design of the patterns, particular wavelengths can be targeted, with a dependency on aspects such as the physical spacing and length of each perturbed section as well as features such as apodisation and resolution of the design affecting the transmitted and reflected spectra over the course of the grating. The flexibility of grating designs, and therefore applications, has led to a great deal of research regarding potential uses for FBGs and more advanced methods for fabricating them.

A fibre Bragg grating is comprised of a series of fibre sections over a length of fibre with a perturbed refractive index in the core, with a simple pattern displayed in figure Fig. 2.2a. At each boundary a fraction of the inbound light is reflected (via Fresnel Reflection), with each of these coherently combining over the length of the whole grating to form a large reflection. The central wavelength of this reflected spectra is dependent on the period of the grating, following the relationship:

$$\lambda_g = 2n_{eff}\Lambda \qquad (2.6)$$

Where λ_g is the central reflected wavelength of the grating, known as the Bragg wavelength, n_{eff} is the effective refractive index over the course of the grating and Λ is the period of the grating. Given the general refractive index of the fibre used in this report, the Bragg wavelength is generally just under triple the grating period when following equation (2.6). An adjustment of the spacing of perturbed fibre sections within the grating will therefore impact the Bragg wavelength, both when adjusted equally or unequally.

A grating of considerable length can be made, with the limits being based on the maximum possible fabrication length and other physical experimental criteria such as reducing erasure during fabrication. Should these limitations be bypassed, a restriction based on the absorption over a length of fibre comes into effect, preventing a grating of theoretically unlimited length using any

known materials or methods. The effects of a grating of increased length are described in detail in section 2.3, though can be summarised by an increased maximum reflectivity and bandwidth.

Variations of fibre Bragg gratings can be classified by both the structure of the inscribed grating [8, 10-12] as well as the power employed whilst inscribing the grating [8, 13], as described in section 2.1.1.

2.2.1. Types of FBG

Type 1

Often used for low temperature sensors and in telecommunications [13], type 1 gratings are fabricated with the use of a laser that inscribes below the threshold for damaging glass. Due to the photosensitivity type, these gratings are able to be completely removed from a fibre upon exposure to temperatures above 200°C, displaying a thermal reversibility that occurs much more readily than for other grating types. Type 1 Bragg gratings are made use of in low temperature environments, operating most effectively between -40°C and 80°C [14]. This suits most telecommunications and sensing applications well and therefore results in type 1 gratings being the most common gratings for such purposes.

As the transmission signal closely resembles the form of the reflection spectra, it can be inferred that absorption or reflection into the cladding of the fibre is negligible, being a fundamental characteristic of a type 1 grating.

Type 2

Having a thermal resistance of over 800°C, type 2 gratings are used in more extreme conditions than type 1 gratings, such as ultra-high temperature and high-power laser sensing. The lifetime of four hours of a type 2 grating at 1000°C has been recorded before it was thermally removed [15].

Type 2 gratings do not share the transmission and reflection resemblance of type 1 gratings, instead wavelengths under the Bragg wavelength are coupled into the cladding modes [14], with only higher wavelengths being granted transmission through the core. This provides the potential to employ a type 2 grating as a wavelength selective tap, limiting transmission below a chosen wavelength [14]. The reflection spectra is of a more typical form, reaching a maximum reflection at the Bragg wavelength, though irregularities in the reflection may be caused by “hot spots” in the laser beam profile [8].

The inscription of type 2 gratings involves exposure of the fibre to a very high pulse energy, causing physical damage to the writing beam side of the fibre core [8]. As a result, type 2 gratings are referred to as damage gratings. As a single excimer pulse may be used to form the grating, type 2 gratings are considered highly practical for mass-production [14] and that this is most efficiently done prior to the application of the fibre’s coating.

Type 2a

Sometimes referred to as type 3 in literature, type 2a gratings have much the same spectral characteristics as type 1 gratings in that the transmission and reflection spectra are complementary [14]. However, type 2a gratings make use of a different fabrication technique, with a long exposure following the annealing of a type 1 grating that involves compaction of the glass matrix [14].

The behaviour of type 1 and 2a gratings when subjected to external changes matches despite small subtleties of index change at the microscopic level, though type 2a gratings can survive noticeably higher temperatures in the order of 500°C [16]. This advantage over type 1 gratings is of use in high temperature sensing applications, though the weak reflection (which can be countered by re-writing the grating) and extended inscription times makes fabricating these gratings less practical [14].

Chirped gratings

Chirped gratings have a period that varies across the length of the grating's physical structure, often linear in nature, which could be considered similarly to a series or smaller length uniform FBGs. As a result, more control over the bandwidth of the gratings is possible, though the strength is reduced in comparison to a uniform grating written under the same conditions. In the case a non-linear function is applied for varying the grating period, applications including pulse compression [17], sensing [18] and dispersion compensation [19] may be made use of.

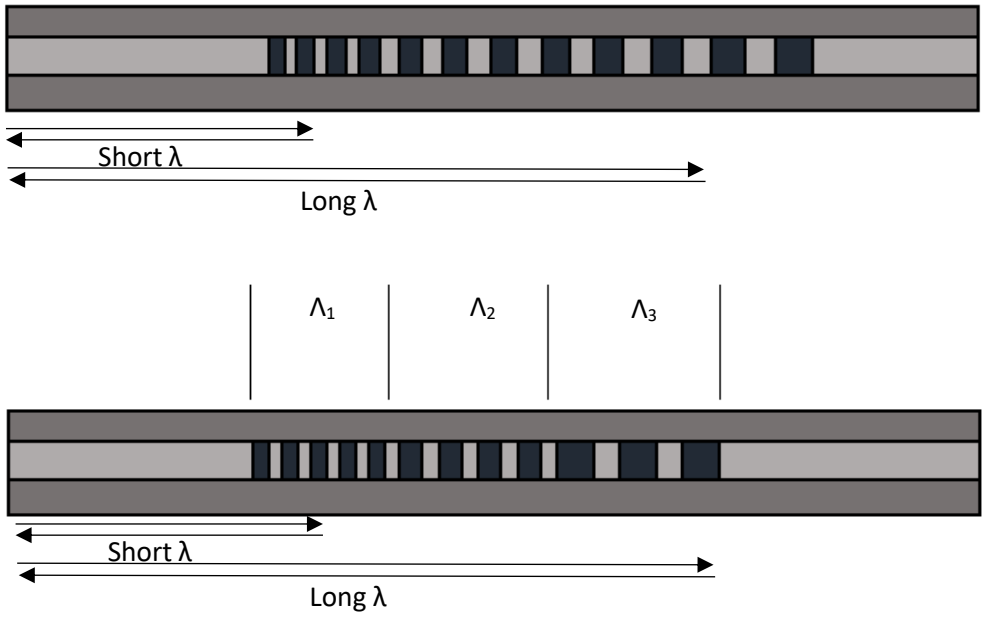

Fig. 2.3: a) a linearly chirped grating of increasing period, reflecting longer wavelengths towards the right of the diagram. b) a schematic diagram of multiple gratings of increasing period to simulate a single chirped grating

Considering the chirped grating to be comprised of a series of short, uniform segments, a chirped grating can be modelled in the form [14]:

$$\lambda_B(z) = 2n_{eff}(z)\Lambda(z) \qquad (2.7)$$

Where z relates the eq (2.6) to the point z along the grating. To extend on this with respect to a chirped grating [8]:

$$\Delta\lambda_{chirp} = 2n_{eff}\left(\Lambda_{long} - \Lambda_{short}\right) \tag{2.8}$$

$$\Delta\lambda_{chirp} = 2n_{eff}\Delta\Lambda_{chirp} \tag{2.9}$$

Where $\Delta\lambda_{chirp}$ is the chirped bandwidth of the grating, Λ_{long} and Λ_{short} are the longest and shortest grating periods, resulting in the chirped grating period $\Delta\Lambda_{chirp}$.

Considering a chirped grating as such a series of individual gratings, the reflectivity of each layer can be modelled as [20]:

$$R_i(\lambda) = \frac{sinh^2\left(L_g\sqrt{q^2-\sigma_i^2}\right)}{cosh^2\left(L_g\sqrt{q^2-\sigma_i^2}\right)\frac{\sigma_i^2}{q^2}} \tag{2.10}$$

Where i denotes the layer in question, L_g is the length of the grating section, q is the coupling coefficient of the section and σ_i contains the wavelength dependence for the layer, expressed as [20]:

$$\sigma_i(\lambda) = \frac{\pi}{\lambda}\delta n_{eff} + 2\pi n_{eff}\left(\frac{1}{\lambda} - \frac{1}{\lambda_{B,i}}\right) \tag{2.11}$$

Where δn_{eff} is the amplitude of the refractive index modulation. In this case, the parameters of this modulation ($n_{eff,}$ δn_{eff},k) are assumed to be constant along the grating length, having no spatial dependency in contrast to the Bragg wavelength of each layer. This alteration in Bragg wavelength for each layer can be monitored via a linear dependence on the grating length:

$$\lambda_{B,i} = \lambda_{B,1} + \mathrm{C}\cdot iL_g \tag{2.12}$$

For i=1, 2,…,M. Where C is the chirp rate coefficient, a constant that defines the rate of change of the Bragg wavelength spatially within the chirped grating as a whole.

A number of techniques for fabricating chirped gratings exist, including changing the relative position of the fibre whilst writing the grating, which may also cause blazing with respect to the fibre axis [8], as well as using a modified phase mask. Most of which focus on altering the Bragg wavelength of the chirped grating instead of the alternative of varying the refractive index of the grating spatially. An alteration of the refractive index over the length of the grating risks the undesired introduction of the Fabry Perot effect [8].

Phase shifted gratings

These gratings make use of a phase shift along the length of the grating to introduce one or more narrow notches to the spectrum at a given wavelength. This allows wavelengths in the spectrum to pass through without reflection, or with an adjustment to the design can reflect narrow bands of

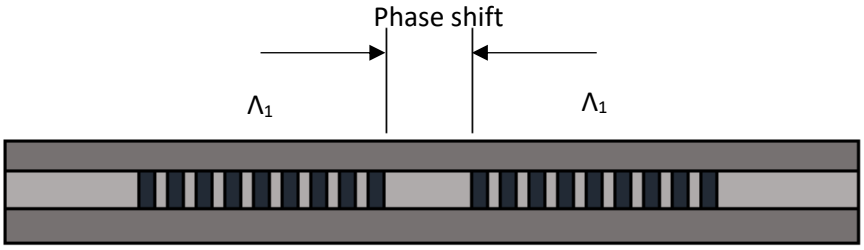

Fig. 2.4: Schematic of a phase shifted grating, displaying an exaggerated split for generating a phase shift. The length of the split is dependent on the desired shift, with the usual length being in the order of a wavelength

wavelengths instead. Phase shifts can be applied to the grating for use in wavelength demultiplexing [21] as well as to produce devices such as comb filters and a single-mode operation of distributed feedback fibre lasers [14].

Considering the phase shift to be located at the point z_ϕ along the length of the grating, there is therefore a split in the original grating, forming a pair of gratings of length L_1 and L_2, with the phase shift location noted to be at $z=L_1=z_\phi$. It therefore follows from coupled mode theory (specifically equation (2.38), covered in detail below) that the matrix for the entire grating structure can be written as [22]:

$$\boldsymbol{T} = \begin{bmatrix} \frac{1}{t_2^*} & -\left(\frac{r_2}{t_2}\right)^* \\ -\frac{r_2}{t_2} & \frac{1}{t_2} \end{bmatrix} \begin{bmatrix} e^{\frac{j\varphi}{2}} & 0 \\ 0 & e^{\frac{-j\varphi}{2}} \end{bmatrix} \begin{bmatrix} \frac{1}{t_1^*} & -\left(\frac{r_1}{t_1}\right)^* \\ -\frac{r_1}{t_1} & \frac{1}{t_1} \end{bmatrix} \tag{2.13}$$

Where t and r are the amplitudes for the transmittance and reflectance for each section of the grating pair. The subscripts 1 and 2 denote the grating sections 1 and 2, whilst $e^{j\phi/2}$ describes the phase shift induced within the grating, of which more detail is presented in section 3.7.1 for use with the modelling used within this thesis. The phase shift, ϕ, is the offset induced in radians, with a phase shift of π therefore providing a shift of half the grating period. Using (2.13) and equations (2.39) and (2.40), the transmittance and reflectance of a phase shifted FBG can be described by:

$$t = \frac{e^{\frac{j\varphi}{2}} t_1 t_2}{1 - e^{j\varphi} r_1 r_2} \tag{2.14}$$

$$r = \frac{r_1 + e^{j\varphi} r_1 \left(\frac{t_1}{t_1^*}\right)}{1 - e^{j\varphi} r_1 r_2} - e^{\frac{-j\varphi}{2}} \tag{2.15}$$

Where $|r_i|^2+|r_i|^2=1$ for i=1,2. This poses a similar expression to the that of a Fabry-Perot resonator comprising of a pair of mirrors, making use of the complex reflectance and transmittances: r_1, r_2, t_1, t_2 [22]:

$$t = \frac{e^{j\left[\frac{\varphi}{2} + \tan^{-1}\left(\frac{\delta_0}{2}\tanh(q_0 L_1) + \frac{\delta_0}{2}\tanh(q_0 L_2)\right)\right]}|t_1||t_2|}{1 + e^{j\left[\varphi + \tan^{-1}\left(\frac{\delta_0}{2}\tanh(q_0 L_1) + \frac{\delta_0}{2}\tanh(q_0 L_2)\right)\right]}|r_1||r_2|} \tag{2.16}$$

Where q_0 is the grating's coupling coefficient (overviewed in section 2.3). When considered in close proximity to Bragg resonance ($\delta_0 \approx 0$), this equation reduces to:

$$|t|^2 = \left| \frac{\frac{1}{\cosh(\kappa_0 L_2)} \frac{1}{\cosh(\kappa_0 L_1)}}{1 + e^{j\left(\frac{4\pi n_{eff}}{\lambda_0^2}\Delta\lambda\right)} \tanh(\kappa_0 L_1) \tanh(\kappa_0 L_2)} \right|^2 \quad (2.17)$$

$$d = \frac{\tanh(q_0 L_1)}{q_0 L_1} \frac{L_1}{2} + \frac{\tanh(q_0 L_2)}{q_0 L_2} \frac{L_2}{2} \quad (2.18)$$

Where d is the distance between the two grating sections, similarly to the equation for a Fabry-Perot resonator's average cavity length.

Techniques for fabricating phase shifted gratings include the use of phase masks which have been modified to incorporate a phase shift into the mask's design [8], localised heat treatment of the grating after fabrication [23] and exposure of the grating region to UV laser pulses after inscription [24]. Processing via phase shifting effectively generates a pair of gratings out of phase with each other which act as a Fabry-Perot resonator. This, as seen in chapter 3.2, allows light at wavelengths matching the resonance points that would normally be reflected to pass through the grating. As the resonance wavelength is dependent on magnitude of the phase shift, the grating can be designed to allow a selected wavelength range to pass, which is simulated in chapter 3.3.

Moiré gratings

Two gratings superimposed with a similar amplitude, but a difference in central wavelength and position on the fibre results in a phase shift in the spectrum passing through [25], being referred to as a Moiré grating. Superimposing the two gratings produces two distinct periods, a slow varying envelope Λ_B, with a low beat frequency and known as a Moiré period, and a rapidly varying envelope, Λ_s. These are described by the equations [14, 25, 26]:

$$\Lambda_s(z) = \frac{2\Lambda_1\Lambda_2}{\Lambda_1 + \Lambda_2} \quad (2.19)$$

$$\Lambda_B(z) = \frac{2\Lambda_1\Lambda_2}{\Lambda_1 - \Lambda_2} \quad (2.20)$$

Where Λ_1 and Λ_2 are the periods of the first and second gratings comprising the Moiré grating. The shift in the central wavelength of the grating is given as:

$$\delta\lambda = \frac{\Delta\lambda\, \delta d}{L} \quad (2.21)$$

Where $\Delta\lambda$ is the difference in Bragg wavelength of the two gratings, δd is the relative shift in the positions of the two gratings and L is the length of the system. In the case of a Moiré grating, the coupling coefficient is of a more complex form, being described by [26]:

$$q(z) = q_0 \cos\left(\frac{2\pi n_{eff} \delta\lambda}{\left(\lambda_0 + \frac{\Delta\lambda\, z}{L}\right)^2} - \frac{\varphi}{2} \right) \quad (2.22)$$

Where:

$$q_0 = \frac{\pi \Delta n_0 C_{01}^{00}}{\lambda_0},\ \lambda_0 = \frac{\lambda_1 + \lambda_2}{2},\ \delta\lambda = |\lambda_1 - \lambda_2| \quad (2.23)$$

In this case, C_{01}^{00} refers to the Bragg coupling in the core for a single mode fibre, z is the location along the z axis and φ is the induced phase shift in the grating. λ_1 and λ_2 are the wavelengths of the two gratings.

The inscription of a Moiré grating can be performed in several ways, such as changing the angle of writing beams [27] or by inscribing the two gratings separately and changing the writing wavelength between inscriptions [28, 29]. In addition, a Moiré grating may be formed from two chirped gratings [27], allowing for a broader stopband in the spectrum's form.

Long period gratings

Gratings with periods in the micrometre range are referred to as both long period gratings (LPGs) as well as transmission gratings. The former name is self-explanatory whilst the latter refers to the coupling of light into forwards travelling modes without coupling into backwards travelling modes. As a result, LPGs provide virtually no reflections instead forming solely a transmission spectrum that may be observed.

Unlike simpler gratings, such as the type 1 and 2 gratings, LPGs encourage an interaction between the main core mode and the odd cladding modes, as the even cladding modes lack the energy to interact. Since coupling from the guided mode to an unguided mode is wavelength dependent, a spectrally dependant loss is induced in the transmission spectrum [14]. In this case, the wavelength dependant phase-matching condition is given by [14]:

$$\beta_{01} - \beta = \Delta\beta = \frac{2\pi}{\Lambda} \qquad (2.24)$$

Where Λ is the periodicity of the grating, β_{01} and β are the propagation constant of the fundamental guided mode and the mode that the coupling occurs with. In the scenario where Δβ is large, the grating period can be in the area of 1μm, though unblazed LPGs result in smaller Δβ values and hence a longer periodicity of hundreds of microns.

Differential changes in the modes can be induced in an LPG by making use of its susceptibility to external bends, strain and temperature changes. This makes LPGs ideal for sensing such changes in surrounding conditions, though the effects of strain are also dependant on the type of fibre the LPG is contained within [30]. Changes in wavelength can also be induced by bending the LPG, as this destroys the constant reinforcement in the coupling between the core and cladding modes due to the cladding modes exiting the cladding-air boundary as well as altering the effective cladding refractive index.

A duel resonance feature has been observed with higher coupling modes in an LPG, which allows for highly sensitive devices. This sensitivity is described by [31]:

$$\gamma = \frac{\frac{\delta\lambda_{res}}{\delta\Lambda}}{n_{co}^{eff} - n_{cl,m}^{eff}} \qquad (2.25)$$

Where $\delta\lambda_{res}$ is the wavelength change, δΛ is the period change and n_{co}^{eff} and $n_{cl,m}^{eff}$ are the core and cladding effective refractive indexes. The most sensitive changes are observed for values of $|\gamma|>5$.

2.2.2. FBG applications

The sensitivity of fibre Bragg gratings to external changes, robustness in environments where other technology struggles and relatively small size makes FBGs prime candidates for a variety of tasks. Some of the main applications for FBGs include use as sensors and performing tasks in telecommunications such as dispersion compensation as well as filtering wavelengths.

Sensors

Some of the most common FBG uses are as sensors for detecting changes in temperature or strain [32, 33], where the fibre's structure is altered marginally by external factors. This adjustment of the fibre's structure alters the grating's period, and therefore the Bragg wavelength, which in turn may be detected. Given knowledge of how a fibre or its coating's dimensions are affected by the aspect being measured, the shift in Bragg wavelength compared to an expected transmission can be used to calculate the change in grating period and therefore, the change in physical dimensions and the change in the monitored condition. In addition, changes in temperature and strain may affect the refractive index of the fibre in a finite and repeatable way.

Taking for example the case of temperature and strain sensing using a chirped FBG, a grating model can be made using a cascade of FBGs, with each section of the model being affected by the variations in temperature (ΔT_i) and strain ($\Delta\varepsilon_i$), as described by [20]:

$$\lambda_{B,i} = \lambda_{B,i,ref} + s_T \Delta T_i + s_\varepsilon \Delta\varepsilon_i \qquad (2.26)$$

Where $\lambda_{B,I,ref}$ is i^{th} reference wavelength, $\Delta\varepsilon$ is the variation in strain, ΔT is the variation in temperature and s_T and s_ε are the thermal and strain sensitivity coefficients. An example of the temperature sensitivity coefficient is 10pm/°C [34] and for the strain sensitivity coefficient is 1pm/με [20].

FBGs hold a key advantage over other forms of sensing, such as electronic sensors, as the method of detection is not affected by a number of factors, including magnetic fields. This, and their relatively small size makes FBGs useful as sensors within a greater variety of environments [35], including those that would prove inhospitable to other forms of sensors, such as within nuclear magnetic resonance devices [36] and within fuel tanks in aircraft [37].

Telecommunications

Fibre Bragg gratings find many uses in telecommunications due to the variety of ways a signal can be manipulated to improve the quality of the data transfer. Fibre optics has recently been demonstrated to provide transmission capacities as high as 54 Tb/s in single mode fibre containing a single core [38]. A common use of FBGs within telecommunications is for dispersion compensation. As mentioned above, a signal comprising of multiple modes may have a variety of paths the modes travel down the fibre via. Some of these are more direct and will therefore travel further down the fibre over a given period than other modes. Via this method, a number of modes will begin to disperse over a length of fibre, requiring compensating in order to retrieve the original pulse and the information carried by it.

The compensation of pulse broadening arising from a spectra propagating through a fibre was first demonstrated in 1992 via a grating-telescope apparatus [39]. Focussing on second and third order group velocity dispersion, the orders were replicated as equal and opposite by means of fibre gratings. By tailoring the diffraction angle to level the ratio of second and third order dispersion of

the grating and fibre, as well as the compensator length to equalise the term's magnitudes, the cumulative dispersion of the orders were made to negate.

Progress in pulse broadening compensation was continued in 1994 through the use of linearly chirped gratings [40, 41]. Here, chirped gratings generate a large and constant dispersion over the bandwidths, which enables the rapid dispersion changes needed for compensation with reflective FBGs. Assuming the chirped grating is placed so the shorter spacing period is facing the light's source, the shorter wavelengths are reflected 'earlier' in the grating structure than longer wavelengths. This caused longer wavelengths to travel for a longer distance and gain an additional time delay in comparison to shorter wavelengths [14].

A transmission-based version of dispersion compensation is also possible by making use of a grating's stop band's proximity to the transmitted wavelengths. Wavelength's close to the grating's stop band experience a strong second and higher order dispersion, affecting the light's propagation to a different degree to other wavelengths in the spectra. This may be used to target particular wavelengths for dispersion control.

A decent amount of research has occurred with pulse compression through the use of FBGs to date [42, 43]. The usefulness of compressing pulse lengths comprises the improvement of range resolution as well as enabling digitisers to capture wavelengths beyond the bandwidth they would otherwise be able to achieve [43, 44]. Compressing the time-bandwidth product of signals enables digitisers to sample an analogue signal with a varying resolution and also has the desirable effect of reducing the file sizes or the data [43] . Performed correctly, pulse compression should perform this task with no loss of data [44, 45].

One advantage held by the methods used in [44, 45] is the reduction of the frequency limit that can be captured, from half the sampling rate, as well as the reduction in digital record length due to oversampling. The Time-Bandwidth Product, a determinant of the number of samples required to represent the original data, and from this, the file size to store the data, has been compressed as a result of the work performed in pulse compression.

Wavelength filtering

The use of fibre Bragg gratings as wavelength filters has recently been employed in relation to ground based telescopes. In this example, FBGs were designed to reflect areas of the infrared spectrum originating from hydroxyl emissions in the atmosphere [46], effectively filtering them out of the transmitted spectra and allowing for an image of the target without the interference of an atmospheric component [47]. This is particularly useful as a solution to observing deep near-infrared observations of the early universe.

The development of non-periodic FBGs, with the ability to supress up to 400 narrow spectral lines while enabling transmission between the lines, was one of the innovations required to achieve this [48]. Another advancement included a conversion method for multi to single mode fibre via a photonic lantern [49-51]. This conversion is required as the gratings presently require single-mode fibres, while multi-mode fibres are needed for collecting light which has been affected by atmospheric turbulence. In addition to this, the use of multichannel fibre to filter for aperiodic FBG fabrication to be used for spectral line suppression [52] has recently been developed, which in combination with the use of photonic lanterns will enable the same filtering to be applied to each channel of the fibre, with fewer errors being present in the final result.

2.3. Coupled Mode Theory

Used to characterise or calculate the interaction of electromagnetic waves within a waveguide, coupled mode theory was first applied to optical devices in the 1970s [8] The theory makes use of the solution to Maxwell's equation with selected boundary conditions to treat complex waveguide structures as if the transverse component of the electric field was a superposition of forwards and backwards propagating nodes [53]. Coupled mode theory forms a useful tool for gaining quantitative information on the spectral dependence of a fibre grating as well as the diffraction efficiency of the grating [12].

As mentioned above, the electric field can be treated as the superposition of forwards and backwards propagating nodes, as shown by [8]:

$$E(x,y,z) = b_1(z)\Psi(x,y) + b_{-1}(z)\Psi(x,y) \tag{2.27}$$

Where $b_{\pm1}$ contains the z dependencies of the modes, varying with the harmonic propagation factor $\exp(\pm i\beta z)$ with $\beta = \beta(\omega) = n_{eff}\omega/c = n_{eff}k$ being the scalar propagation constant. Ψ is transverse dependence, which satisfies the scalar wave equation for the unperturbed fibre.

Making the assumptions that a fibre is weakly guiding, lossless and couples the perturbation of the core's refractive index with the structure's unperturbed normal mode, the electric and magnetic fields can be treated as approximately transverse to the fibre's axis. This enables polarisation due to the fibre's structure to be ignored and the use of the scalar wave equation to be used on its own. Since the modes used in coupled mode theory are finite, the theory serves as an approximation, though accuracy of the interpretation of the properties of a device in combination with the speed of reaching a solution provide benefits that lead to it being a good foundation for research.

The counter propagating nodes occurring in an FBG will each have propagation constants with opposite signs, relating to the direction of propagation for each mode. The condition due to the finite range is referred to as the phase matching condition and is based on the co-propagating or counter-propagating nature of the interacting modes, being held when the two modes travel in opposite directions. Each of these forms a part of the overall description of the system, being described via the frequency detuning (with respect to the design Bragg wavelength), δ, and the coupling coefficient, q(z), in the set of coupled equations [53]:

$$\frac{du(z;\delta)}{dz} = i\delta u + q(z)v \tag{2.28}$$

$$\frac{dv(z;\delta)}{dz} = -i\delta v + q^*(z)u \tag{2.29}$$

Where u and v are solutions to the coupled mode equations for the forwards and backwards propagating modes that must satisfy the equations and two approximate boundary conditions across the grating length, on the z plane. In the example of the boundary conditions $u(0;\delta) = 1$ and $v(L;\delta) = 0$, the reflection coefficient would become $r(\delta) = v(0;\delta)$ with a transmission coefficient of $t(\delta) = u(L;\delta)$ for a grating $0 \leq z \leq L$. The case described below makes use of the example boundary conditions covered here.

The coupling coefficient itself is one of the concepts used to describe the characteristics of a Bragg grating, alongside the design Bragg Wavelength and the effective refractive index. For example, a uniform grating has a constant coupling coefficient over the length of the grating, with the coupled mode equations being able to be solved analytically. Weak gratings, having a small influence on propagating waves, generate zeroth order solutions to the coupled mode equations as the coupling coefficient approaches zero. The index modulation amplitude, which presents the grating strength, may be gained via taking the modulus of the coupling coefficient [53].

2.3.1. Uniform grating solution for coupled mode theory

To expand on the analytical solution to the coupled mode equations for uniform gratings, the differentiation of (2.28) and (2.29), and substitution of the derivatives, forms the following equations [53]:

$$\frac{d^2u}{dz^2} = (|q|^2 - \delta^2)u \tag{2.30}$$

$$\frac{d^2v}{dz^2} = (|q|^2 - \delta^2)v \tag{2.31}$$

By placing (2.30) and (2.31) expressions into (2.28) and (2.29) and applying the two boundary conditions, the following transmission and reflection coefficient expressions may be determined (where $\gamma^2 = |q|^2 - \delta^2$ and L is the length of the grating [53]):

$$t(\delta) = \frac{\gamma}{\gamma\cosh(\gamma L) - i\delta sinh(\gamma L)} \tag{2.32}$$

$$r(\delta) = \frac{-q^*\sinh(\gamma L)}{\gamma\cosh(\gamma L) - i\delta sinh(\gamma L)} \tag{2.33}$$

As can be seen in these forms, the transmission coefficient is non-zero in all locations, provided $|q|^2$ and δ^2 are not equal. The reflection coefficient varies over the length of the grating with poles and zeroes.

2.3.2. The Transfer Matrix Method

In the functions used for generating grating designs in this report, the Transfer Matrix Method is employed to find solutions to the coupled mode equations, enabling a stable and efficient analysis of most gratings. This technique is especially useful for analysing chirped gratings, as these may be divided into a series of effectively uniform periods, with each section of the series having a different period. However, care must be taken to ensure each of these sections are not made arbitrarily small, as equations (2.28) and (2.29) are not valid for a length of a few periods [14]. A sufficient accuracy can usually be achieved if N≥50, following the description of:

$$N \ll \frac{2n_{eff}L}{\lambda_d} = \frac{L}{\Lambda} \tag{2.34}$$

Where λ_d is the design peak reflection wavelength for the grating, and Λ is the design period of the grating.

By dividing a grating into a number of sections (N), so that each section may be treated as a uniform grating, similar boundary conditions allow for the solving of the coupled mode equations as shown

above, with the section length now being Δ=L/N. By doing so, a transfer matrix relation between the fields at the point z along the fibre and z + Δ can be found via:

$$\begin{bmatrix} u(z+\Delta) \\ v(z+\Delta) \end{bmatrix} = \begin{bmatrix} \cosh(\gamma\Delta)+i\frac{\delta}{\gamma}sinh(\gamma\Delta) & \frac{q}{\gamma}sinh(\gamma\Delta) \\ \frac{q^*}{\gamma}sinh(\gamma\Delta) & \cosh(\gamma\Delta)-i\frac{\delta}{\gamma}sinh(\gamma\Delta) \end{bmatrix} \begin{bmatrix} u(z) \\ v(z) \end{bmatrix} \quad (2.35)$$

Where q and δ are, as above, the coupling coefficient and frequency detuning. γ is:

$$\gamma = \sqrt{q^2 - \delta^2} \quad (2.36)$$

With the overall transfer matrix $\mathbf{T} = \mathbf{T}_n \cdot \mathbf{T}_{n-1} \cdot \ldots \cdot \mathbf{T}_1$, with $\mathbf{T}_i$ describing the propagation through each section, the fields at the two ends of the grating may be connected via:

$$\begin{bmatrix} u(L) \\ v(L) \end{bmatrix} = \mathbf{T} \begin{bmatrix} u(0) \\ v(0) \end{bmatrix} \quad (2.37)$$

for a grating $0 \leq z \leq L$. **T** is the transfer matrix appearing in (2.35), indicating it as a 2x2 matrix with elements T_{11}, T_{12}, T_{21} and T_{22} in the form:

$$\mathbf{T} = \begin{bmatrix} T_{11} & T_{12} \\ T_{21} & T_{22} \end{bmatrix} \quad (2.38)$$

Once the four elements of **T** are found, the transmission and reflection coefficients may be calculated using them. Using (2.35) and comparing to (2.32) and (2.33), we see that:

$$t(\delta) = \frac{1}{T_{22}} \quad (2.39)$$

$$r(\delta) = -\frac{T_{21}}{T_{22}} \quad (2.40)$$

Via this method [53] the transmission and reflection of a grating design can be simulated with some efficiency, opening the opportunity for altering aspects of the design and simulating again to better suit the intended purpose. It is also possible to perform the technique described above in reverse to calculate the coupling coefficient from the transmission and reflection coefficients.

2.3.3. Direct Numerical Integration

Another technique for finding solutions to the coupled mode equations makes use of the Runge-Kutta method for integration. Though simple, this technique requires a large number of steps due to the algorithm for integrating, slowing the overall calculation of a solution in comparison to the Transfer Matrix Method [53]. Therefore, the transfer matrix method is used in preference to direct numerical integration for simulations in this thesis.

2.4. Fabrication techniques

2.4.1. Fabrication basics

As the applications of fibre Bragg gratings grow in number, so too has the variety of FBGs, leading to a number of different fabrication techniques. While all these techniques share the same premise, the different approaches to achieving a wavelength selective fibre section, has left potential ways of improving the fabrication process. Each method is limited in a different way, dependant on the specifics of the technique, but all are affected by errors, an aspect which has seen much research to reduce [54, 55]. This research into countering errors has been focussed on systematic errors, due to the repeatable nature and the relative simplicity of solving them compared to random errors in fabrication. The reduction, and eventual effective removal, of both systematic and random errors from the fabrication process would open the doors to fabrication techniques that allow for improved flexibility in the resulting gratings and in an increased precision in the writing of gratings.

At the time of writing, there are four major techniques for the inscription of FBGs [10, 56]:

- Point by point technique
- Mask image projection
- Interferometer/Holographic
- Phase mask technique

Each technique is adapted for its own advantages when writing gratings and is best suited to particular types of grating or fabrication requirement. As a result of variations in the writing method, each is also limited in varying ways, such as accuracy, writing time and tolerance to alignment. A brief description of each follows.

Point by Point

The point by point method functions by writing sections of the FBG individually, requiring a lens to assist with concentrating a single UV pulse onto the fibre. The nature of this fabrication method adds much time to the writing process [8, 10], slowing down the rate of production of gratings, in particular for multiple gratings. At the time of writing, little work seems to have been done to improve this technique's weakness. However, the flexibility afforded and the control in the distance between each section of the grating allows for the writing of diverse and precise grating designs.

Mask Image Projection

Another technique which grants flexibility with respect to the grating design is the mask image projection method, in which a laser is passed through a mask to produce a high-resolution projection onto the fibre. The simplicity of this method, with respect to the other techniques, in particular favours flexibility regarding complex grating structures [8]. However, the masks used each refer to a specific grating design, requiring a new mask to be produced prior to each new grating to be fabricated or if the mask is damaged due to continued use or external causes.

Interferometer/Holographic

The interferometer technique writes via a pair of intersecting beams, crossing to form a fringe interference pattern into which the fibre is presented for inscription [57]. This splitting of the main beam into pairs of, later recombining, beams is performed with the use of a phase mask. This splitting of the beam forms several orders, dependent on aspects such as the angle of the phase mask plate in comparison to the incoming beam, of which the first order is of best use for inscription. The zeroth order, passing through the phase mask and continuing onwards, requires

consideration to prevent it affecting the grating at sections where it will be written. The use of a zeroth order nulled phase mask is possible for this. If lacking this form of phase mask, the treatment of the zeroth order may be performed with a screen to block the zeroth order. Repositioning or titling the mirrors to ensure the location of the interference pattern is to one side, away from the zeroth order's path may also be used to ensure the interference pattern's composing beams can be controlled more thoroughly. Care must be taken with either method to ensure the full strength of the first orders and that any translation of the mirrors is performed precisely.

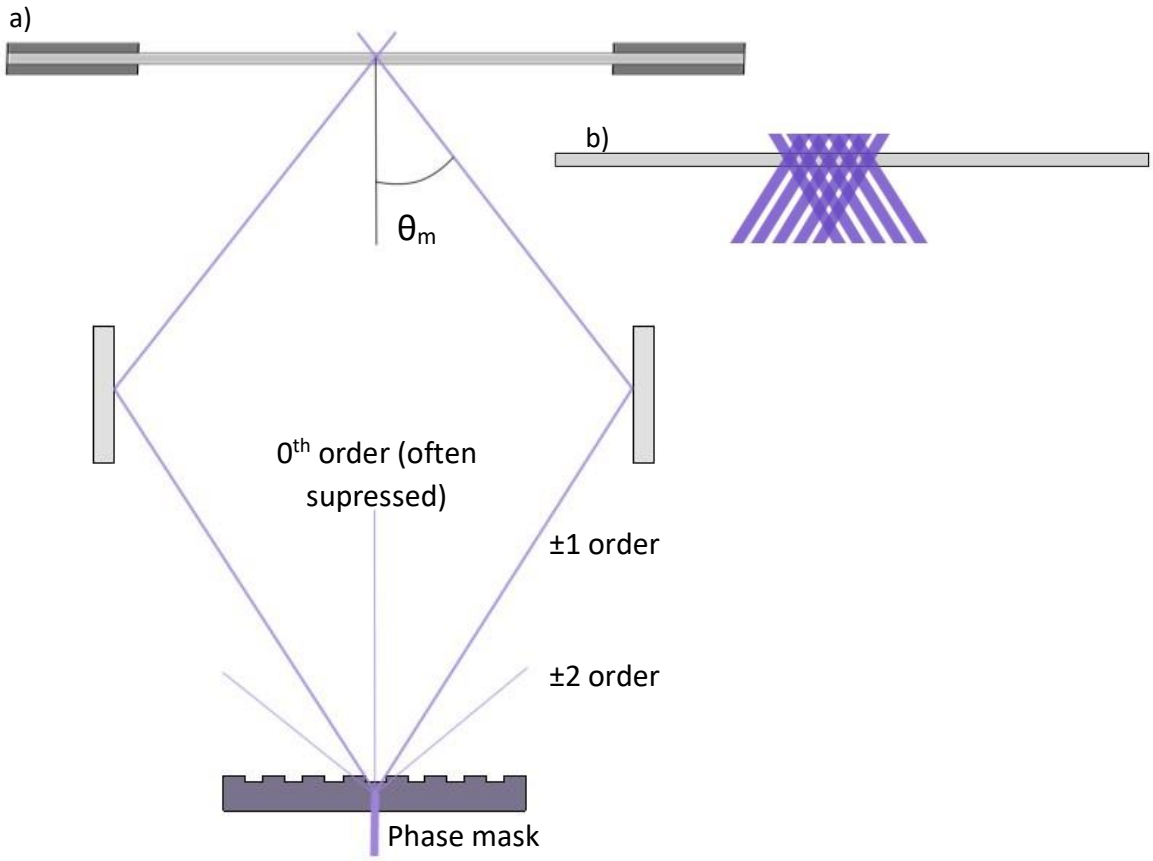

Fig. 2.5 the writing of an FBG via the interferometer technique, demonstrating the 0th, 1st and 2nd diffraction orders of the phase mask. b) A simplified representation of the interference pattern generated by the intersecting beams over the fibre.

The produced grating is dependent on the angles of the reflectors used to direct the beams rather than via a physical mask or individual writing of sections, with both a flexible range of wavelengths and periods able to be produced and a choice of uniform gratings being available. As the rotation of the mirrors changes the intersection angle, the location of the interference pattern changes slightly, requiring the translation of the stage which holds the fibre. The path lengths of the beams from the phase mask to the fibre should be kept identical to ensure mutual coherence of the beams is maximised. The relationship between these angles and the fabricated grating is shown via:

$$\lambda_g = \frac{n_{eff}\lambda_{UV}}{n_{UV}\sin\left(\frac{\theta_m}{2}\right)} \qquad (2.41)$$

Where λ_g is the designed wavelength for the grating, n_{eff} and n_{UV} are the effective refractive indexes of the fibre over the course of the grating and of the fibre relating to the UV writing beam respectively, λ_{UV} is the writing beam's wavelength and θ_m is the angle of one of the incident beams.

In equation (2.41), the value $\theta_m/2$ can be formed via an adjustment of the angle of the pair of mirrors relative to the angle at which they are parallel ($\theta_{\pm1}$) and the diffraction angle of the first order from the phase mask (θ_{mirror}):

$$\frac{\theta_m}{2} = \theta_{\pm1} + 2\theta_{mirror} \tag{2.42}$$

Detuning of the Bragg wavelength relative to errors in the intersection angle can be observed via the equation [58]:

$$\frac{\Delta\lambda}{\lambda_B} = -\frac{\Delta\theta}{2}\cot\left(\frac{\theta}{2}\right) \tag{2.43}$$

However, the orientation of the fringe patterns may not be adjusted using techniques common to the other methods, resulting in this technique's limitation to the fabrication of uniform gratings. In addition to this, since a large amount of importance is placed on the angle of the beams at the intersecting point, any variation in the angle could result in a grating which is marginally different to the designed specification. This difficulty in replicating a previously made grating exactly limits this method in terms of uses where a set of identical gratings are required over an extended period of time.

Phase Mask

The phase mask technique makes use of a thin silica plate with etched relief gratings to direct the incident UV beam into multiple orders, as shown in figure 2.2. The zero order is ideally supressed, via the use of a zeroth order nulled phase mask in some cases, as the interference pattern generated at the fibre core is the sum of all the diffracted orders and not just the ±1 orders. The period of this interference pattern is provided by [8]:

$$\Lambda_I = \frac{\lambda_{uv}}{2\sin(\theta_m/2)} = \frac{\Lambda_{pm}}{2} \tag{2.44}$$

Where λ_{uv} is the wavelength of the writing beam, $\theta_m/2$ is the diffraction angle of the m^{th} order and Λ_{pm} is the period of the phase mask.

The period of the written grating is dependent on the writing beam's intensity. The phase mask, in addition to the diffracted orders of the writing beam, determines the written grating's wavelength as given by [8]

$$\lambda_g = \frac{m\, n_{eff}\lambda_{uv}}{\sin(\theta_m)} \tag{2.45}$$

Where λ_g is the wavelength for the grating, n_{eff} is the effective refraction index of the fibre over the course of the grating, λ_{uv} is the wavelength of the writing beam, θ_m is the beam's angle and m is the order of the beam.

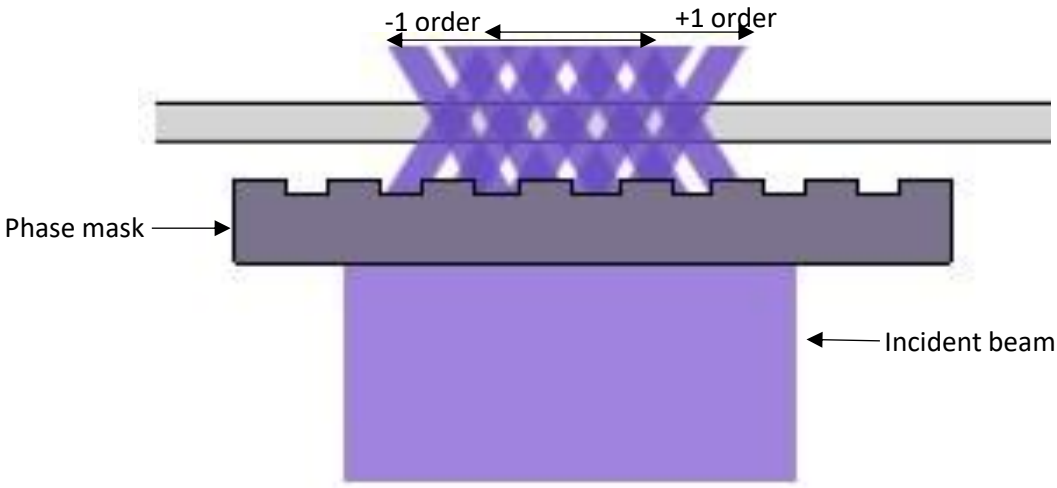

Fig. 2.6: The writing of an FBG via the phase mask method, demonstrating the ±1 orders

In order to locate the grating in the point of maximum beam overlap, the fibre core requires placing as close to the phase mask plate's surface as possible, a distance which is relative to the radius of the fibre itself. Since the distance is non-zero, there will be a short region on either side of the grating without an overlap of the beams. The necessity for the fibre to be held closely to the phase mask poses the risk of scratching the phase mask's surface if appropriate care is not taken to prevent this occurrence during inscription.

The tunability of the inscribed grating varies with the fibre to phase mask difference and the length of the phase mask via the relationship [10]:

$$\lambda_B = 2n_{eff}\Lambda\sqrt{1+\left(\frac{r}{l}\right)^2} \qquad (2.46)$$

Where Λ is the period of the fibre grating, r is the fibre to phase mask separation and l is the length of the phase mask.

Due to the fixed and limited wavelength range an individual phase mask can produce gratings with, a new mask would be required for writing within a new wavelength range beyond that of the original phase mask. Considering the cost of phase masks and their sensitivity to surface scratches, this method can become increasingly expensive in terms of this element. However, the phase mask is the only required component for adapting the beam for inscription [10], thereby simplifying the process of fabrication and providing a distinct advantage over the interferometer method.

The phase mask technique is capable of fabricating gratings with a fixed period and chirp, but by using narrow or scanned beams in UV wavelengths, it is capable of a variety of index modulation amplitudes. This combined with the capability of making the same grating multiple times provides the strengths of this method.

When used, phase masks allow for a precise and repeatable inscribed grating wavelength, enabling the production of the same grating a number of times. A single phase mask plate may contain a small number of individual phase masks, each inscribed with a pre-determined function. As mentioned above, each phase mask does, however, have a limited range for use, meaning that some systems will require a collection of phase mask options for grating inscription.

In setups that make use of a phase mask, the application of a focussing lens prior to the beam's arrival to the phase mask results in the beam focussing in one plane, increasing the power density at

the overlap without affecting the grating length. The lens also determines whether the beam overlaps are aligned along the length of the core of the fibre and assists with generating this alignment.

Gratings of a longer length than the phase mask may be inscribed, though consideration to the motion of the fibre relative to the phase mask. Methods of creating this relative motion without erasure of the grating structure involves the concept of phase mask dithering, where small, repetitive motions of the phase mask along the axis of the fibre's motion follow the motion of the fibre, then return to the original placement swiftly. Suitably aligned with the grating period, this enables a theoretically infinite grating length to be fabricated, assuming freedom from experimental constraints.

Phase mask dithering may be replicated via the use of amplitude modulation, where the reduction of beam amplitude enables the fibre to move a given distance before exposure continues. Whilst the period of time the fibre is exposed to is reduced, this method does not require the phase mask to be in motion, thereby giving an optical rather than mechanical method to fabricate a long grating with a short length phase mask. More detail is provided below on how this is achieved within the fabrication system, though a description of such dithering can be made via [22]:

$$a_0(z,t) = a_0(z) \cdot triangle(f \cdot t) \tag{2.47}$$

Where $a_0(z)$ is the amplitude of the dithering at a given point on the z axis and $0 \leq triangle(f \cdot t) \leq 1$ is a normalised periodic function for a triangle wave with frequency f. Given this, the coupling coefficient can be provided as:

$$q(z,t) = q_0 \frac{\sin\left(\frac{\pi a_0(z,t)}{\Lambda}\right)}{\frac{\pi a_0(z,t)}{\Lambda}} = q_0 sinc\left(\frac{a_0(z,t)}{\Lambda}\right) \tag{2.48}$$

Where q_0 is the initial value for the coupling coefficient and Λ is the grating period.

A number of additional aspects have been developed that can be applied to the main fabrication techniques described above. These range from the suppression of side-lobes to characterising the interaction of electromagnetic waves being carried by a fibre. The aspects also add to the capabilities of the main techniques and enable a better understanding of what occurs which can be applied in the design and fabrication stages.

2.4.2. Fibre sensitivity

An aspect key to the process of inscription, the sensitivity of the fibre to UV exposure has multiple ways of adapting. Four major methods to do this occur, with the most common being hydrogen loading. This is done via the exposure of the fibre to high levels of hydrogen, after which the sensitivity of the fibre to UV is increased, slowly decreasing as hydrogen escapes the fibre. This rate of escape is relative to temperature, with low temperatures slowing this process and high temperatures speeding the rate of escape. After inscription, the need of hydrogen in the fibre has passed, and the remaining hydrogen is expelled through placing the fibre in an oven for a period of time.

Brushing a localised area of fibre using a hydrogen fuelled flame is another method of introducing hydrogen to the fibre, where the hydrogen reacts with the Germano-silica fibre generating Germanium oxide deficient centres permanently, unlike hydrogenation. However, this comes at the cost of weakening the fibre physically after exposure to the flames [10].

Various fibres have different wavelengths of UV that are the most efficient. Matching the wavelengths, such as the use of ArF excimer Vacuum UV radiation at 193nm [59], has been proven to increase efficiency, especially for the point by point method.

In addition to this, doping the fibre with certain elements can increase the sensitivity, with Boron having a significant effect [10]. It has been found that Boron's introduction to the fibre reduces the refractive index when it is introduced [8], though this can be counteracted via thermal annealing afterwards [10]. Other co-dopants that may be used are Nitrogen and Tin [8]. Tin-Germanium co-doped fibres have some advantages over Boron in terms of temperature resistance and an increased photosensitivity, though Tin-Germanium fibres are rarer.

One thing that should be noted when fabricating gratings using fibres with increased sensitivity is that the sensitivity of the grating may change over the course of writing a grating, particularly if the grating forms over many hours. Hydrogenation is a good practice to write gratings with as this variation is lessened, reducing the chances of accidentally producing gratings at different wavelengths when using the FBG [8].

2.4.3. Apodisation

Apodisation is a process used to supress the side-lobes that occur during the fabrication of FBGs. Side-lobes occur in the grating spectra due to the grating's physical nature of being finite. This implication that they have defined and abrupt ends forms a rectangular function, in turn forming a sinusoidal Fourier transform with side-lobes that may not always settle at a zero point [8]. In some areas, such as telecommunications, side-lobes can cause adverse effects that counter the purpose of the grating, hence the need for a process to supress them.

To achieve this, apodisation adapts the magnitude of the grating's coupling coefficient with respect to the location on the fibre through the use of a function, often a modified raised cosine [60] though other functions such as Gaussian and Sinc may also be employed and combined [8]. The gradual increase in coupling coefficient upon entering and decrease upon exiting the grating via such functions results in the desired suppression of the side lobes present in an unapodised grating. Care must be taken to not alter refractive index modulation amplitude, as this changes the local Bragg wavelength, forming a distributed Fabry Perot interferometer, which results in a structure forming on the blue side of the grating spectrum [8]. Maintaining a constant average refractive index throughout the grating's length is important to prevent such formations.

In addition to this side lobe suppression, aspects of the grating are also improved via apodisation, such as dispersion within the fibre [8].

Two different methods for applying apodisation are optically and mechanically. Optical methods use either the Moiré method or its alternatives to vary the intensity of overlapping beams while maintaining a stable refractive index. Mechanical methods involve moving parts, either the fibre [61] or dithering of the phase mask [56].

Within the AIPT fabrication system, apodisation is achieved via a slight adaption of the moving fibre technique, where the fibre moves gradually relative to the phase mask, as covered in section 3.1.1. The fibre is dithered in the translation axis to wash out the inscribed grating to the required degree. Given a linear variation in dither amplitude and a stationary phase mask, an apodisation effect is added to the inscribed grating [8]. The beam size is of importance with this method, as the smearing of the grating is dependent on the width of the inscribing beam thereby requiring a small beam to

ensure precise apodisation. As the AIPT system fires the beam at given points in the fibre's translation, rather than at set times, the addition of apodisation functions via a manipulation of the beam firing pattern for the grating design, feigns the effects of fibre dithering in a system that aims for consistent motion. This irregularity in the firing pattern at each end of the grating is generated within the FBG's design file, which instructs the operation of the system's modulators on the relevant control of the beam.

Other techniques for applying apodisation to a fabricated grating include the periodic and symmetric stretching along the fibre axis during inscription has been performed [62], and is possible for gratings of any length. Additionally, the use of a variable diffraction efficiency phase mask may provide the desired effect via the variable design of the phase mask and the points used during relevant steps in the fabrication. However, this technique requires a phase mask to be created for such a purpose, of which the Gaussian phase-mask profile can only be approximated [8].

2.4.4. Beam modulation

The adoption of modulators to modify the incident UV beam's path, which removes the need for the phase mask to physically shift, known as dithering, is another variation made of FBG fabrication systems. The initial amplitude modulation research succeeded in this task, though the method results in the loss of a degree of the laser's power. This alternative method for simulating a moving fringe with the fabrication setup is developing with attempts to increase the efficiency of the setup via higher modulation frequencies [63] and modulating the phase of the incident beam [56, 64, 65].

The reduction of the need for phase mask dithering not only simplifies the setup, lessening the need for more moving parts, it also reduces the chance of any damage upon the phase mask. As the phase mask can now remain stationary, any alignment based on the phase mask does not need to consider its motion, reducing both the complexity of the process and also leaving a smaller potential for a misaligned section to touch the phase mask. This will potentially extend the lifetime of a phase mask through the smaller risk to it.

Two main methods of modulation are explored in this thesis, amplitude and phase modulation. Within the fabrication system, the use of an amplitude modulator provides the capabilities for fabrication without phase mask dithering. In the case of an acoustic optical modulator, this is achieved via the generation of an acoustic wave front from an oscillating transducer within the device, which produces a varying index of refraction based on the periodic expansion and compression of the sound. A beam entering this region is scattered by the periodic modulation of the index of refraction, via the equation [66]:

$$\Lambda(\sin(\theta_i) + \sin(\theta_o)) = m\lambda \qquad (2.49)$$

Where Λ is the wavelength of the sound wave and λ is the wavelength of the inbound light. θ_i and θ_o are the angles of the inbound and outbound beams of the m^{th} diffraction order.

Given that the conservation of energy and momentum requires $\theta_i = \theta_o$ for sound frequencies of the order 10^8Hz [67], (2.49) can be simplified to [66]:

$$2\Lambda \sin(\theta_o) = m\lambda \qquad (2.50)$$

The amount of a beam transmitted into a diffracted beam order is affected by aspects within the modulator such as the sound wave's intensity. In the fabrication system, the ±1 order is used, with 70% of the inbound intensity aimed to be transmitted to one direction of the first order, though the

actual transmission at present requires some attention with respect to alignment and modulation settings to achieve this target. The efficiency of the diffraction order desired is dependent on the RF power provided to the AOM by a radio frequency (RF) driver.

Additionally, AOMs are capable of periodically allowing and denying a beam to pass via a scattering mechanism. This varies for each beam order, with the zeroth order being largely unaffected by this, and the first order experiencing amplitude modulation. In the case of the fabrication system used in this thesis, this amplitude modulation is of use for enabling scanning of the beam across the fibre, of which more detail is found in section 3.1.2.

Phase modulation operates in a different way, with crystal housed within whose dimensions oscillate with a chosen frequency pattern. Usually achieved via piezoelectric properties of the crystal, this alters the path length of the light beam through the medium with respect to time, changing the phase of the outbound beam. As a piezoelectric medium can be modified by periodic change in electric field, a periodic alteration of the outbound phase can be achieved. For example, a sawtooth pattern for an electric field (demonstrated in Fig. 2.7), will cyclically expand the crystal over time, then swiftly remove the induced expansion back to the initial state. This will cause the outbound beam's phase to shift by a set degree, then return to the base state and repeat.

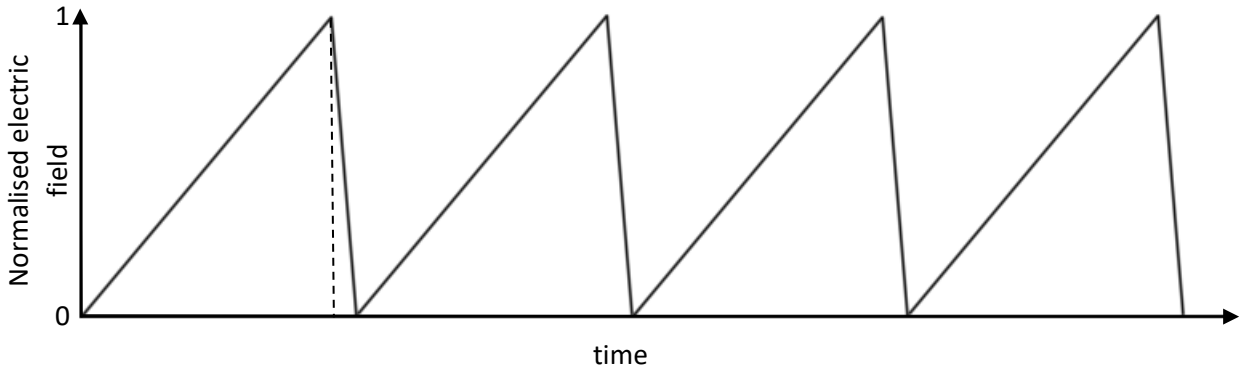

Fig. 2.7: A representation of a sawtooth signal for the use of controlling the phase modulators. On the first period is a demonstration of the finite fall time, required due to the physical nature of the piezoelectric crystal. The period time is dependent on the translation speed of the stage employed in the system.

Following the piezoelectric method for phase modulation, the change in phase of the beam is adjusted by an alteration in the dimensions of the piezoelectric crystal, which in turn depends on the electric field via [68]:

$$S_p = s_{pq}^E T_q + d_{pk} E_k \tag{2.51}$$

$$D_i = d_{iq} T_q + \varepsilon_{ik}^T E_k \tag{2.52}$$

Where S_p is the mechanical strain in the p direction, $T_q$is the mechanical stress in the q direction, D_i is the electric displacement in the I direction, $s_{pq}^E$is the elastic compliance tensor in a constant electric field, d_{pk} is the piezoelectric constant tensor, $E_k$is the electric field in the k direction and ε_{ik}^T is the dielectric constant tensor under a constant stress.

As an example, in the case of a crystal with both the stress and electric field acting along the same axis, equations (2.51) and (2.52) will lead to (2.53) and (2.54) [68]. The subscript "3" in (2.53) and (2.54) refers to the polarisation axis (orthogonal to the stretch axis) of the material, as demonstrated in Fig. 2.8.

$$S_3 = s_{33}^E T_3 + d_{33} E_3 \tag{2.53}$$

$$D_3 = d_{33} T_3 + \varepsilon_3^T E_3 \tag{2.54}$$

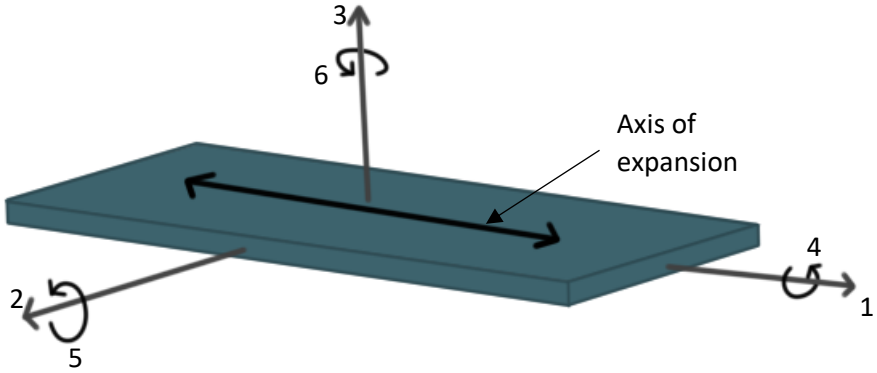

Fig. 2.8: Tensor directions for defining the relations in (2.51)to (2.54), with 1 and 4 being in the axis of expansion, 2 and 5 being transverse to the expansion and 3 and 6 being in the axis of the crystal's thickness

The mechanical stress and strain exerted on the crystal leads to its expansion along the desired axis, changing the path length of the beam through the crystal. Therefore, the beam exits the crystal at a different point in its period, leading to a different phase than would be attained had the beam left the crystal in its original state. This variation in beam phase is linearly dependent on the change in the path length through the piezoelectric crystal, as described by [12]:

$$\frac{\varphi_i}{2} = \frac{2\pi n_{eff}}{\lambda} \Delta z_0 \tag{2.55}$$

Where the effective refractive index of the gap medium is n_{eff}, λ is the wavelength being inspected and Δz_0 is the length of the gap. φ_i is the phase shift resulting from the presence of such an object.

Equations (2.53) and (2.54) demonstrate that an alteration of the electric field will result in a variation in strain the crystal is under, which may be altered with respect to time under a time dependant electric field. The variation of electric field to be used within this thesis is covered in more detail in section 2.4.4.

The fabrication demonstration by Liu [63] of complex gratings, with the setup generating gratings with spectral responses in agreement with calculated responses, showed improvements to the fabrication process, with complex gratings being written for uses such as filters with amplitude and phase desired for pulse shaping. However, this did not go into great focus on the loss of efficiency from the index modulation technique employed.

The investigation of the phase modulation of one of the two beams in an interferometer setup, performed by Sima [64], displayed how such a method could perform. The adjustment of one of the two intersecting beams to generate a constructive or destructive interference fringe pattern while the fibre is passed across the pattern allows for the fabrication of a wide range of grating periods by a single setup. This technique of employing phase modulation appears to work for writing gratings

with a strong change in refractive index and displays improved inscription speed, stability and flexibility in fabrication, though little published work has been done to improve on this setup and counter errors since its introduction.

Gbadebo's investigation into phase modulation with the holographic inscription method [56] differed in the method modulation was employed in the setup, with the aim to replace the Acoustic Optical Modulator (AOM) with a phase modulator. The advantages of the adaptation were identified, with frequencies increasing up to 9kHz, from the 100Hz limit with phase mask dithering, as well as countering the weakness of AOMs with phase masks in effectively blocking out half the beam's power. The adaptation of the fabrication setup demonstrated succeeded in its use instead of the AOM and was shown to work alongside an amplitude modulator. This has been employed in fabrication with the current setup in AIPT and interest has been displayed for more research, though little seems to have been published on this in the time since his thesis.

The use of phase and amplitude modulators within the fabrication system provides the capability to scan the inscription beam across the fibre without the risk of erasing sections of the grating's form or spectrum. More detail on how this is performed is covered in sections 3.13.1.1 and 3.1.2.

2.4.5. Grating length and FBG arrays

Another aspect of FBG fabrication that little published work can be found on is an adaptation of writing and grating design techniques to allow for longer, more advanced gratings to be created on systems that would otherwise be limited. While arrays of FBGs have been investigated, especially for use as sensors [33, 69], the use of an array of short gratings to simulate a single, long grating currently has little published work developing it.

The lack of research into the replication of long FBGs with an array of gratings first poses the challenge of identifying if it is a viable option. The identification of a technique for FBG arrays working as a long grating replica would enable current fabrication systems to produce them, thereby increasing the amount of research that can be performed on complex, long gratings.

2.4.6. Recent fabrication advancements

In order to develop a system to apply the advantages of the techniques described above, several adaptations have been approached, including the use of modulators [63, 64] and feedback [56, 65] during fabrication. In addition to this, work had advanced in the apodisation, or reduction of side-lobes from the spectral changes, of FBGs [70]. Among this work is recent research into techniques which are still in development at the time of writing, such as the use of FBGs as components such as a wavelength selective switch [71]. As such, some of the techniques described here may suffer from a lack of published work, an issue which is likely to be resolved in upcoming years.

Recent work on apodised FBGs by Abdullina and Vlasov [70] has progressed the suppression of side-lobes in both holographic and phase mask setups, leading to higher quality gratings in terms of affecting chosen wavelengths and reducing any undesired effects on surrounding wavelengths. This has resulted in an improved ability to accurately, and repeatedly, target specific wavelengths during fabrication. This precision may be carried over onto more complex designs with some investigation and is an aspect of recent research that may be adapted onto future setups for enhancing FBG quality.

Some development has also been sought in the use of FBGs to emulate the output of more complex or expensive components. Mainly used in communications areas, the use of FBGs for dispersion compensation has been prevalent for a while, with research still ongoing [72], more work is being advanced to do with using FBGs in place of other components, though much of it is in the early stages.

2.5. Chapter conclusion

This review of progress in the fields of fibre grating fabrication outlines the growth in an application driven field. Processes for a variety of fabrication techniques and for inscribing gratings for specific purposes have been developed, with room to improve these techniques to mitigate constraints that result from experimental conditions.

A fabrication system that monitors the fabrication process and compensates for weaknesses of the main inscription methods presently holds little observable research in terms of its application to a whole system, though interest has been shown. Such a feedback system would enable the elimination of a portion of fabrication errors, in particular a potential to limit the effects of random errors from factors such as the fibre itself. The successful implementation of fabrication feedback could also allow for more complex concepts to be investigated with gratings, as the divergence of the fabricated grating with respect to the designed grating could be reduced to acceptable parameters. Further work beyond the implementation of feedback would improve this further, enabling complex gratings to be fabricated closely to their design.

The applications of FBGs are as varied as the structures capable of fabrication, with possibilities mainly being focused in the areas of telecommunications and sensing. The majority of sensing applications involve the observation of changes to the fibre, and by extension the grating, itself, though some progress in recent years has been made in microchannels, as further described in section 3.7.5. Whilst this research at present has been observing the effects of these channels, potential applications into detection of variations in the contained fluid has had limited research.

These two apparent gaps in the literature are explored in this thesis, with the aim of enabling more complex gratings to be written for a variety of purposes, including the detection of nanometre-scaled particles suspended in a medium. Subsequent improvements to the fabrication system will enable a greater flexibility in regard to how fibre gratings are inscribed and to the designs of gratings that may be fabricated, therefore increasing the potential options for grating-based research.

3. Grating designs and applications

3.1. AIPT advanced fabrication system

3.1.1. Inscription system

The system used for fabricating FBGs in this report makes use of the phase mask technique to generate an interference pattern at the point the fibre is placed. The system as a whole can be considered in three parts; the inscription head, where the beam is split and recombined over the fibre for writing, the beam control prior to the inscribing beam reaching the inscription head, and the equipment for monitoring the fibre during fabrication, which is discussed in the next section.

In this system, the inscription head comprises of a cylindrical focussing lens, which serves to focus the inscribing beam in one plane prior to it reaching a phase mask, which may be swapped out between inscriptions as required and some clamps for holding the fibre in place. A moving stage is employed to gradually move the fibre clamps, and thus move the fibre across the beam as inscription occurs. The speed of this motion is controllable via the controlling software among other settings to assist with calibration prior to starting the inscription process. To counter any accumulation of error from the motion of the stage, a location feedback system is employed to fire points of the grating based on the stage's location rather than using the inscription time to estimate the current stage location [56]. This reduces unintended changes to the grating related to non-uniformities in the stage's motion and any build-up of errors linked to it. The motion precision of the stage is approximately 300pm and information of the stage location is fed to the modulator described below in the beam control segment of the system. The speed of the stage's motion during inscription is dependent on the grating itself and may be adjusted to alter the strength of a written grating. Inscription speeds vary from 0.006mm/s, usually for shorter gratings, to 0.032mm/s, for gratings approaching the present limit on grating length, though both ends of this range may be passed if such a need arises. The inscription speed is most commonly between 0.008mm/s and 0.014mm/s. Up to the moving of the system to the new laboratories, the maximum inscription length was limited to 10cm, though this will have the option of being increased with the inclusion of an interferometer head mounted on a 1m translation stage. As part of this change, an adaptation to the fibre clamping system will be required to prevent any sagging of the fibre in the inscribing zone. Details on this are provided in section 3.1.2.

The option for observing strain on the fibre is available and is used for situations where adjustments to fibre strain is needed prior to inscription or for when this constraint is of importance to the grating. The fibre to phase mask plate distance is monitored via a mounted camera. When combined with software for processing and displaying information such as the distance between the fibre and phase mask plate and any shift in this distance along the length, this camera enables pre-inscription control or suppression of any tilt to the fibre relative to the phase mask plate. This system currently measures the distance in pixels, which by comparing the distance at each end of the section, a fibre/phase mask plate angle can be calculated. This angle upon inscription is in the area of 0.01°, with a reported 0° being an achievable and preferable result. This allows additional control over the tunability of the grating's centre wavelength, as described in section 2.4.1. A screen is placed behind the fibre and serves not only to block the inscribing beam exiting the system after the fibre, but also to assist with aligning this beam with the fibre.

The beam itself is generated by a Coherent I300 laser with a wavelength of 244nm and a beam size between 450µm and 1000µm. Prior to reaching the inscription head, the beam passes through a series of controlling components to ensure the beam is suitable for inscription. The beam requires focussing to prevent a beam of too large, degrading the accuracy of wide bandwidth gratings, and too small a diameter, increasing the difficulty in alignment, whilst maintaining a constant size across the diameter of the fibre. This is achieved by slowly focussing with a long focal length lens. In order to ensure the beam size is constant across the diameter of the fibre, the beam's Rayleigh length must be greater than the fibre's diameter, with a minimum length of 125µm being selected. A combination of lenses, shown in Fig. 3.1, focusses the beam in the current setup to a Rayleigh length of between 265µm and 330µm, dependent on the alignment and condition of the laser at the time.

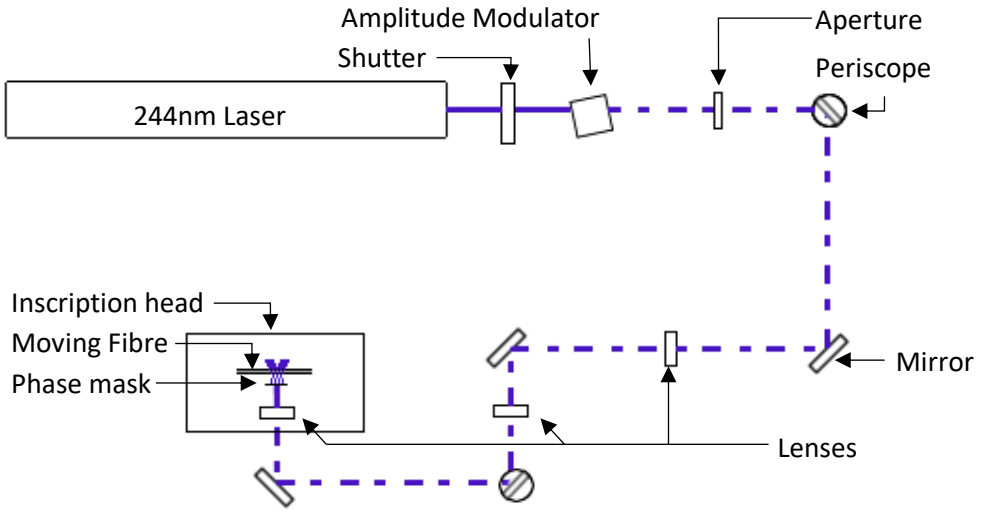

Fig. 3.1: The former laser setup, as used in the old laboratories. Showing beam control components such as mirrors and the inscription head.

During inscription for gratings in this report, the laser power is set to be between 95 and 125mW, with the laser current most commonly being at 39A. This variation in power is most commonly due to aspects such as the alignment of lenses and mirrors both in the system as a whole and within the laser casing. Issues with the system alignment can be fixed through attention to each component in person, though any misalignment within the laser casing usually presents a delay due to maintenance regulations.

The main addition to this section from the norm is an amplitude modulator, which serves to attune the beam based on the apodisation profile. The position of the stage is fed back to a control system in the form of a sin wave with 1024 data points, which is then used to command the modulator appropriately [56]. Whilst modulating different aspects of the beam has been used in several other places, such as in Southampton [64], modulating the amplitude is a route that does not seem to have much published work as of the time of writing.

With respect to the AOM, whose operation is covered in section 2.4.4, the modulator is employed to create a periodic change in amplitude in the first diffraction order, with the aim of 70% transmission into one of the first orders. This effective on/off transmission of the beam in this order allows for the inscription head to move during the "blocked" section of the period and inscribe during the "transmitted" section. Appropriately timed, this enables the fibre to be scanned along the beam path without a constant exposure that would erase the grating, instead creating sections of exposed

and unexposed fibre of the desired design. Control of the AOM is linked to the present location of the translation stage within the inscription head, allowing transmission to occur at set points along the fibre.

The stage position feedback functions similarly to a timed function for controlling the modulator, though rather than the position being calculated by the runtime and set translation speed, it is the position of the stage itself that is used. The position is then used to determine the required signal for the modulator in terms of the first order transmission pattern's frequency. The acoustic wave generated by the AOM for the required frequency of transmission can therefore be adjusted based on the stage's physical translation, rather than the simulated progress assuming uniform stage motion. This reduces the potential for non-uniformities in translation speed to cause an unintended change in grating structure and thus, potential erasure of a grating section.

Via use of the AOM, aspects such as chirp may be introduced via an adjustment of the firing pattern of the beam onto the fibre to achieve a designed coupling coefficient pattern. Taking the modulation as a method to simulate phase mask dithering [22]:

$$q(z,t) = q_0 \frac{\sin(\pi k)}{\pi k} = q_0 sinc(k) \tag{3.1}$$

Where q_0 is the initial value for the coupling coefficient and $k=\frac{a_0(z)}{\Lambda}$, with $a_0(z)$ being the amplitude of the dithering at a given point on the z axis and Λ, as before, being the grating period.

For the example of applying chirp, the coupling coefficient equation becomes:

$$q(z,t) = q_0 \frac{\sin\left(\frac{2\pi z}{L}\right)}{\frac{2\pi z}{L}} = q_0 sinc\left(\frac{2\pi z}{L}\right) \tag{3.2}$$

When applying the local Bragg wavelength:

$$\lambda(z) = \lambda_0 + \frac{{\lambda_0}^2}{2n_{eff}L_g}\frac{z}{L/2} \tag{3.3}$$

In the above equations, as before for chirped gratings, λ_0 is the base Bragg wavelength for the grating, L_g is the length of the grating section and L is the length of the whole grating.

Despite the many advantages of such a system, developments can be made to improve upon it and counter its limitations. A more powerful laser may be employed by this setup to increase the power reaching the fibre during inscription and fabricate the gratings at a faster pace. In addition, the limitation of a fabricated grating's length to 10cm within this setup removes the possibility of some of the longer potential designs to be inscribed without a method for stitching together a series of grating sections to replicate one long grating. Such improvements have been sought with the development of the inscription system in the new laboratories, along with concepts for increasing the system's potential for replicating a grating's design more closely and increasing the flexibility of gratings that can be made in comparison to the old system described.

3.1.1.1. Example fabrications on the old system

To highlight the fabrication capabilities of the old system, a number of gratings for research outside the scope of this thesis were inscribed. The majority of these gratings were for uses within AIPT and for associates of the institute. Many of the gratings provided the opportunity to acquire techniques for fabrication that would not have otherwise been learnt prior to the movement of the inscription setup to the new laboratories.

FBGs as a wavelength selective switch

One aspect of research alongside the optical communications branch of AIPT is the production of gratings for use with parametric comb generation and ensuring flat comb lines. The work on optimising the flat top spectra via the use of a wavelength selective switch (WSS) has been promising thus far for comb regeneration and the increase in the number of comb lines [71]. Via a WSS in combination with a parametric mixer, a WSS has been shown to provide flexible pre-dispersion management which controls the outcome of the parametric process to generate a comb. By optimising the phases of the comb source lines, the number of comb lines generated by a single stage parametric nonlinear mixer has been tripled [71].

In the present form, the process for creating a parametric comb utilises a wave shaper. In order to make the creation of a system for making these combs more viable, there is a need to replace this expensive component with a cheaper alternative. Current research into this is aiming to use FBGs, designed to manipulate the phase to create the flattest comb sections possible, using a grating with a broad wavelength and with more control over the time delay. Thus, a requirement was set for a grating of precise central wavelength that provided a suitable time delay with respect to the inbound wavelengths, with Fig. 3.2 showing the form of the designed time delay in blue. With these prerequisites, a grating was designed and fabricated to enable such control, so that it could be tested alongside the existing process for parametric comb generation.

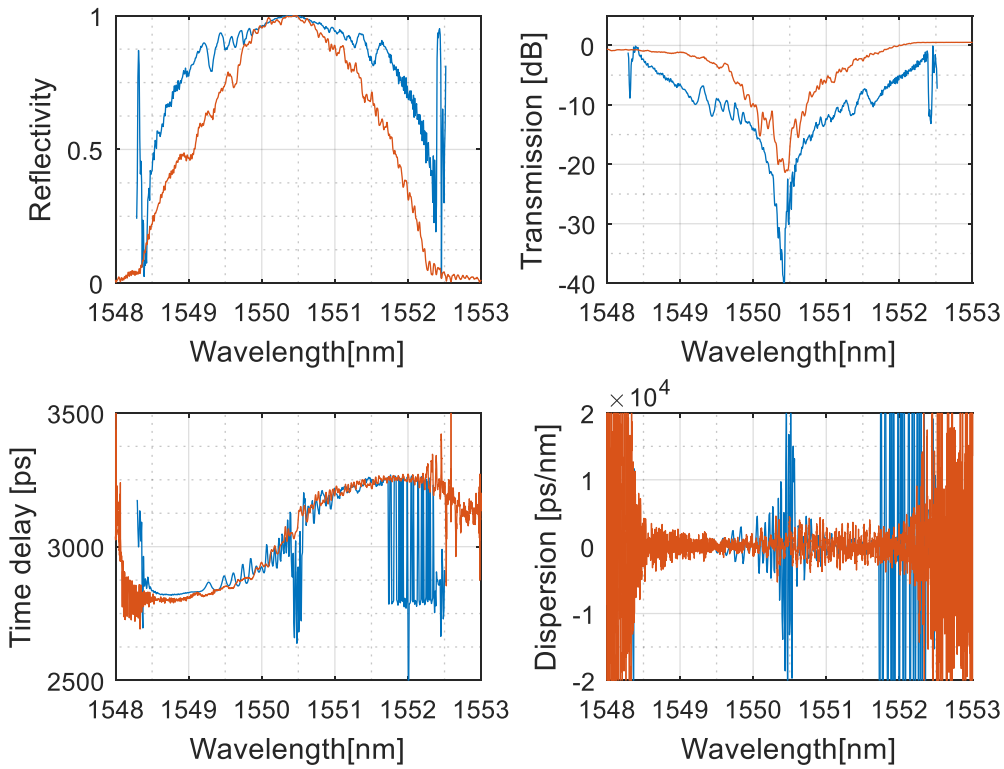

Fig. 3.2: An example of a fibre fabricated for use in place of a wavelength selective switch. One of several gratings made for this purpose. The design is shown in blue for comparison to the fabricated grating in red. A wavelength shift of +0.4nm was observed, with the plot of the design shifted from a centre at 1550nm to 1550.4nm to aid in comparison. The main focus, being the time delay, has been achieved, though improvements could be made to other aspects.

An example of a fabricated grating for use as a WSS is presented in Fig. 3.2. Following tests, more versions are likely to be required to refine the initial results and to act as a reliable method of achieving the requirements of these gratings. As of the time of writing, further fabrications are yet to be made due to delays in setting up the fabrication system in the new laboratories. During the fabrication of the grating in Fig. 3.2, the laser power was experiencing issues, resulting in a weaker than intended grating, though the form of the grating was a close match.

Once a method of using FBGs in place of a WSS is found, the setup for generating parametric combs could easily be replicated and used in optical communications more widely, providing a cheaper version of a wave shaper. As of writing, this research is still under way.

FBGs for measuring heartbeats

Another set of gratings inscribed was for use in measuring small changes in shape due to heartbeats. Gratings were created to test the functionality of such a system with the grating designs and were subsequently sent to Diasens Doo Beograd in Serbia, as part of the CARDIALLY project, for testing. This project is an interdisciplinary proposal, combining the capabilities of Aston University, Universita Degli Studi Di Brescia (Italy), Diasens (Serbia) and Novosibirsk State University (Russia) and funded by Horizon 2020 Research and Innovation Staff Exchange. The overall aim of the project is to provide applications in cardiology to cut costs in European health care systems and improve quality of life.

A part of the project involved the creation of FBGs for the detection of small motions caused by heartbeats on the carotid artery, which was performed at Aston University in collaboration with Diasens in Serbia. This is achieved non-invasively via a multi-channel grating located on the surface of the skin, above the carotid artery. An example of such a grating is provided in Fig. 3.3 and Fig. 3.4 with gratings following a similar design being created in addition. All the grating designs feature a multi-channel form, to aid in the detection of the small movements resulting from surface

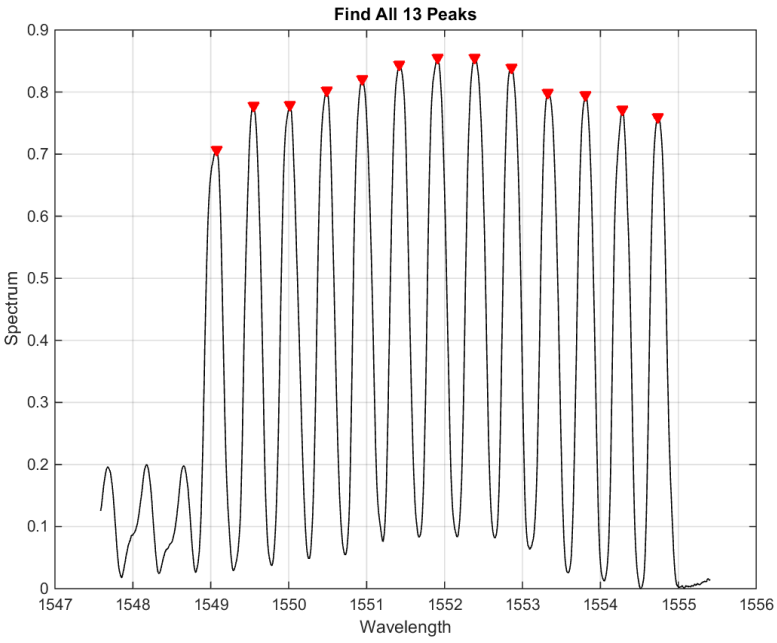

Fig. 3.3: Example of a reflectivity spectra plot of the desired fabricated outcome for the gratings, considering beam size effects, for Cardially. One of these was provided for each file for inscription.

heartbeats. The design of the grating in Fig. 3.3 and Fig. 3.4, features thirteen narrow band channels of even spacing, with the reflectivity diminishing with peaks further from the central wavelength. A variation of this design with each channel being of equal strength was also present to ensure simulations were physically accurate. In the case of fabricating these designs, the primary concern was the presence of the thirteen channels to enable to observation of the effects of the heartbeats on a physical grating of this design. A secondary requirement was also placed on the reflection strength of the gratings, as a weak reflectivity would increase the difficulty of observing small alterations.

During the fabrication of this set of gratings, an issue arose with the output power of the laser, which resulted in slightly weaker than intended gratings, requiring more time to fabricate to the intended strength. For this early stage in the research in Serbia, the change in strength of this degree would not cause a great problem, as the effects of the spectrum's form is of greater importance for early tests, though some attention to the laser source was made to correct this for future work.

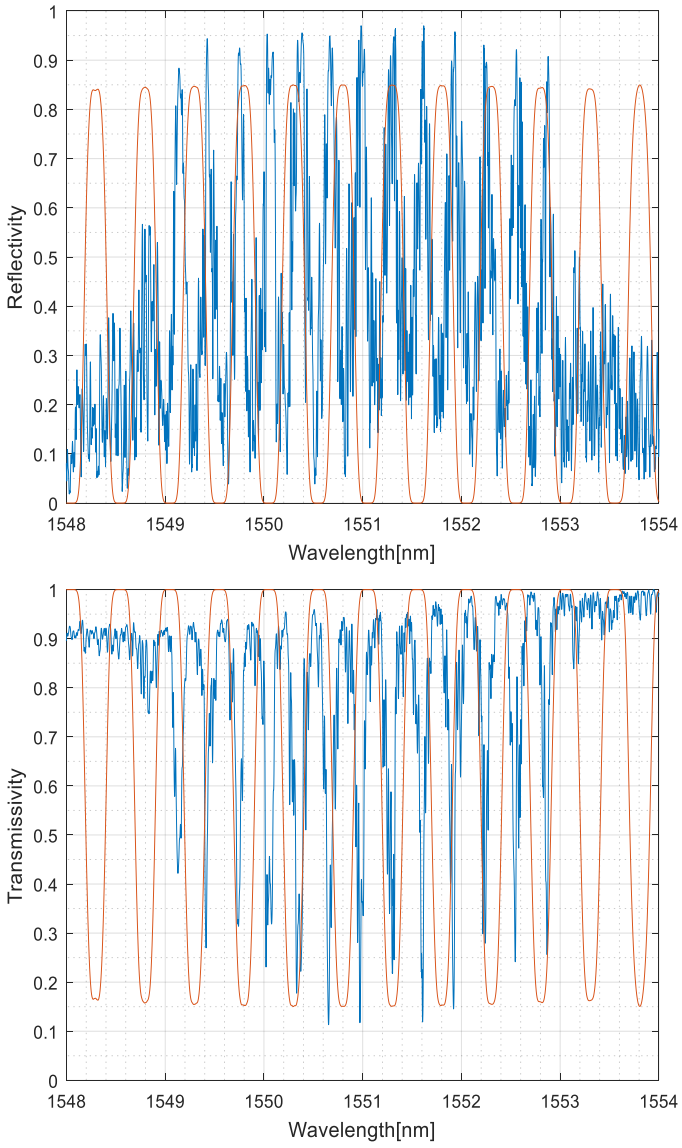

Fig. 3.4: An example of a fibre fabricated for use in the CARDIALLY project (in blue), matching the design (in red, shifted by -0.8nm in wavelength for comparison) file.

3.1.2. Inscription system in the new laboratories

Following the relocation of the fabrication system to new laboratories, multiple changes have been made to the fabrication system. The same capabilities described above remain in place, though the option of fabricating via an alternative means has been added. The placement of an optional mirror

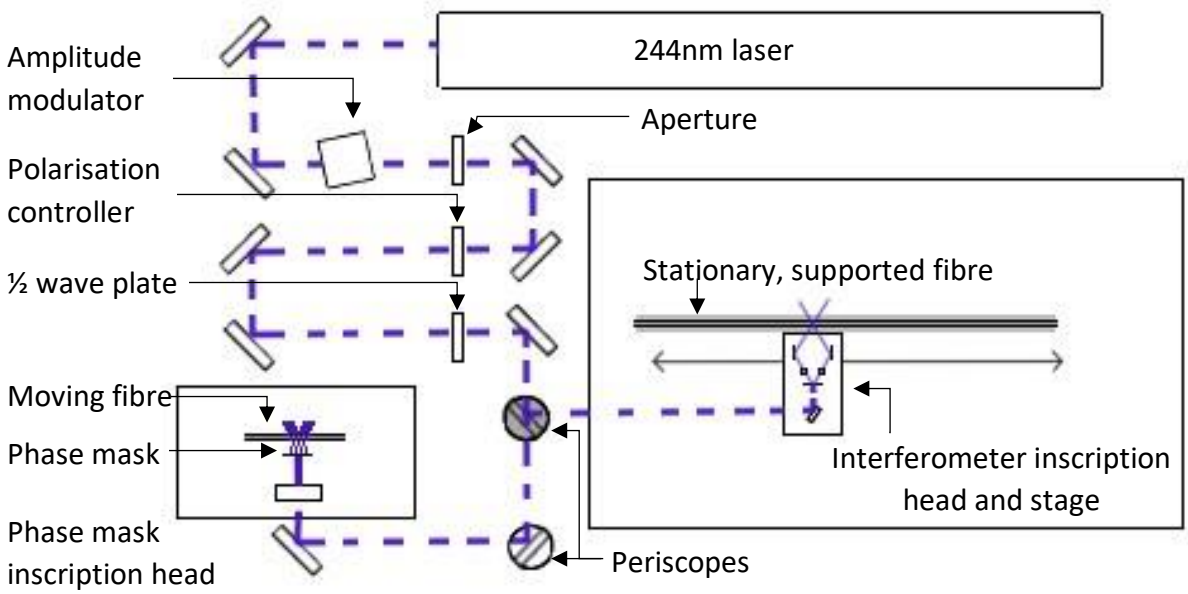

Fig. 3.5: The inscription setup in the new laboratories, showing beam control components, the two inscription heads and the location for selecting the inscription head to use. The greyed out periscope signifies an optional mirror for use when selecting which inscription head to make use of.

redirects the beam post-control to an alternative inscription head that employs the interferometer technique.

This alternative inscription head is mounted on a 1m translation stage, enabling longer gratings to be fabricated than the old system, though has a small number of final adjustments to be made for full functionality to be claimed. Presently, the head makes use of a setup resembling that of Fig. 2.5 with mounted mirrors redirecting the beams to intersect at the fibre's location. This head moves along the translation stage, scanning across a stationary fibre, which is supported to reduce sagging and the resulting blazing effects on the grating. The method for supporting the fibre is in the process of consideration at the time of writing, with potential methods including glass capillaries to additionally protect fibre sections not being exposed at a given moment. The prevention of sagging of such a capillary could be assisted by freely rotating supports or a similar system for supporting the fibre section in line with the inscription head at any given time.

Other methods for countering fibre sagging across such a length have been developed, including the tracking of the fibre position and use of a two-axis translation stage to follow the deviation of the fibre's position, moving the inscription head to maintain the inscription zone's presence over the fibre [65, 73].

The addition of motorised rotation stages for the mirrors is the next stage for completion and will require a program to be written to integrate it into the fabrication system for full control. Considering the rotation error of the rotation stages, a grating precision of less than 0.01nm in the central wavelength can be met.

To enable the smooth writing of the grating as the inscription head scans the fibre, a pair of phase modulators, one in each arm of the interferometer, will be added. These will be controlled with a saw tooth signal to account for the shifting head and ensure the interference pattern on the fibre inscribes the correct grating structure. The use of two phase modulators enables a precise control of the interference pattern, allowing for adjustments to be made to each arm simultaneously for an effective phase difference. Via this method, the effective phase difference between the two arms can be adjusted at an accelerated rate in comparison to the use of a single modulator, thus enabling a larger variety of translation speeds for the interferometer head. A stage position feedback may be applied to the phase modulators using the same technique as for the AOM. The precision of which will depend on the functioning of the stage upon testing. In this case, the position will affect the output phase of the beam based on the relevant point in the signal pattern. More details on this inscription head can be found in section 3.3.

As with the use of the amplitude modulator in the old inscription setup, the pair of phase modulators within the inscription head may have their modulation rate adjusted to adjust the translation of the fibre relative to the beam without affecting the inscribed grating via erasure. This has an advantage over the use of the AOM in that the task can be performed with continuous inscription, instead of an on-off modulation that reduces the exposure time over a length of fibre. As the phase modulators perform the same task as the AOM, there is no requirement to use both together in a system. Fig. 3.5 presents the location of the AOM for situations where the original phase mask head is in use. For the use of the new interferometer head, modulation via the AOM is not required, needing either the unadjusted transmittance through the amplitude modulator or a system for temporarily removing it from the beam path.

As well as the physical additions to the setup, the integration of the feedback system, described in section 3.2, can be established once the basic fabrication abilities of the system have been confirmed. This will allow for observations of the grating's fabrication to be compared to the expected grating at the relevant point in inscription and, if necessary, adjust the design of the remaining grating to correct deviations that result from fabrication conditions or fibre irregularities.

Old inscription system	New inscription system
Translation stage- up to 10cm gratings	Translation stage- up to 1m gratings for interferometer head
Stage position monitoring	Multi-method stage position monitoring
Phase mask head	Phase mask and Interferometer head
	Feedback technique

Table 3.1: Changes and additions to the inscription system from prior to (old system) and after (new system) the relocation to the new inscription labs.

In combination with the option to choose inscription head, the feedback system will allow for flexibility whilst further ensuring the accuracy of fabricated gratings with respect to the design file. This will open the possibilities for a wider variety of gratings to be fabricated by AIPT and therefore progress research into the applications for a greater variety of fibre gratings and structures.

3.1.3. Grating measurement

Throughout this report, measurements taken have been mainly performed via a LUNA Optical Vector Analyser 5000 (hereby referred to as “LUNA OVA” or “LUNA”). This monitors the gratings through fibre optic interferometry. Within LUNA is contained a pair of Michaelson interferometers, one for measurements and one used for triggering.

The device under test (DUT) is added into one arm of the first interferometer and is described by the phase and a linear transform in the frequency domain. The OVA is designed so that, even in the case of extremely short DUTs, the initial path delay in the DUT arm of the interferometer is long enough to prevent low frequency terms influencing the measurement and therefore prevent dead zones in measurements.

By sweeping through a range of wavelengths and measuring the response in the time domain to determine the Jones Matrix elements, particular aspects of interest can be found, such as the insertion loss, the group delay (the derivative of the phase response) and the chromatic dispersion (as the derivative of the group delay), which may be used to describe many aspects of the spectral response and which can be stored in a concise way. As the raw data is acquired in the form of four interference fringes over two detector channels in order to appropriately characterise the Jones matrix, the two fringes on each channel must be separated. This is performed by using the length of the DUT to place two selection windows for each of the two channels, each over one of the impulse response peaks. An incorrectly set DUT length will misplace the windows, either shaving off some of the impulse response peak or leaving one or both peaks entirely outside the windows, leading to inaccurate data collection.

A method for LUNA to automatically find the DUT lengths exists, which determines the DUT length close to the correct setting, with a slight manual shift in the value required on rare occasions. Since the location of the impulse response locations are determined by the delay through the DUT rather than the length specifically, using a refractive index of 1.5, the DUT length value may be slightly altered to the physical length of the device.

Once the windows have been set, aspects of the spectra such as the insertion loss, the phase response and a describing Jones Matrix can be accurately characterised. From these raw aspects and the Jones Matrix, a large number of features of the spectrum can be calculated, describing the DUT. Plots of measured gratings in this report have been formed from data gathered in this way as well as aspects of grating measurement for feedback processes thus far.

In the case of the inscription system employed in this report, each end of the fibre is connected to a LUNA OVA during writing. A continuous measurement of the insertion loss, or other relevant aspects in need of monitoring, is taken over the course of inscription, allowing for observations over the grating’s formation to be made. Measurements are recorded upon completing inscription prior to and following annealing for initial analysis and as a record of the grating’s state at this point. As described in more detail in the chapter covering feedback, this continuous measurement of the grating during inscription is employed for acquiring data used by the feedback technique for monitoring the writing process.

Luna measurements in this report are taken with a wavelength resolution of 1.28fm and contain a number of points in the thousands, the exact number being dependant on the wavelength range chosen to record each grating. This reduces the probability of a narrow peak in the data being located primarily between two data points and helps to ensure that local maxima and minima are displayed with an appropriate accuracy.

3.2. Fabrication using a feedback algorithm

The potential to observe a grating during fabrication and identify how closely it matches the original grating design is an achievement that would enable gratings to be fabricated much more closely to the intended design than before through countering errors in fabrication [74]. Should a grating's spectrum be observed to deviate due to an error in the initial setup, imperfections in the fibre or other cases, an automatic correction to this change to bring the spectrum back into line will result in fewer iterations of a grating to counter such errors.

The concept of a feedback process in the fabrication of FBGs works off a few steps that work in addition to the current fabrication process. These steps are as follows:

1. Acquire data regarding the transmitted and reflected spectra of the grating as it is being fabricated.
2. Compare this data to what the spectra is simulated to look like at the current point in the inscription process.
3. Calculate what changes are required to "correct" any variation and bring the fabricated grating closer to the original design.
4. Adapt the fabrication design to incorporate the calculated changes.

These four steps are repeated until the inscription process is complete.

In order to maximise the impact of feedback and to ensure the calculated changes are relevant at the point that they are implemented to the design, the entire process must be streamlined to run as swiftly as possible whilst maintaining stability. Should each iteration of the feedback loop take too long, then by the time the calculated changes to the system are made, it would no longer be the most efficient way to correct the design at the point of implementation. Should the fabrication process run exactly as intended then the feedback loop would act to monitor the inscription, seeking any variation from the initially designed grating.

In addition to this, changes must be made to the current setup to enable the feedback processes to function and affect the inscription. The nature of the changes in the corrected design may result in aspects such as the final length of the grating altering, which the system in turn must be flexible enough to perform. By extension, the manual preparation of the system prior to inscription must also be flexible enough. In the example of the grating length, such a precaution could be an extension of the section of fibre stripped of its coating. With knowledge of what changes the feedback system makes to a grating design during fabrication, such alterations to the system and manual processes can be more reliably defined.

Such a process for monitoring the inscription stage in fabrication would improve the accuracy of fabricated gratings in comparison to the initial design for the grating. Not only would it allow for a correct grating to be fabricated in fewer iterations, it would also enable more complex designs to be fabricated, where any variations from the initial design would severely affect the grating's spectra.

Within the process of creating a feedback system, the task of creating a set of LabVIEW VIs for the acquisition of the spectra during fabrication was assigned. The results of which at this time are described below. The remainder of the feedback system was worked on by Dr. Adenowo Gbadebo, with information regarding data transfer between the sections being discussed to ensure smooth designing.

3.2.1. Remote control and interrogation via LUNA

One of the key tasks in implementing a feedback process in grating fabrication is the gathering of measurements relating to the grating during inscription. In order to pass on the data to programs to compare to the grating design, there must be a method for connecting to lab equipment and not only commanding a scan but retrieving the data from the scan.

In this case, a series of LabVIEW virtual instruments were created to remotely control a LUNA Optical Vector Analyser. This was performed via a TCP/IP connection between the VIs and the LUNA control software. Whilst the work upon designing the VIs connected the two systems on the same computer, the same tasks can easily be performed with VIs on another computer that can connect to the hardware running the LUNA control software. This could be done as part of the TCP/IP connection with correct referencing of components.

Several aspects must be considered when using TCP/IP to control LUNA. The main two being the need for every VI to run smoothly and as swiftly as it can, a key requirement for real-time functioning and feedback, and the knowledge of the data being sent and received. Since all data received from LUNA via this method is transferred as a string, most data must be converted into the relevant data type within the VIs. This not only allows for processes within the VIs to function but is also a requirement for the comparison programs the data will be moved onto.

The availability of functions within LabVIEW for establishing a TCP/IP connection as well as the TCP Write and TCP Read functions, for sending commands and receiving responses, greatly simplified the process for creating control VIs for this task. Beyond forming the connection, the main requirements relating to the LabVIEW TCP/IP functions related to the number of bytes to read when receiving data. If this is not matched appropriately, then data received over the course of several command responses may spread onto following responses, causing issues in data verification and analysis.

Within the software created for controlling LUNA, three VIs served to perform the processes required by this stage in the feedback process. In addition to these three, an extra VI was employed for simple one-command-one-response test purposes. The main VIs will be briefly described below and the aims and purpose of each explained.

TCP Controller Settings

This VI is used to control pre-scan settings on the LUNA OVA, particularly, settings that will likely be unchanged during a scan, though incorporation of aspects of this VI may be used to control settings during fabrication between scans. Settings controlled by this VI include:

- Central scan wavelength
- Wavelength scan range
- Measuring transmission or reflection (as LUNA can only scan one of the two at any one time)
- Whether an average should be taken over several scans and how many scans should be taken for this.

In addition, the VI performs checks to test if LUNA is functioning at its optimal operating temperature and to find the DUT length prior to any scans. A confirmation of the settings is presented for manual validation prior to closing the connection.

TCP Controller Scan and Plot

The VI that runs during the feedback process, Scan and Plot commands LUNA to perform scans and retrieves scan data, formatting it for use by other programs in the feedback process. In its present

form, this VI also plots the scan data and displays it for manual confirmation of the scan results, a useful addition for monitoring the formation of a grating visually for the user.

Since all data received from the scan is in a string, Scan and Plot must convert the data into arrays that can be used for plotting and comparison. Careful analysis of the string format was required to ensure the correct conversion of data type. The VI scanned results have been compared to measurements taken whilst manually controlling the LUNA software to validate that the conversion method does not affect the data values. Conversions from the strings received from LUNA are performed by a series of subVIs written for the responses to LUNA commands, which provide not only the scan data itself, but useful information on the scan such as the DUT length and the number of averages successfully taken in the scan (which may differ from the averages set in the previous VI if errors occur in the scans). This data is passed onto the main feedback programs for analysis, having been converted to the relevant forms.

TCP Controller Save

This simple VI currently runs separately to the others and saves the scan data into two file formats, a text file and a binary file. The two files created mirror the format of saved data upon manually saving with the LUNA OVA software and together record almost all data gathered in some form. Due to the simplicity of this VI, it could easily be added as a sub-VI within Scan and Plot with some minor adjustments to smooth the passing of relevant data. It is presently kept separate as the ability to save a single scan whilst the feedback process is running has less of a priority than ensuring the smooth functioning of the entire system post-integration. Regardless, this task is useful during tests for the feedback process and the VI for quickly saving data has been created should it be deemed a useful addition to the feedback process.

This VI allows for the saving of relevant data in a form that can be recalled later on for analysis and research. Plots later on in this report relaying data from a fabricated grating are derived from the data forms this VI saves in, with no changes in analysis functions required between saving manually with the LUNA software and through this VI. In this regard, this simple VI does what it is required to do in a method that can be performed very swiftly and potentially at any point within a feedback process.

3.2.2. Integration of LUNA interrogation with the feedback and fabrication systems

The process described above is looped at a rate as close to the feedback process's iteration runtime as can be achieved. Once the full fabrication system is running, including the integrated feedback process, the efficiency of the VI shall, if necessary, be improved to bring its runtime to under that of the rest of the feedback process. An appropriate match of these two runtimes will prevent the build-up of scan data and the presenting of old (and by that point in fabrication, potentially irrelevant) data whilst ensuring that data is always at hand for the remaining feedback process.

Due to the relocation of the inscription setup to the new labs and subsequent delays, tests on the functionality of the feedback system have not been fully performed, though much of the system is in place with respect to the software and the physical fabrication system.

At present, the feedback system is designed to run for the phase mask inscription method, which will be the primary inscription head used to test the feedback system prior to the development of an adapted version for the interferometer head, described in section 3.3. Potentially, a simple alteration of one setting of the main feedback system control to determine which inscription head is

to be used would select VIs for relevant head-related control rather than creating two separate systems. Such a setup would require a modular aspect to the feedback system where the VIs for controlling the relevant inscription head could be called, though this option would require the feedback system to be designed to allow this and would be more difficult to achieve as a later feature.

3.2.3. Fabrication feedback system conclusion

The creation of a method to enable an automated measurement of the grating spectrum during fabrication has been performed, completing a key aspect required for a feedback-based correction of gratings being inscribed. The process presently issues commands to the software controlling a LUNA OVA as well as retrieving the data and converting it to a format that may be used by the feedback system as a whole.

Whilst testing of this aspect of the feedback process as a part of the entire fabrication system requires performing, this is a priority for once the fabrication system is operational. Once feedback influenced gratings have been written for comparison to gratings written by the old system, the improvements will be able to be observed. This will also reveal any further improvements to the feedback system's efficiency and whether the monitoring system described above requires alterations to enable this.

3.3. Creation of an interferometer head

One aspect considered as part of integrating the feedback process is the potential adaptation of the programs to enable the use of it through multiple methods of FBG fabrication. Should this be achieved, it would not only prove the potential for the feedback process to be widely applied in FBG fabrication but would also highlight changes that would be required for its use with the remaining inscription methods and assist with refining the feedback process. The first of these advantages could specifically assist other sections of AIPT working with inscription and increase the quality of gratings made. Additionally, the use of the interferometer head method would assist with the control of beam size, which is a useful factor when writing multi-channel gratings.

This alternative head to the phase mask inscription head described above is presently mounted on a 1m air-bearing translation stage. This provides an extension to the maximum length of grating that can be inscribed, up from the 10cm limit with the present phase mask head. Early tests have been performed using a green laser, showing the capability of the early pre-motorised version of the head to recombine the beam pair over a chosen point with an easily observable beam. Given the dependence on wavelength for the angles a phase mask induces, the angles resulting from this laser differ from that of the 244nm laser used for inscription.

Motorised rotation stages for mirror control are presently in the process of purchasing, which shall improve the interferometer head's precision in comparison to the present mirror stages as well as enabling an integration into the feedback system. The potential for commanding these rotation stages via a feedback-controlled automated process would complete the integration of this head with the rest of the system, simplifying the mirror alignment task for the user.

The selection of these motorised rotation stages involved careful consideration in order to allow for the required precision of rotation, therefore the required maximum offset in Bragg wavelength. To achieve this, the resolution of a set of motorised rotation stages were used to calculate the Bragg

offset that could be expected. The same process was also applied to a range of manual rotation stages, for comparison and in the eventuality that a manual stage met the resolution requirement.

The technique for observing the Bragg offset involved a simulation of the interferometer set as if fabricating gratings with Bragg wavelengths of 500nm and 2000nm (to observe the boundaries of fabrication) and 1550nm (the most frequently fabricated Bragg wavelength). A change in the angles for these fabrications of the same magnitude as the rotation error of the stages was applied and the change in inscribed Bragg wavelength was noted. These values were compared to a desired precision for the interferometer head of 0.01nm, ruling out all but three of the motorised stages and all of the manual stages. From this point, aspects such as the cost for the stages and required components as well as the dimensions of the stages were considered before a single rotation stage design could be chosen. The result of this is the selection of the Thorlabs PRMTZ8 for use within the interferometer head, with a resultant potential error in Bragg wavelength of 0.00323nm. As well as providing a higher precision than manual rotation stages, the selection of a motorised stage also enables a link to the inscription feedback, as any offset at the start of inscription may be observed and, if necessary, corrected by the system itself.

The motorised rotation stages incorporated into the interferometer head make use of a LabVIEW VI to calculate the mirror rotation that provides the required beam intersection angle to inscribe a grating of the desired wavelength. This makes use of the equation:

$$\theta_{mr} = \frac{(90-\theta_{pm})+\left(90-\frac{\theta_g}{2}\right)}{2} - \left(90-\frac{\theta_g}{2}\right) \qquad (3.4)$$

Where θ_{mr} is the angle the mirrors should be rotated (with 0 being the two mirrors parallel to each other) to provide the required intersection angle, θ_g. θ_{pm} is the angle of the first order diffracted beam by the phase mask. A diagram of these angles is provided in Fig. 3.6. This mirror angle is provided to both stages, with each applying this angle in opposite directions to recombine the beam.

Referring back to equation (2.41), the dependence of the inscribed wavelength on the intersection angle is clear, displaying how the angle of the mirrors in the interferometer head can achieve an arbitrary wavelength.

$$\lambda_g = \frac{n_{eff}\lambda_{UV}}{n_{UV}\sin\left(\frac{\theta_g}{2}\right)} \qquad (3.5)$$

Where λ_g is the designed wavelength for the grating, n_{eff} and n_{UV} are the effective refractive indexes of the fibre over the course of the grating and of the fibre relating to the UV writing beam respectively, λ_{UV} is the writing beam's wavelength and θ_g is the angle of one of the incident beams.

The distance between the point of intersection and the mirror line, determining the required location of the fibre relative to the inscription head, as well as the grating wavelength to be inscribed using the physical intersection angle are both provided for reference. In addition, a method of nudging the stages has been applied to enable repeated attempts at acquiring an adequate intersection angle, should the initial rotation not be accurate enough. This feature was added following the observation that the PRMTZ8 stages do not always rotate to a precise position for small rotations (angle changes of less than 10° seem to pose such a risk), though posed more reliability for larger motions.

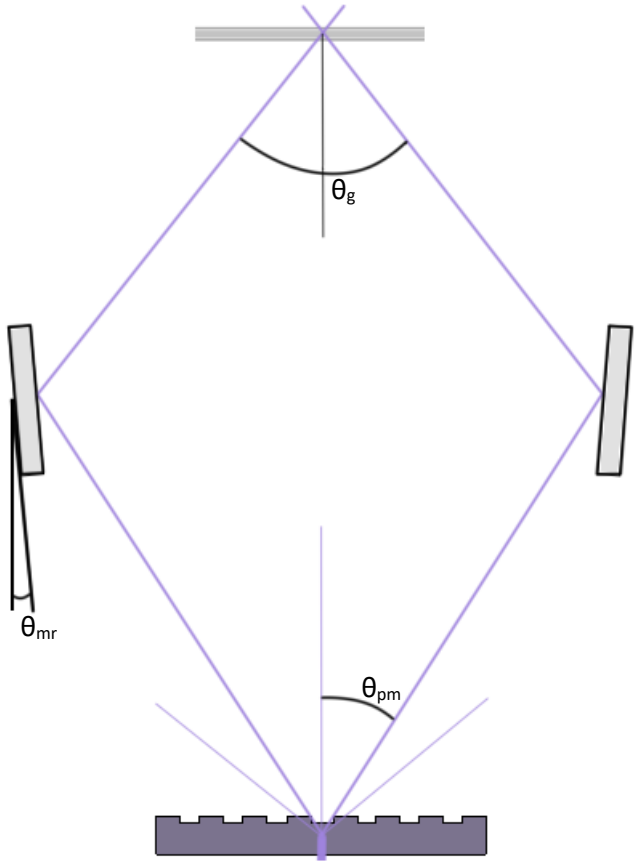

Fig. 3.6: Diagram of the angles involved in the interferometer head, showing θ_g, θ_{pm} and θ_{mr}

The inclusion of a pair of phase modulators will be made, one in each arm of the interferometer. A saw tooth signal sent to each of these modulators will enable a mitigation of the effects of moving the head relative to the fibre during inscription, as the amplitude modulator does. Unlike amplitude modulation, the use of these phase modulators will enable the beam to be continuously inscribing, increasing the effective power of the beam in comparison to one that is cyclically blocked. This is due to the phase modulators creating a moving fringe over the fibre, which repeats periodically, returning to the original phase before repeating. Should the inscription head's translation speed be matched to the motion of the fringe, the fringe will effectively remain stationary on the fibre allowing for a continuous inscription over an extended distance. It is worth considering when designing the signal controlling the phase modulator that the return of the crystal's dimensions to the initial phase value is not immediate. This a matter of importance for fast inscription speeds, as the relative portion of the crystal's return contraction within the period increases as the signal is altered to enable increased inscription speed.

The pair of phase modulators used in the interferometer head in this thesis can each delay the phase of an inbound beam by π, with the pair enabling a shift of up to 2π when used together. For a simple, uniform grating the pattern of phase shift induced by the modulators follows a sawtooth pattern provided to the modulators for controlling the electric field and therefore the crystal and phase. Following this technique, the phase modulators can enable a grating of a given wavelength to be inscribed over a longer length than otherwise could be achieved. By adjusting this phase shift pattern relative to the pattern for a given beam scanning speed, aspects such as chirp and apodisation may be achieved via mild erasure of relevant sections, adjusting the coupling coefficient that would describe the relevant sections of the grating. Similarly, phase shifts in the grating can be

formed by altering the inscribing beam's phase at the relevant point in the grating and then returning to the original pattern for the grating's inscription. This would result in a grating design with a change in one location that causes a phase shift, returning to the original design afterwards.

Phase modulators that function appropriately at 244nm are difficult to produce, as the crystals that are transparent to light of this wavelength often have limited control of the phase and are hygroscopic. For the phase modulators to be added to the interferometer head, β-Barium Borate (BBO) crystals are used to modulate the beams. BBO crystals are of use in this case as they have a wide transparency range of 189-3500nm [75] as well as a high damage threshold of 1GW/cm^2 (for a 10ps pulse-width at 532nm). This, and the mechanical and physical properties of the crystal [75], makes BBO a good candidate for modulating a 244nm beam within a phase modulator.

The development of this interferometer head will be of benefit to the fabrication system once fully integrated, enabling a greater variation in wavelengths that a grating may be fabricated at as well as the length of gratings. Greater control of the orders diffracted by the phase mask will also be possible in comparison to the phase mask head, which due to its nature has none besides any suppression of orders by the phase mask itself. Mounting the interferometer head on a 1m air bearing translation stage enables full advantage to be taken of the interferometer technique's ability to inscribe longer gratings, allowing for much longer gratings to be fabricated than with the old system.

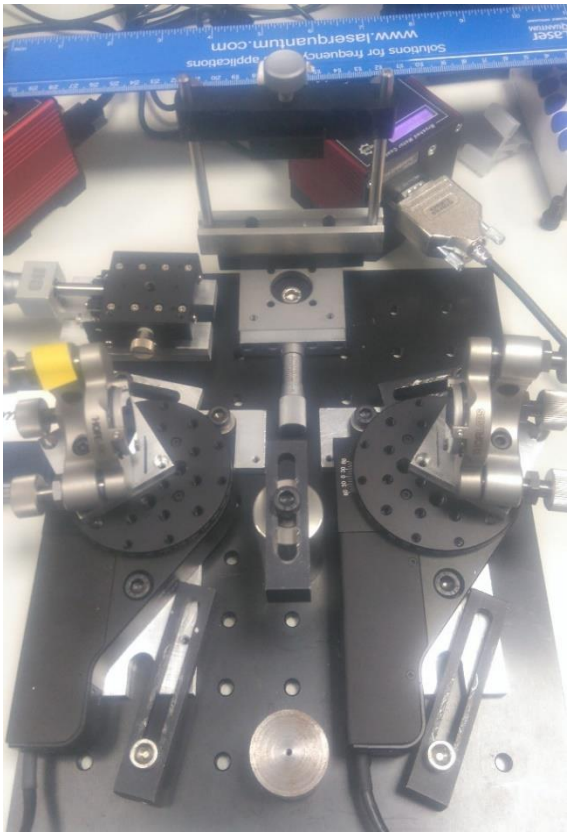

Fig. 3.7: The interferometer head at its present state at the time of writing. Visible are the pillar for the phase mask (bottom), the two mirror stands, mounted on PRMTZ8 rotation stages (right and left), a holder for a cylindrical lens (top) and a pillar to block any 0th order refraction from the phase mask (centre, may not be required dependant on phase mask choice). The fibre will be located on the far side of the head in this view (in line with the ruler in the case of the mirror positions shown in the diagram) to be supported as the laser scans across it. The phase modulators will be placed between the mirrors and the lens position, on top of one-dimensional translation stages (one of which is presented in the top left for visualisation).

3.4. Additional aspects in fabrication

As well as the inscription of the gratings themselves, several other experimental aspects have been focussed on that form part of the work done around FBG fabrication. This includes the precise measuring of the gratings once the added hydrogen has been expunged, organising the preparation of fibres prior to inscription and gaining a knowledge of the system as a whole through observing maintenance of it.

Fundamentally, the measuring of the gratings after inscription has little variation from measurements during inscription. Both rely on the use of the LUNA optical vector analyser to gain readings of the transmitted and reflected spectra and other properties of them, an aspect which may be controlled by a version of the VI presented in the feedback section for measuring during inscription. The differences lie in the steps taken beforehand and the precision of the results.

The removal of the hydrogen post-inscription would not affect the transmitted and reflected spectra to a great degree but may cause a slight change in the refractive index of the fibre itself. In addition to this, a reduction in error is gained via the method for attaching the fibre containing the grating to the OVA. Instead of a connection which aligns the ends of the fibre to ensure passage of the spectra between fibres, which is sufficient for during the inscription process itself, the post-inscription measurements make use of splicing the grating's fibre to reduce loss at the connections. This greatly impacts the continuous error in transmission, caused by loss of light at fibre connections, and ensures that the error itself is stable as any movement of the fibre is unlikely to affect the join or alignment of it. Through use of splicing to measure the FBGs after the hydrogen is removed, a precise set of measurements of the fibre can be made to confirm those made just after inscription. Aspects of this technique may also be applied to any measurement of gratings in order to reduce errors and the ability to utilise splicing is of importance in many areas regarding optical fibres.

3.5. Conclusion to fabrication system improvements

The inscription system has been improved with the addition of not only an alternate inscription head but also by the inclusion of a feedback system for monitoring grating fabrication. The increased flexibility in gratings that may be fabricated by the new system will enable a wider range of advanced grating research to be possible, as the range of gratings and grating length offered by the interferometer head and its translation stage may be chosen in place of the repeatability of the existing phase mask head. In combination with this, the use of a system to monitor the gratings during fabrication and compare them to the anticipated grating at the given time has also been discussed, in particular work performed on an automated method for monitoring the spectra of the gratings being inscribed.

The combination of these two factors will result in an improvement not only in the variations of gratings the system is capable of, but also in ensuring the fabrications match expectations with the requirement for fewer iterations of the grating. Such improvements will be thoroughly tested once the inscription system is fully operational, a process which is close to completion as of the time of writing.

3.6. Split grating fabrication

3.6.1. Introduction to split gratings

One aspect of grating fabrication with potential advantages to gain is the splitting of a grating design into an array of grating sections, which together replicate the original grating design. If successfully achieved, this would enable gratings that would normally be too long for fabrication to be split into smaller sections to be inscribed separately, thereby enabling a range of physically long gratings to be made on a system that would otherwise be incapable of the task. An extension of the length of gratings that can be written by splitting it would also enable more complex designs, requiring this length to function, to be fabricated on current systems without the need to redesign sections of it to accommodate longer fibre gratings.

The design of the split gratings used in this section mirror the general appearance of phase shifted gratings, albeit with much larger spaces between grating sections. These gap lengths are of such a size to enable the fibre to be shifted and be clamped in a new location to continue inscription of a long grating in multiple sections. Therefore, the shift in the fibre's position for a split is dependent on several aspects, including the length of grating sections, the number of sections the grating is split into, the width of fibre clamps and the distance between the fibre clamps.

These longer gaps provide a variation of a phase shifted grating that is more challenging to accurately control the resultant phase shift and provides a much greater effect on the spectrum. The system could be considered in a similar way to a Fabry-Perot resonator within the fibre, with each grating acting as a mirror. In this case a system of, for example, three grating sections could present a challenge to compensate for without reliable simulations.

In order to achieve a simulation of a split grating system, a MATLAB function was created to split a grating design into several sections. A resulting example of a split grating array was derived from this and put through the same simulation programs used for more general designs to test how the gaps added into the split gratings might affect the final design. At this point, a decision could be made on the viability of this technique for fabrication purposes and whether deeper research would be beneficial at this stage.

Section 3.6.2 details the processes regarding splitting gratings and investigates the viability of this technique. Whilst it was found that splitting gratings is currently unlikely to be viable, aspects to be considered should this be investigated again have been found and are discussed below. In addition, the research performed in this area contributed to the development of the nanoparticle detection system simulations discussed in section 3.7.

3.6.2. Methods for modelling the split grating function

To generate the split gratings, a function was written in MATLAB to allow for a grating to be divided into a given number of sections with a specified length separating each one. Starting from the initial design of the chosen grating, the number of data points of each grating section is determined based on the length of the un-split grating and the number of sections it is to be divided into. This information is used to split the grating design into the desired sections, stored within a cell array in preparation for re-assembling further on.

A similar method is used to generate an array of zeros to take the place of the gaps in the split grating design. Once the number of data points corresponding to the desired gap length is determined, a zero array is formed. The grating design is then re-assembled with a zero array being

placed between each grating section to form the gaps. The calculation to determine the number of data points within the zero array ensures that the concentration of data points over the new split grating design's full length is constant.

In order to ensure the split grating design could be correctly plotted and fabricated, the column describing each data point's position along the grating required redefining. To do so, the total number of data points and the length of the new grating are defined and from this, a new length column is generated. The redefining of equally spaced data points along this new split grating's length ensures that the gaps are included in further processing of the new design. Finally, the new split grating is plotted to allow for manual checks and the new grating design is saved in the same format as the original design, thereby enabling the split grating to be presented to the same simulations as the original design for comparison.

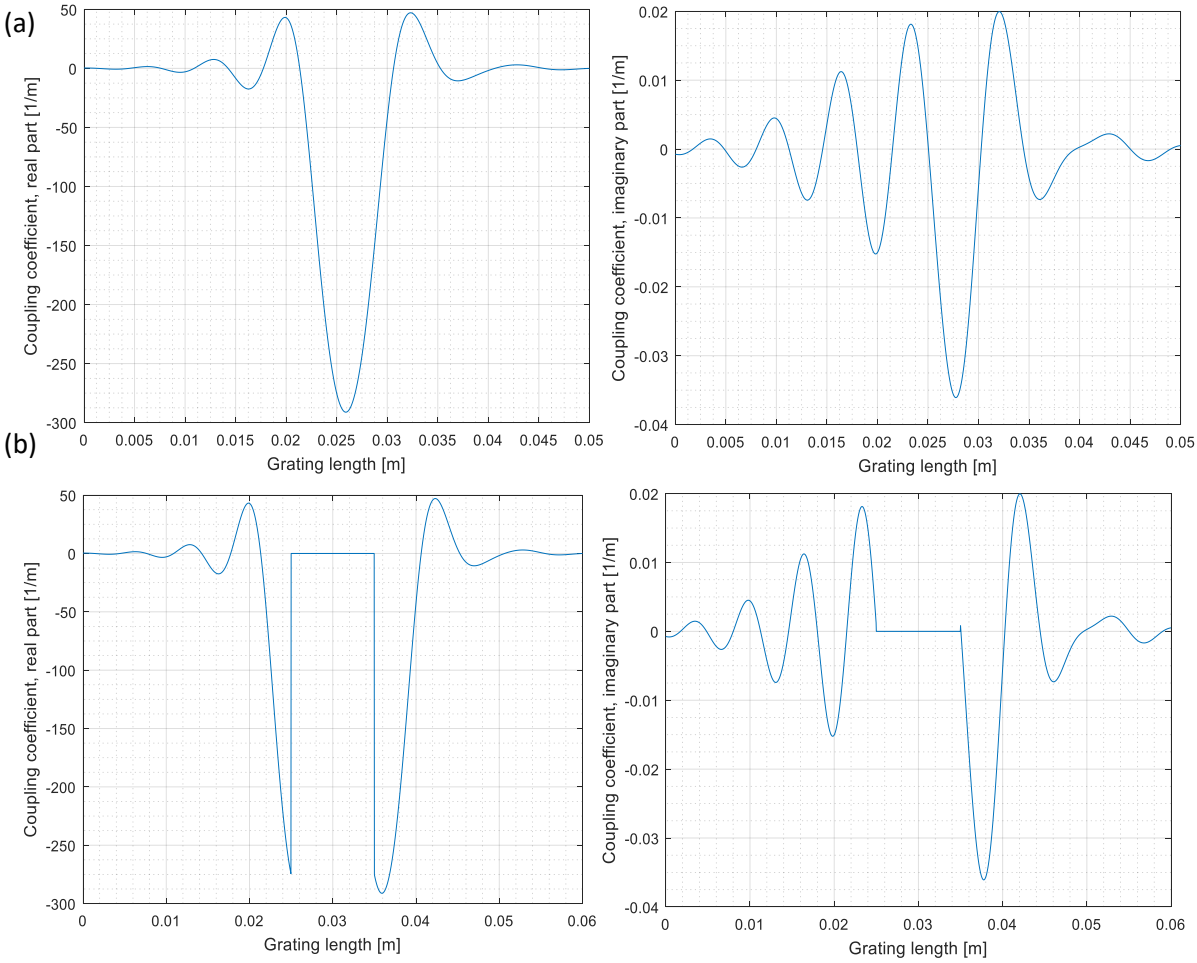

Fig. 3.8: Simulated grating coupling coefficients before (a) and after (b) being split with the function described above. In this case, a 1cm gap has been introduced to the centre of the original 5cm design. The original design was designed with a reflection coefficient of 0.8, a bandwidth of 0.2nm, a Gaussian order of 8 and a dispersion coefficient of 0. The total grating length for the un-split design was 5cm and 6cm for the split design.

The current technique for splitting gratings successfully performs its function, though it does have its limitations and disadvantages. For example, the method for generating the gaps leads to a large number of effectively value-less data points that result in large file sizes for output files. This in turn leads to longer processing times for simulations, especially in cases where large gap lengths are involved. In addition to this, there may be cases where the section lengths or gap lengths are

required to vary across the split design. The splitting function in its present form is unable to provide this variation, though it could be adapted to perform this if required.

3.6.3. Simulations with split gratings

To investigate the viability of fabricating split gratings, both the un-split and the split versions of a grating design were passed through a function that simulates the grating. This function calculates a simulation of the transmission and reflectivity of wavelengths passing through the grating as well as the time delay and dispersion. It also produces an output file that records the data plotted.

As can be seen in Fig. 3.9, there is a noticeable difference in the simulation results when a split is introduced into the grating. This is largely due to the Fabry-Perot effect, as each grating section forms its own spectrum in the results. The edges of each section cause interference with the neighbouring sections, resulting in fluctuations in the overall spectrum. In the case of multiple splits in the grating design, this would occur over several points across the total length.

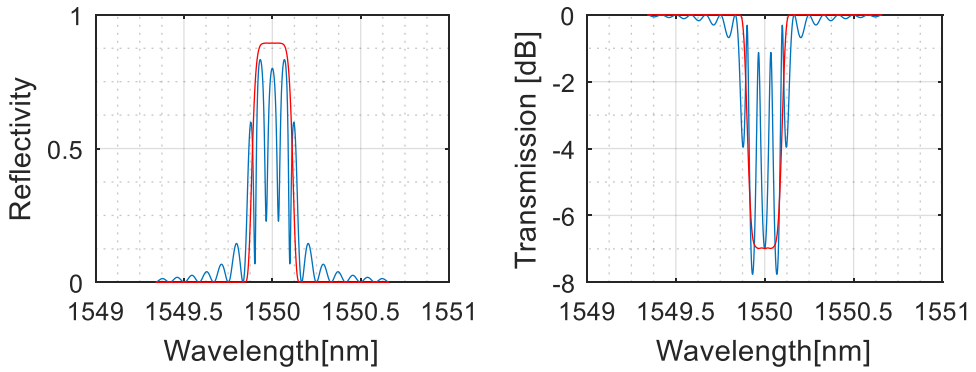

Fig. 3.9: Simulations of a 1cm split (blue) and un-split (red) grating design of 5cm length, demonstrating the appearance of the Fabry-Perot effect in the split grating design and the variation from the un-split design after simulations. The original design was designed with a reflection coefficient of 0.8, a bandwidth of 0.2nm, a Gaussian order of 8 and a dispersion coefficient of 0. The total grating length for the un-split design was 5cm and 6cm for the split design.

The magnitude of the Fabry-Perot effect's impact on the simulated results was observed to vary relating to the length of the gap in the design, with a larger split resulting in a greater impact on the simulation, as displayed in Fig. 3.10. These lengths were chosen to represent expected distances for a grating to be shifted to fabricate a continued section of an elongated design. Working on the example of the old AIPT system's limit of 10cm for fabricated grating length, shifts of 1cm and 5cm demonstrate the range that may separate two grating sections that do not require the full 10cm lengths (for example, a grating design with a total length of 12cm, split into two 6cm sections), considering inaccuracies of manually moving the fibre and re-clamping. For fabricating longer sections (for example, a grating design of total length 19cm, split into two 9.5cm sections), the positioning of the fibre clamps must be considered. Hence, a separation of 10cm is considered to enable the fibre to be held without a risk of damage to the grating due to the clamp. Shorter gaps may be possible for fabrications involving longer sections, though this would involve a minor redesign of the head to reposition the fibre clamps.

The use of such long gaps instead of gaps in the micro or millimetre scale is based on the length of shifts in the fibre required and the repeatability of manually moving the fibre along before re-clamping. The magnitude of the motion that the fibre will be shifted by to inscribe a new section will be in the centimetre scale when considering the old maximum inscription length of 10cm, with the

shift being related to the full length of the grating and the maximum fabrication length of the inscription system. Precision to the millimetre level is possible with a specialised procedure and appropriate measurement aids, though when considering the movement of the fibre to enable an additional grating section length, this will greatly increase the difficulty of attaining such precision.

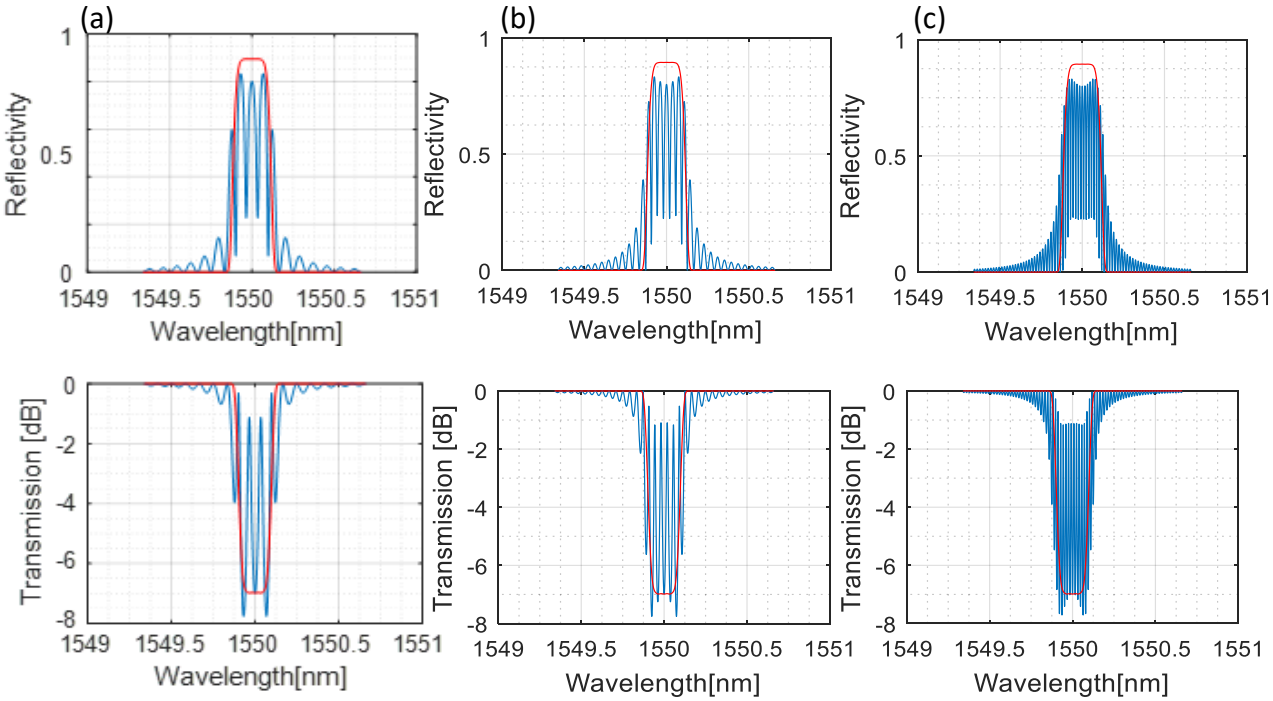

Fig. 3.10: The magnitude of the Fabry-Perot effect's relation to the length of the gap included in the split design on both simulated reflectivity and transmission. The red curves show the un-split simulation (designed with a reflection coefficient of 0.8, a bandwidth of 0.2nm, a Gaussian order of 8 and a dispersion coefficient of 0) with the spit designs plotted in blue. The gap lengths displayed are 1cm (a), 2cm (b) and 5cm (c). The grating design prior to splitting was 5cm in length.

The impact of the Fabry-Perot effect on the simulated results could likely be mitigated if additional work is performed, though that was not done in this report due to time constraints. Without a reliable method for reducing the impact of the Fabry-Perot effect, little further progress can be made regarding splitting gratings at this time. Should this be overcome though, the potential uses for split grating designs would warrant further investigation to achieve. One additional result of the Fabry-Perot effect is the slight reduction in reflection around the central wavelength. This could be compensated for following any countering of the Fabry-Perot effect itself, should it not occur as an aspect of this countering.

To verify the simulated results, a version of this split grating design was fabricated and is detailed within the next section. This fabrication confirmed the appearance of the Fabry-Perot effect, as predicted by the simulation.

3.6.4. Fabrication of split gratings

In order to verify the results of the simulation described above an example split grating was fabricated and measured. This grating design was presented to the inscription software in the form of a single grating, with a "gap" in the centre replicating the split. This method of inscribing the pair of gratings as a single design was chosen to ensure the precision of the gap length. With research into reducing the impact of the Fabry-Perot effect over longer gaps, a tolerance for the variations associated with manually adding gaps (by physically moving the fibre along the setup's clamps

between inscriptions) could be achieved. Though this is presently not possible, therefore requiring this form of split design.

The process of inscription for this grating progressed as expected. The first grating section inscribed acted as a usual grating would, with little variation from an un-split grating. However, as the gap was reached and progressed along, the resulting perturbations from the Fabry-Perot effect became apparent. The resulting changes increased until the end of the gap length, where the rest of the grating was formed as expected, albeit with difficulty in observing this following the result of the gap.

The result of the split grating fabrication confirmed the simulation in that the split in the grating generated perturbations that would be difficult to resolve with current understanding. The variation in magnitude between the fabricated and designed gratings shown in Fig. 3.11 is a result of the fibre used during fabrication. Due to the nature of the other gratings being fabricated that day and the time available for inscribing this example, this grating was fabricated on a length of highly sensitive fibre. The increased sensitivity was not only due to the fibre's added hydrogen, as is the case for all fibres used thus far, but its doping with Boron. This combination of techniques leaves the fibre highly susceptible to inbound UV light, resulting in the changes occurring much faster than in more commonly used fibre. This leaves a much smaller acceptable margin of error for the total inscription time to create an FBG of the correct strength, as the times involved drop from the usual 20 to 80+ minutes down to 1 to 10 minutes. The ease of overshooting the strength of the grating due to this results in multiple attempts to fabricate a design of the correct strength if errors are made initially. The time and length of this fibre available at the time left the option of only a single attempt. The resulting grating, though much stronger than intended, still shows the important features it was fabricated to display, in the form of the Fabry-Perot effect. In the case of this grating, a central wavelength shift of 0.35nm is present, the likely cause of which is discussed above.

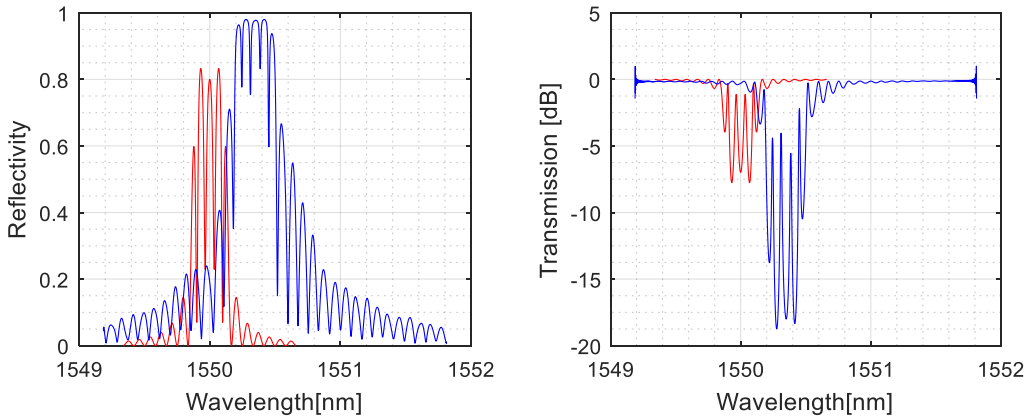

Fig. 3.11: The final fabricated result of the split grating design's transmission and reflectivity (blue), demonstrating the emergence of the Fabry-Perot effect predicted by the simulation in section 3.6 (red). The difference in magnitude in transmission and reflectivity is based on the sensitivity of the fibre used and is described in detail below. The design follows parameters described the previous figures, with a 5cm grating, split in the centre by a 1cm gap, a reflection coefficient of 0.8, a bandwidth of 0.2nm, a Gaussian order of 8 and a dispersion coefficient of 0.

3.6.5. Conclusion to split gratings

This section has looked at the possibility of splitting a grating design into multiple sections prior to fabrication with the aim of enabling a grating to be inscribed in several pieces separately. Software was written to form a split in a grating design, performed in a way to enable the output file to be treated by other programs in the same way as the original design file. Output files from various splits were then passed through existing simulation programs to determine the effect of introduced gaps. An example of a split grating was fabricated to confirm the simulation. This fabrication confirms the Fabry-Perot effect's appearance and is described in detail later in the report.

Given the inclusion of the Fabry-Perot effect upon introducing splits into a grating design, it is currently unlikely that more progress could be made at this point. It has been found that the Fabry-Perot effect is dependent on the length of the gap in the grating design, which would therefore be a main factor to be considered in any attempt to mitigate the variations caused by the gap. Should a technique be found to counter the changes introduced in a split design over a variety of gap lengths, especially for larger gaps, then a method could then be created to correct variations from the initial design over the distances required for fabricating multiple parts of a grating on current systems. Work performed relating to a functioning feedback technique for fabrication could be adapted to generate corrections to a split design to adequately replicate the original design over several sections. This would then achieve the aims of the split grating technique and enable longer and more complex gratings to be inscribed on current systems.

3.7. Nanoparticle detection system

An investigated application for fibre grating structures was that of a potential nanoparticle detection system, consisting of a system of gratings which contains a small bored hole acting as a channel through the fibre core in the centre of the grating system. Any change in the spectrum of the system is to be detected as a nanoparticle passes through, indicating the presence of this particle and if possible, it's size, location or orientation.

Though the structure of a microchannel in the centre of a fibre grating is a topic which has been researched [76, 77], the use of such a structure for the purpose of detecting nanoparticles via the induced effective phase shift has seen a lack of published work. Hence, the focus of this section is the development of a potential use of a microchannel system as a nanoparticle detector through simulations to determine the feasibility of such a system and the precision of measurement equipment required.

Such a system could in the long run find use in the detection of anomalous particles in a fluid, such as a virus, though before such progress is made a proof of the underlying principals is required. Should the orientation of the nanoparticle be found to be detectable, applications such as electromagnetic field detection via an electromagnetically sensitive nanoparticle may also be of interest for further research. In addition, the availability of a method for measuring aspects of an individual nanoparticle such as the diameter and refractive index would provide additional methods for identifying and parameterising particles in a fluid. The ability to perform such a task in a known fluid, such as a contaminant in blood or an undesirable particle in an otherwise risk-laden environment, could also aid in the discovery of the particle's identity with a single test, without the need for a sample to be removed from the fluid.

Other methods of nanoparticle detection exist, including a grating written in tapered fibre which detects the presence of nanoparticles settling on the surface of the fibre due to induced conditions

in the system [78]. This technique differs from the one described within this thesis via the location of the nanoparticles and therefore the structure of the grating. The need for tapered fibre and appropriate extra-fibre conditions in [78] is not present in the method covered below, instead making use of a microchannel that forms a phase shift within an FBG. This leads to a simpler setup for the detection process, requiring only the fibre containing the detector and a fluid containing the nanoparticles.

Another method measures the concentration of particles via the changing refractive index of the surrounding medium, which has been covered in several papers. However, this technique is not suitable for detecting the changes induced by a single nanoparticle as this may not affect the refractive index of the entire surrounding medium [79]. Therefore, the use of this method for detecting individual nanoparticles and properties of them would not be as feasible, instead gaining an overview of the entire fluid and any changes from a normal state.

The method covered below covers the simulation of the transmission through the fibre when a nanoparticle is present within the microchannel. Due to scattering due to the microchannel, modelling the reflectivity of the system back into the path of origin poses a complex task which was not deemed to add enough to create to a high quality. The modelling of nanoparticles smaller than the wavelength of the incident light, via scattering and absorption, has been achieved [80] and could be applied into the model below, though time did not allow an integration beyond applying the principals with respect to transmission. Should this be added in, then it is likely that an alternative method for calculating the change in phase will be required, as the use of the nanoparticle's refractive index gives way in importance due to the nanoparticle size in comparison to the light's wavelength.

The simulation progress described in this report aims to lay the groundwork for this and to create a model that can be used to replicate the physical system, determining if such a concept is feasible.

3.7.1. Nanoparticle detection theory

The principal behind the nanoparticle detector is based on the variation in the spectrum resulting from the presence of a nanoparticle within a base detector system. In order to achieve this, simulations of the base system must be created using principals described in this section. The concept is based on the idea of observing the changes in the system's transmission spectrum that occur as a result in the change in optical path the nanoparticle induces.

The main structure of the detection system is based on that of a Fabry-Perot cavity. A pair of matching uniform gratings located in close proximity with a bored hole located between them and passing through the fibre core, as displayed in Fig. 3.12. This cavity is simulated as having a diameter of 1µm, though as described in section 3.7.5, present fabrication techniques will have difficulty in achieving this. The behaviour of the spectrum given a change in the cavity's size is discussed in section 3.7.3 to counter this point.

The spectrum passing through a pair of gratings arranged in close proximity to each other, resulting in an optical phase shift, creates in an interference between the two gratings. In the case of two uniform gratings of the same design, this leads to a series of constructive and destructive regions in the spectrum, as observed in section 3.6. This spectrum form contains multiple identifiable areas which may be observed for alterations resulting from changes in the core in the vicinity of the

structure. Such locations can be made use of via the shifts in the wavelengths they occur at and the subsequent change in maximum reflectivity at the peaks either side of the chosen points.

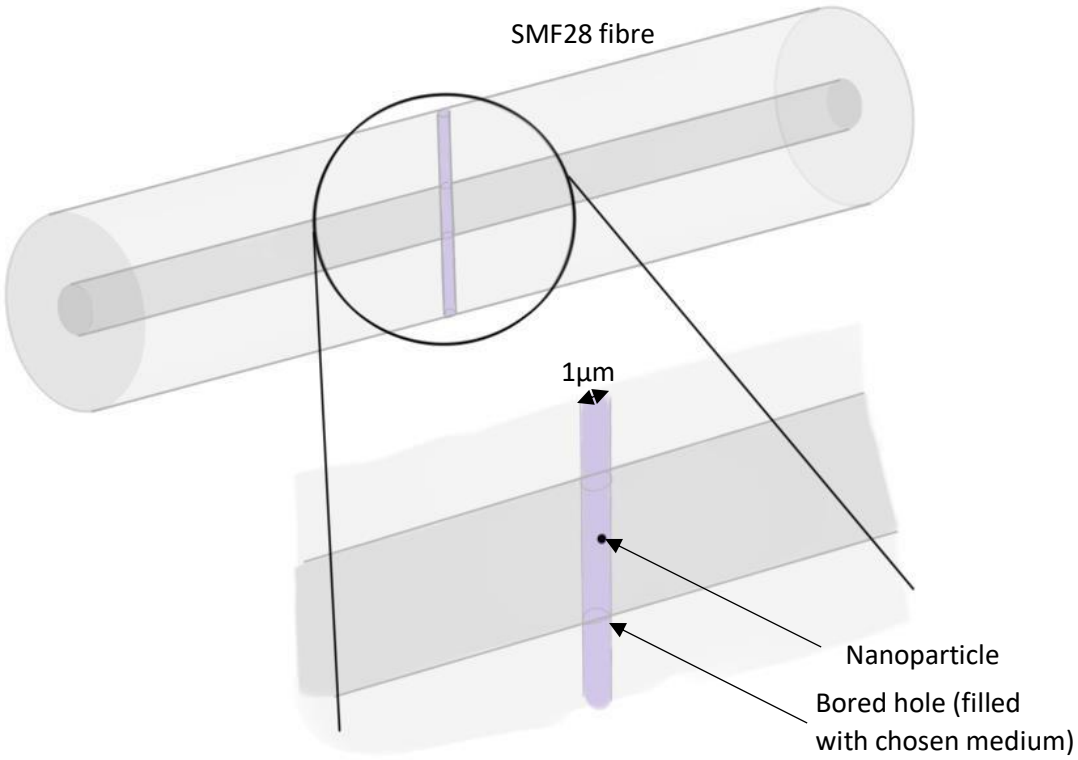

Fig. 3.12: A fibre grating with a microchannel bored through the cladding and core, mirroring the nanoparticle detection system to be simulated. A chosen grating design is inscribed into the fibre core, which is not displayed in this figure in order to aid clarity regarding the bored hole.

The presence of a bored hole between the two FBGs, required to pass nanoparticles through, results in a phase shift in the spectrum passing through, of the form [12, 76]:

$$\frac{\varphi_i}{2} = \frac{2\pi n_{eff}}{\lambda} \Delta z_0 \qquad (3.6)$$

Where the effective refractive index of the gap medium is n_{eff}, λ is the wavelength being inspected and Δz_0 is the length of the gap. φ_i is the phase shift resulting from the presence of such an object. Such a phase shift may be included into a simulation of a fibre Bragg grating that uses the transfer matrix method (described above in section 2.3.2). In order to add the effects of this shift, an additional section must be added to the matrix method in the relevant location of the form [12]:

$$F_{p\,i} = \begin{bmatrix} e^{\frac{-i\varphi_i}{2}} & 0 \\ 0 & e^{\frac{i\varphi_i}{2}} \end{bmatrix} \qquad (3.7)$$

Where $\varphi_i/2$ is as provided in equation (3.6). The result of this shift within the simulation is of the same form as that of a Moiré grating, with the central peak of the spectrum split by the presence of a valley in a location specific to the magnitude of the phase shift. As such, the valley's location will not necessarily be of a symmetric form, though it is possible to achieve this with a particular effective phase shift.

Similarly to the phase shift caused by a bored hole in the fibre, the presence of a nanoparticle also provides an alteration to the effective refractive index. Modelled in a similar method, the nanoparticle forms a significantly smaller size to the area with the altered refractive index, thereby providing a relatively smaller phase shift than the bored hole, in the order of 100 times. The effect of this is a slight alteration to the phase shift of the bored hole without a nanoparticle, shifting the location of the valley by a set amount dependant on the refractive index and size of the particle, as in equation (3.6).

Based on this logic, an alteration in the wavelength of the valley indicates a change within the medium filling the bored hole. If the medium is known to be wholly uniform besides one or more nanoparticles, then such a shift is indicative of a nanoparticle passing into a location where it causes a slight phase shift in part of the spectrum. Given knowledge of this wavelength shift, the phase shift may be calculated and from this, details of the nanoparticle may be gained.

At present these details require some knowledge of the nanoparticle, though as more variations in the spectrum are observed, more information can be gained about the nanoparticle. This will potentially allow for simultaneous measurement of the particles size and effective refractive index in addition to just the presence of one or more nanoparticles. Should the nanoparticle be non-spherical, and its location known, it may be possible to observe the orientation of a particle based on the phase shift and by extension details on what holds the nanoparticle to that orientation, such as an electromagnetic field.

3.7.2. Methods employed within simulations

The simulations employed make use of established MATLAB codes for modelling fibre gratings in single mode fibre. By taking steps, described in greater detail in section 3.7.3, to ascertain how certain aspects of the spectra behave under chosen circumstances, it was confirmed that aspects of the model created followed the theoretical concepts described above. Having confirmed a number of these, the MATLAB model overviewed in section 3.7.2.1 was formed. Limitations to the model do exist and are discussed below in addition to attempts to counter these restrictions and inaccuracies.

3.7.2.1. Basic MATLAB model

The MATLAB model employed is based on the simulation program created for fibre Bragg gratings, based on the Transfer Matrix method described in section 2.3.2. The transfer matrix method employed is adapted to include a phase shift in the central region which aligns to the bored hole and the medium that is contained within. This method uses information gained by the previous split grating simulations, as this model begins as effectively a version of that system with a much-reduced gap length, to simulate the transmission and reflection spectra, gaining a data set for the base system with no nanoparticles present.

The phase shift involved in the appropriate location in the transfer matrix method is that described in equation (3.6), requiring a small addition to the original MATLAB function for the case of the gap's location.

A full description and discussion of the spectral form is discussed in sections 3.7.3 and 3.7.4, though the primary detail considered within this model is the single valley formed within what would be the central peak of the grating. This valley's location is dependent on the phase shift produced, which itself varied depending on the presence and properties of a nanoparticle contained within and shifts

cyclically as this phase changes. This shift in the valley's location may be measured, enabling the phase shift change to be determined.

Following the creation of a spectrum for the base system, the process is repeated with the addition of a nanoparticle of chosen proportions and refractive index. In the case of this work, the tested nanoparticle sizes range from 148 nm, the size of a HIV virion reported by Pang et al [81], to 10nm, an investigation into the potential for measuring small nanoparticles. The system's spectrum with the nanoparticle's presence is calculated and plotted alongside the base system's spectrum for comparison.

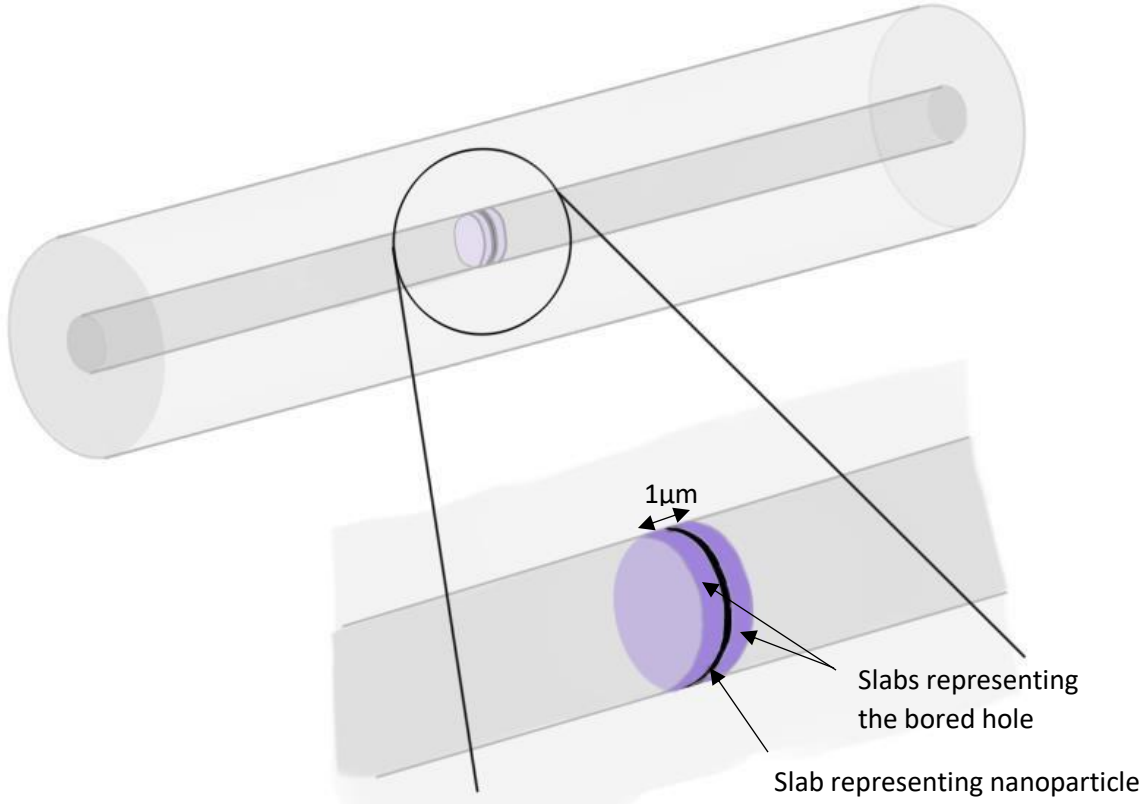

Fig. 3.13: A visualisation of the MATLAB simulation, displaying the limitations of modelling such a system with purely the Transfer Matrix Method. Again, the fibre grating surrounding the system is not represented in this figure to aid in clarity regarding the slabs.

Limitations for this method of calculation do exist in the form of the dimensions of the bored hole and the nanoparticle itself. The main aspect being the model's assumption that all variations are along the fibre's length (z axis) and radially, with radial symmetry being maintained. This limits the modelling of the bored hole to that of a slab of a chosen refractive index and thickness in the z axis, with a visualisation of this provided in Fig. 3.13. Similarly, the nanoparticle is only able to be modelled as a slab of nanometre-scaled thickness. This reduces the physical accuracy of the system and likely increase the magnitude of the valley shifts simulated, though the principal of the valley's shifts remains and proportionate changes in shift should be comparable to a physical system. Methods to counter this limitation are tested in section 3.7.2.2.

Observations of variations in the gap such as the gap medium and the proportions of the gap are discussed in detail in section 3.7.3, as are the effects of a nanoparticle's presence within the gap.

Data sets for both the base system and with the presence of a nanoparticle are saved separately for analysis, in the same format as the original MATLAB function. As such, all sets of data produced by this version of the function and the original function should be compatible with previously written functions for analysing the output files as well as those written for this report.

In addition to alterations to the original MATLAB function, a small number of other functions were created to perform varying comparisons of the outputted data, with a number being based on the same general layout. The main form of these functions involves reading a number of the output files and employing the peak finding algorithm described below to precisely locate the valley's location for each data set. These are compared to each other and for a data set with no nanoparticle present to determine the shift in the valley's location. These shifts are plotted for comparison, enabling a trend in valley shifts to be determined for specified variable changes. Variations of this process have been created for alterations in the medium contained by the bored hole (specifically the refractive index, though other aspects may be observable with adaptations to the main simulation), the refractive index of the nanoparticle and the nanoparticle's size

3.7.2.2. Investigations using other software

As part of the research into simulating the spectra resulting from the grating system described above, the limitations of the MATLAB model were taken into consideration. Potentially the most impactful of these is how the simulation assumes the fibre's structure to be delineated. As the model is an extension of the existing simulation program used within AIPT, it is held to the limitations of a program designed for gratings written in a traditional fibre structure, consisting of a single mode fibre of constant radial proportions along its length. For simulating the majority of the grating structure, this is a perfectly reasonable aspect to work with, however issues arise when the single bored hole is applied to the model.

As any changes in the fibre structure using the existing program can solely vary in the z plane, the same as the fibre's length, the inclusion of a hole of a radius smaller than that of the fibre becomes an issue. The closest approximation to such a hole is that of a slab of material of the same refractive index as the medium filling the hole, set to a thickness matching that of the hole. Such a model effectively simulates light traveling along the centre of the fibre core, passing directly through the hole without scattering due to any curvature. Similarly, any nanoparticle is limited to modelling as a slab with a thickness in the nanometre scale. This renders modelling shifts in the nanoparticle's position along the x and y planes impossible.

To model the system through a more physically accurate method, investigations were made into two other pieces of software, FIMMWAVE and COMSOL, which could consider such a structure. In both cases, the model was formed in two dimensions to become familiar with and test the software's capabilities before progressing to a three-dimensional model. Should this be found to be possible, it would save the need to create a new MATLAB program from the ground up for accurately modelling the bored hole within the grating structure.

<u>FIMMWAVE</u>

Initially, several tests were undertaken using a trial of FIMMWAVE and its FIMMPROP extension from Photon Design. This added some understanding to the functioning of the system as well as some intriguing results, though over the course of the trial questions were raised about the calculation techniques employed by the program and the stability of the program left much to be

desired. As such, its use was not deemed to be viable. Observations are described below that display what was simulated and why this software was not progressed with.

A replication of general SMF28 fibre (using the Corning specifications [82]) was formed with a length of 10μm, displaying a full transmission through the fibre core for a wavelength of 1550nm. This result was repeated for two of these fibre sections connected, as shown in Appendix 1a, confirming that the program did not provide any losses across such a connection.

A simulation of the system using a slab was performed to test the similarities of the calculations and their results to the established MATLAB program. Should these results be similar to those described in sections 3.7.3 and 3.7.4 then progression could be made with the knowledge that further results would be comparable to a MATLAB program accounting for aspects explored in FIMMWAVE.

The addition of a 1μm slab of refractive index 1.61, displayed in Appendix 1b dramatically reduced the transmission through the system to a mere 23.6%, which would be expected for a grating designed for a wavelength matching the 1550nm simulated here. However, for a single gap, this reduction in transmission is not anticipated. Similar results were gained when varying the refractive index of the gap medium, with no result gaining more than 26.1% transmission. To observe this, a parameter scan was performed, as in Appendix 2, varying the refractive index of the gap and observing the transmission across the system.

Following this initial test, a replication of an FBG in a two-dimensional system was performed. FIMMWAVE's method of repeating a specified period, as shown in Appendix 3a, enables a relatively efficient way to repeat calculations for each period a specified number of times. For simple grating designs, this provides a good simulation of the transmission and reflection profiles when scanning over a range of wavelengths, however investigations into more complex FBG designs, groups of FBGs (as required for the nanoparticle detector) and for LPGs varied significantly from the results of the established MATLAB programs. An example of a pair of FBGs is displayed in Appendix 3c.

In order to more accurately represent the bored hole through the fibre, an alternative method for modelling the area around the hole was investigated. The use of a mixed waveguide method to model the fibre in the hole's vicinity was used instead of the inbuilt fibre waveguide model used above. The method for simulating SMF28 fibre using a mixed waveguide differs from that of a fibre waveguide in that the waveguide is measured via Cartesian coordinates in place of a radial system. This enables the area in which the nanoparticles are occurring to be modelled as a hole bored into the fibre instead of a gap between fibre sections. Initially, squared off versions of the fibre cladding were simulated for simplicity of programming, though this was later altered to a circular form.

In this system, a nanoparticle can be simulated as a rectangular form of height and width of 0.001μm and a length of 0.01μm (determined by the length of the section modelled with the nanoparticle, with regular gap sections placed either side). Again, the nanoparticle can be shifted in the z axis by manipulating the lengths of the regular gap sections on either side, as with the MATLAB simulation, as well as being shifted in the x and y axes. Similarly to the fibre waveguide example, the nanoparticle can be "rotated" by changing which axis has a longer length of 0.01μm. In the mixed waveguide case however, this incurred no change in transmission.

After time being spent on the reoccurring problem with reliable and realistic simulations of FBGs, as well as a software stability issue that interrupted progress on multiple occasions, it was concluded following the trial that it would not be viable to progress using this software. Despite these setbacks, useful knowledge was gained on how aspects of the nanoparticle detection system could be

modelled, which aided in simulations using COMSOL and enabled more to be performed when examining both COMSOL and MATLAB.

COMSOL

Following the tests with FIMMWAVE, a software trial of COMSOL and its Wave Optics module was acquired. This showed promise in modelling the section around the bored hole, though COMSOL's method for calculating the physics of electromagnetic waves seems to not be suited for modelling over the length of such an elongated structure. Issues with runtime render the simulation of the entire nanoparticle detection system unfeasible, though COMSOL may be of worthwhile use for simulating the area around the bored hole in nanoparticle detection tests.

Initial tests followed the same lines as the above FIMMWAVE model, forming a short length of basic smf28 fibre (again, matching the Corning specifications), in this case 100µm in length. This was performed to test the capabilities of COMSOL, prior to a full grating model, regarding the simulation of long, thin structures in line with optical fibres both with and without a microchannel as well as identifying how the simulation package handles such a task. Initial simulations (shown in Appendix 4a) observed an issue that would become a theme among the COMSOL models; that of an extended runtime. For this 100µm length of smf28, the program took over eight minutes to run, in comparison to the MATLAB model's runtime in the order of a few seconds for an entire grating.

As the transmitted modes in this model should be confined to the fibre core, the cladding's radius was reduced to 20µm, enough to confirm the location of transmission whilst cutting the runtime. As a result of this reduction, and the subsequent lowering of the number of mesh nodes COMSOL performed calculations over, the runtime was reduced to the region of half to one minute for a single wavelength scan, in a simulation displayed in Appendix 4b. Whilst this is a significant reduction, it is still not enough to make a parametric sweep over a large number of spectral wavelengths viable, with a sweep of 30 wavelengths between 1548nm and 1552nm requiring seventeen minutes to perform and 20 wavelengths requiring a little over eleven minutes. Increasing the mesh element sizes also reduced the runtime, though at the cost of significant precision in the results generated.

As these runtimes do not permit a reasonable simulation of an entire grating, tests were performed to generate a simulated single period of a grating for potential use should the runtime issue be resolved. To perform this, the latter 50µm of the structure was adjusted so that the fibre core's refractive index was 1.4732 (an increase of 0.005). This produced the result in Fig. 3.14Fig. 3.14 , displaying the simulated effect of this refractive index change on the transmitted and reflected spectra from a 100% transmission in the previous model. The alteration of the transmission and reflection spectra for this single, short period confirms that COMSOL's model for calculating shows promise for simulating grating structures, though the extended runtime and memory usage for longer lengths makes the use of it for observing the transmittance and reflectance of a grating unviable at present. Limitations in the model due to unfamiliarity with COMSOL may be present, which alongside techniques discovered over the remaining trial period, may counter the issues described in this section to an extent, though this was judged to be insufficent to progress with these simulations using COMSOL.

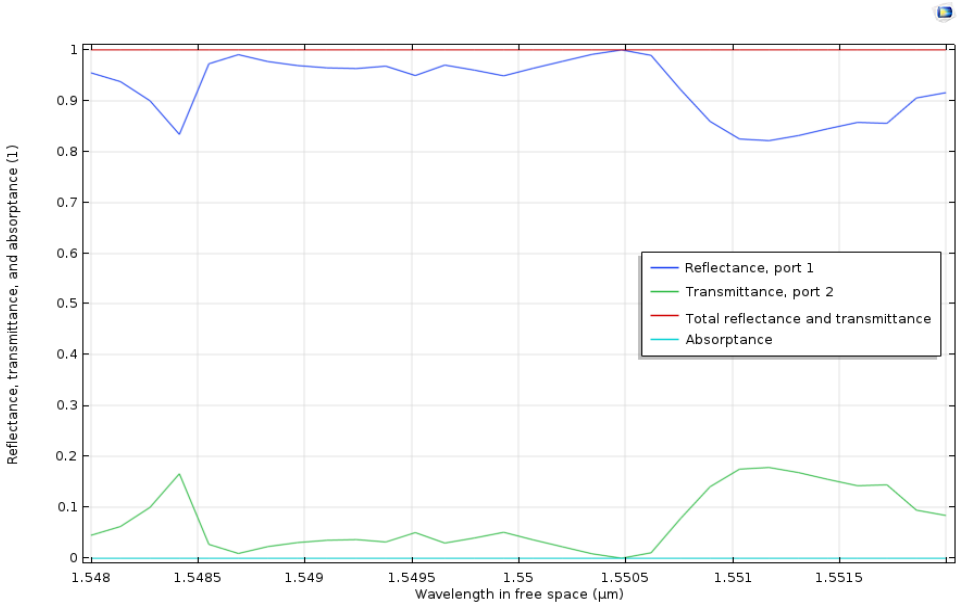

Fig. 3.14: The calculated transmission and reflection spectra across 30 wavelengths for a 100μm smf28 fibre length where the latter 50μm has a core refractive index increase of 0.005. To total of the reflectance and transmittance in this figure shows a lossless system for this simulation test of a short perturbed fibre section.

Following this conclusion, the remaining trial period of COMSOL was spent investigating other ways it could be of use. Focussing on the immediate vicinity of the bored hole, the use of COMSOL for analysing the modes was inspected.

Working with a three dimentional model of a 10μm long smf28 section, the modes at either end of the model were observed, as shown in Fig. 3.155a. In this figure, the visual of the z axis has been stretched to more clearly display the modes at each end simultaneously, distorting the appearance of the cylindrical microchannel in Fig. 3.205b in particular.

By modelling the modes at each end of the fibre section, the transmission of each mode can be observed, with attention paid to the strength and any distortion of the mode's shape. Noting the drop in transmission at particular wavelengths (mainly tested in the vicinity of 1550nm) when a microchannel is added to the system, an effective ground state for a nanoparticle detector can be modelled, in preparation for a version where a nanoparticle is introduced.

The modelling of the modes resulted in the same mode form and strength at each end for a wavelength of 1550nm, indicating a 100% transmission rate across the sample, similarly to the smf28 transmission observed in the previous tests above. The addition of a 1μm diameter cylindrical hole filled with methanol (refractive index = 1.33), as displayed in Fig. 3.15b, subsequently created a drop in transmission whilst keeping the form of the mode virtually constant. The 47% drop in transmission however is significant as it is much higher than expected for a hole covering roughly 12% of the core's radius in the y plane. If the surrounding gratings system was included in this simulation, then this drop could be accounted to the transmission spectrum of the gratings, though this is not the case with the simulation.

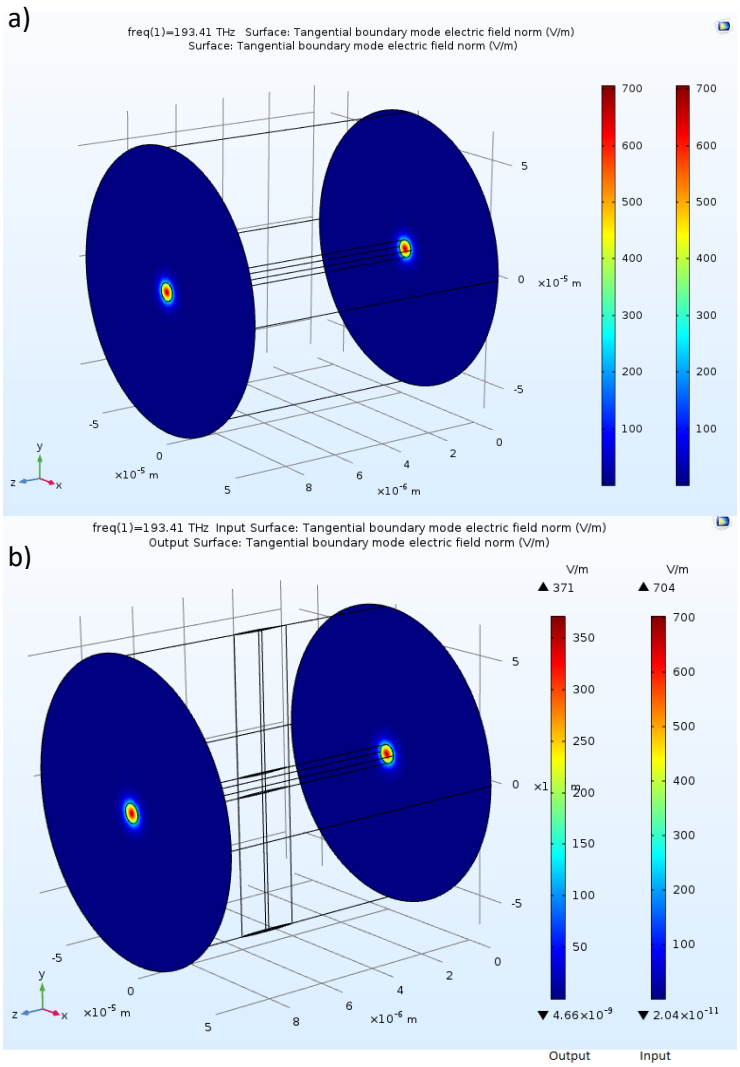

Fig. 3.15: A comparison of the input and output modes for a 10µm length of a) smf28 fibre, b) smf28 fibre with a 1µm methanol hole bored though the core. Fibre diameters and refractive indices matching the SMF28 parameters were applied. In this diagram, light is input from the +z direction (left) and the output transmission through to the –z end (right) is compared on the scales beside the diagram.

The capabilities of COMSOL for presenting the above system with a nanoparticle within the microchannel was briefly explored prior to the end of the trial period, with the principals of how such an addition could be made being uncovered. The generation of either a spherical or near-spherical object in addition to a cylindrical (or similarly extruded) form is possible as is control over the location in the x, y and z planes. Based on this and the possibility to present the simulation with multiple nanoparticles, COMSOL shows promise for modelling this aspect of the nanoparticle detector. More work on progressing the microchanel simulation in Fig. 3.20 prior to full tests with a nanoparticle would be of benefit, especially with respect to observing the effects at different wavelength values and with the aim of a decrease in runtime.

The use of COMSOL for simulating the nanoparticle detection system as a whole does not seem to be feasible, considering the elongated runtimes in comparison to MATLAB for general fibre gratings. Should a method for altering the mesh to enable this difference in runtime be successfully implemented, then it would be worthwhile to perform simulations with COMSOL, as the methods employed enable a more physically accurate representation of the bored hole than the MATLAB model could achieve.

Considering these limitations, a possible mid-point could be employed should careful data management and automation be employed. A mixture of MATLAB and COMSOL for simulations of the fibre gratings and the bored hole section respectively could enable the best of both programs, with data from the first set of gratings passed to COMSOL for the bored hole section, then passed back to MATLAB. This would pose the issue of how to transfer not only the propagation data, but also any relevant variables used within the simulations and ensuring COMSOL's calculations mirror that of MATLAB's in such a way as to produce comparable results. A successful implementation of this data transference would allow the need for COMSOL's elongated process of processing fibre gratings to be bypassed in favour of an established and more efficient MATLAB program, whilst areas that the MATLAB program struggles with would be calculated within COMSOL for a more physically accurate representation of the system. This limiting of COMSOL's use to the aspects that the MATLAB program struggles to simulate however may not be worth the cost of the software unless other uses are also required.

3.7.2.3. Peak finding algorithm

In order to ensure the comparison in valley location shifts made use of a standard position, a specific function was written to provide an accurate description of the peak's location. The precise nature of the valley shifts in the presence of a nanoparticle requires the location of the valley's peak to as high a precision as can be gained. For such a reason, an alternative function for identifying the peak was created via the established centroid method.

This function was based on the existing MATLAB function "findpeaks", which locates the location of a plot's peak though will select a point on one side of the peak should it plateau rather than the central location. The written code initially performs the same task as findpeaks, though will choose a central point in the case of a plateau.

The maxima point is used to locate the peak to within sub-point accuracy on the x axis via the centroid method. Using the initial method's maximum as a starting point, the form's full width at half maximum is employed as boundary locations for the centroid method. This uses equation (3.8) to effectively find the centre of mass for the area between the boundaries, with the area used for this highlighted in Fig. 3.16. This produces an offset from the initial maximum which is applied and subsequently used as the peak's maximum.

$$x_{com} = \frac{\sum x_i L_i}{\sum x_i} \qquad (3.8)$$

Where x_{com}= the value on the x axis for the centre of mass, x_i= the i^{th} value on the x axis and L_i= the i^{th} value on the y axis. The summations are of the i values between the two boundary points. In this case, this is between the two full width at half maxima points.

Given a high resolution, the change induced by the centroid method is often particularly small, though it becomes of great use in situations such as that displayed in Fig. 3.17. Where the number of data points results in a plateau at the peak, MATLAB's findpeaks function will select a data point at one end of the peak (highlighted as a circle in Fig. 3.17).

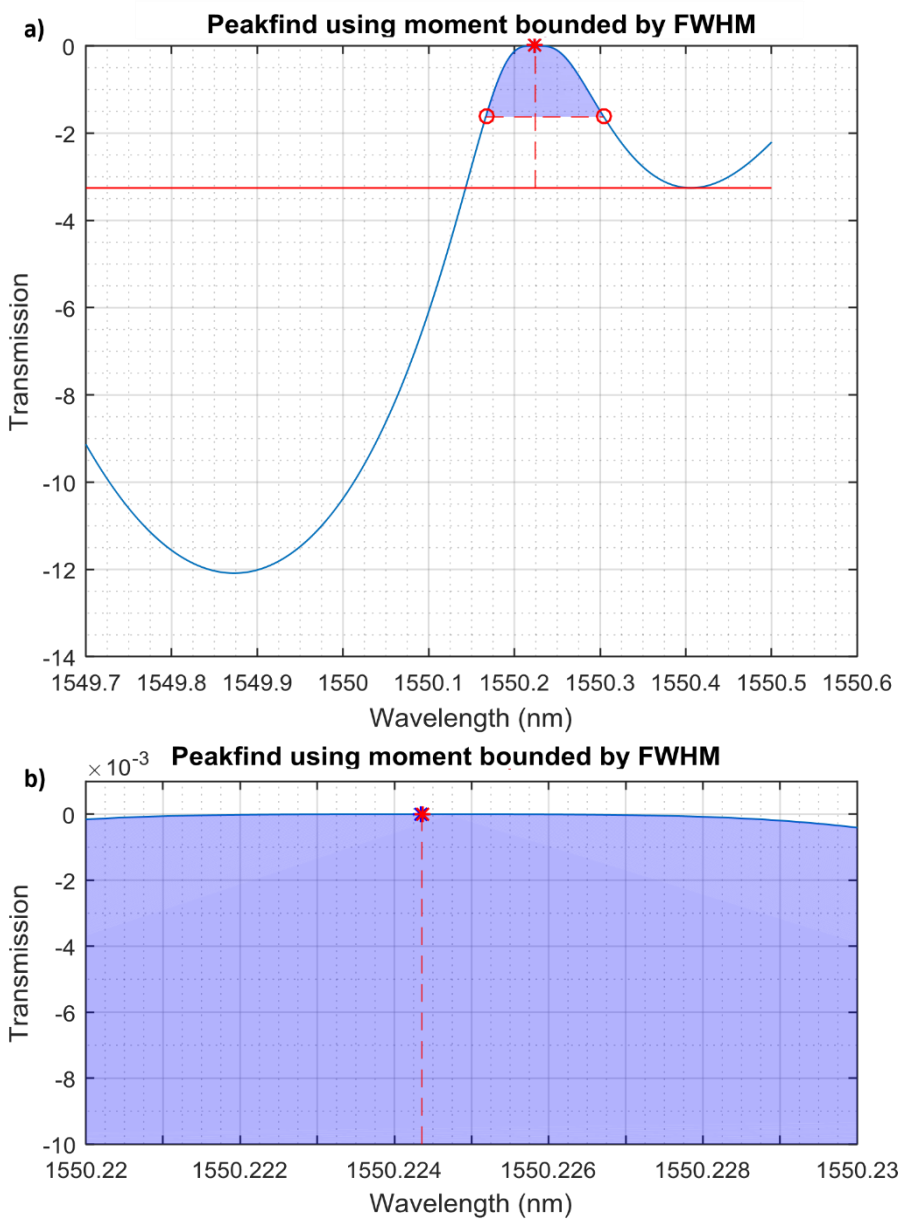

*Fig. 3.16: a) The area employed by the peak detection algorithm's centroid calculations to locate the maximum. The red star is the maximum found by the contained "findpeak" adaptation. The red circles are the boundaries defined by the full width at half maximum of the peak (marked by the red line). The blue shaded area delineates the area employed by the method to determine the maximum at sub-peak accuracy. b) An enhanced view of the maximum, showing the offset between the initial maximum (blue star) and the adjusted maximum (red star). In this case, the shift is 4.4043*10^{-5}nm.*

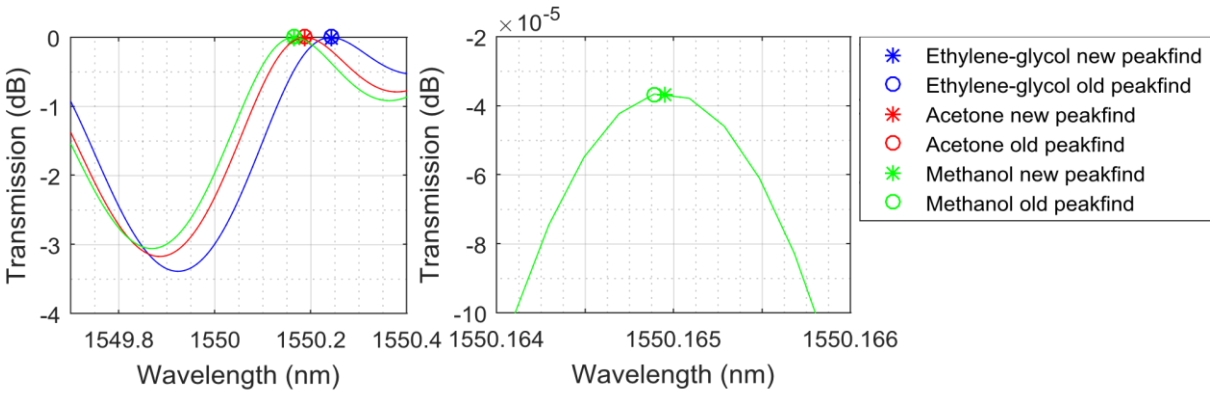

Fig. 3.17: An example of the located peaks using MATLAB's basic findpeaks function (circled) and the adapted moment-peakfind function (starred). Each data set used in this plot is comprised of 20000 points, with roughly 3500 data points in the section the function analyses (in this case, the wavelength range 1549.7-1550.4nm).

Though it is a simple change to the findpeaks function, this variation enables the peak to be located much more precisely than the base MATLAB findpeaks function, in particular granting the possibility of sub-point accuracy. In the case of measurements via a LUNA OVA, the resolution of the data may result in peaks located between data points or plateaus forming based on where data points are located. The use of such a peak-finding algorithm will enable the location of the peaks to be more thoroughly defined without total reliance on convenient point location and the variations thereof. As such, it can be clearly stated that for the purposes of locating peaks, this function is of far greater use than the base MATLAB findpeaks function.

3.7.2.4. Simulation assumptions

As may be noted in the above simulations, the assumption has been made that a single nanoparticle is present in the system, which is unlikely to be the case in the majority of physical measurements. This assumption was made for the model within this thesis in order to better understand how a single nanoparticle changes the spectrum and to understand the processes involved in the simulation. By using the simulation results, one can begin to form a system for monitoring a small number of nanoparticles which may be more easily tested.

In the situation where multiple identical nanoparticles are present in a medium, an experiment employing the logic behind Millikan's oil drop method could be made use of. By observing the magnitudes of shifts and noting that this will always be an integer multiple of a single nanoparticle's shift, the total shift induced can be calculated via a number of measurements over a space of time. Once this has been performed, a determination of the number of particles or aspects of the nanoparticles can be made as with the presence of a single particle.

Should a measurement contain nanoparticles of varying sizes, such as the presence of viruses among blood cells, then a knowledge of the shift sizes can be used to determine the concentration of each form of particle. Such a method assumes a system closed to external nanoparticles entering and would require tests to gain information on the shift size for the included particles, likely via the method described for detecting identical particles. Once such data has been acquired, a number of scans, of a greater number than for identical nanoparticles, can be made and the shifts observed. As before, integer multiplications of the shifts induced by a nanoparticle form the overall shift, though this time with multiple values for the shifts comprising the spectral change. This increase in parameters makes the measurement more complex and hence, more measurements will be required to truly observe the composition of the analysed set of particles.

Other assumptions made include the spherical nature of nanoparticles simulated. Whilst items such as virions are often close enough to spherical to be modelled as such, the simulation of non-spherical nanoparticles has not been included in these simulations. This assumption is made to allow for a consistent parameter among the above simulations, though with the inclusion of an appropriate COMSOL model for the microchannel region, a non-spherical nanoparticle is easily simulated. Additionally, the assumption that the particle is located centrally in the x-y plane is due to the present model limitation in the MATLAB simulations. Once again, a functioning COMSOL simulation will enable the removal of the assumption.

3.7.3. Effects of gap alterations and nanoparticle presence

Gap alterations

As can be seen from equation (3.6), a change in the phase during a step in the transfer matrix method will result in an alteration to the form of the spectrum. Given that the phase is itself dependant on the refractive index and the length of the section covered by the step, it is expected that variations in the medium contained in the bored hole will be observable in the spectrum. In addition, the spectrum should be sensitive to changes in the diameter of the hole, though this should remain consistent once the structure is formed. Should care be taken with tests on a physical structure, changes in this aspect for the hole itself should be kept to a minimum, enabling phase shifts to be solely dependent on the medium contain within the hole.

Within the model, this is easily achieved, enabling an observation based solely on a single varying aspect. Initially, simulations were run to observe how a change in each variable affected the spectrum, noting the expected cyclical pattern to the shift in the valley. As an initial centre point for early tests, the minimum width of the bored hole for a $\pi/2$ phase shift when the hole is filled with air was investigated, with a slab of 387nm thickness achieving this. This was chosen as a $\pi/2$ phase shift creates a single valley in the centre of what would be the central peak. From this point, any shifts are easily observed as it would break symmetry in the x axis around the grating system's design wavelength.

With the slab thickness held constant, three other gap mediums were simulated; acetone (RI=1.36), ethylene-glycol (RI=1.447) and methanol (RI=1.33). As can be seen in Fig. 3.18, the varying refractive indexes of the media results in an index-dependant shift, with larger refractive indexes inducing a larger shift. The shifts themselves are sub-nanometre in scale, requiring specialised equipment to observe in a physical system. In the case of Fig. 3.18 these shifts, with relation to the air spectrum, are; ethylene glycol: 0.1675nm, acetone: 0.1378nm and methanol: 0.1273nm.

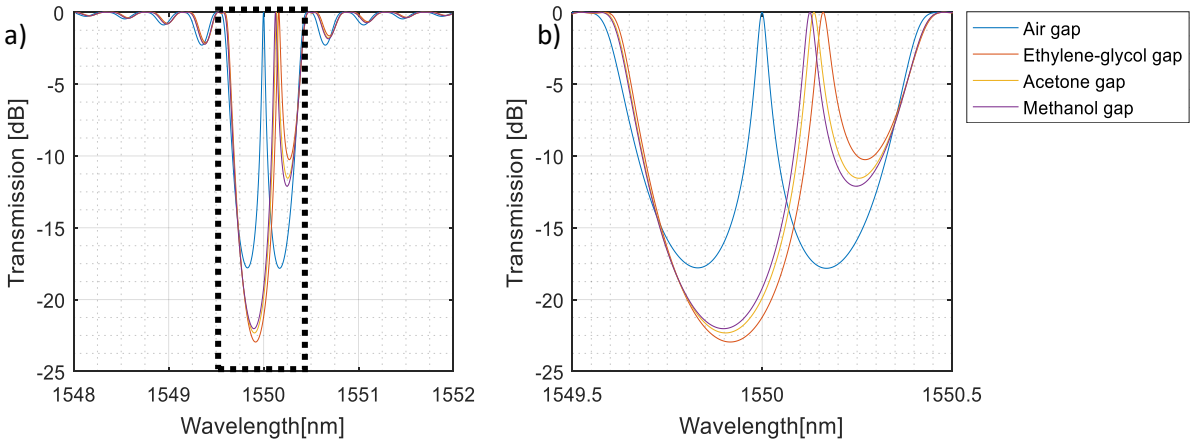

Fig. 3.18: The transmission of a 1550nm grating pair separated by a gap of 387nm comprised of air (blue), ethylene-glycol (red), acetone (yellow) and methanol (purple). b) is an enhanced view of a) focussing on the area around the central form of the spectra.

Similarly, changes in the slab's length within the simulations affects the location of the valley. Small increases in the length shifts the valley to a higher wavelength. For example, altering the slab length to 500nm with air as the medium, increases the valley's wavelength by 0.1137nm. Doubling the slab length from the 0.387nm example above will lead to a π shift, masking any existing valley. A small shift from this point is more difficult to observe in comparison to a central valley due to the relative magnitudes of what would be the central peak of a uniform grating at the respective wavelengths.

Due to the cyclical nature of the valley's shift, should a refractive index cause a shift for a given slab length to move to valley outside of the "central peak's" area, the valley will instead be observed to enter the other side of the peak. Thus, care is required should the slab length create a valley far from the peak's centre. Ideally, the base system should have a phase shift of some odd multiple of π/2, to minimise the chance of this occurring and allowing any shift to be easily measured independent of the shift direction.

In the case of a nanoparticle detection system, it should be considered that the spectrum of the base system varies depending on the medium, ideally keeping the choice of medium constant once the design has been chosen. As the detection of a nanoparticle is based on variations in the valley location relative to that of the base system, the base valley location of the detector should be precisely known for every measurement with a nanoparticle. As the shifts due to nanoparticle presence, as described below, are much smaller than for the medium changes covered above, precise intruments will be required for a physical system.

Nanoparticle presence

The addition of a nanoparticle to the system follows much of the same logic as described above for the base system. Again, limitations exist in the MATLAB function regarding the simulation of an object in the fibre that does not match the fibre radially. Hence the nanoparticle is required to be considered as a slab of a nanometre scaled thickness. This thin slab is placed within the slab representing the bored hole, effectively rendering it as a pair of slabs either side of the nanoparticle, with a total length adding up to the desired value for the base system's hole.

By varying the lengths of the gap either side and keeping the total length constant, the nanoparticle can be “moved” to different points across the gap. Initially, the nanoparticle was placed in the centre of the gap, ensuring symmetry from the central point of the “physical” structure of the system. Given the present state of the simulations, shifts of the particle in the x and y planes is not possible, only in the z plane. Given work to modify the simulations to allow for particle motion in the x and y planes, variations in the spectrum could be calculated to observe this change in additional dimensions.

Initial tests modelled the nanoparticle as a 10nm thickness slab with an arbitrary refractive index of 1.4, chosen to be in proximity to a number of crystals and biological materials at 150nm. The hole, as with other simulations further in this section that are not specifically mentioned, was modelled as an acetone slab of 1µm thickness to match an assumed microchannel diameter in a physical setup. A small change in the transmission spectrum was observed by the addition of this nanoparticle. This is most observable as a shift in the location of the valley and a subsequent change in the maximum of the smaller peak beside the valley, as seen in Fig. 3.19. The location of the particle across the gap was also investigated, though no difference in the spectrum was discovered by altering this variable.

With the above simulation, a shift of +0.45pm was formed, with a change in maximum of the smaller peak being 0.012dB. Although this shift is too small to be observed with the maximum resolution of a LUNA optical vector analyser (1.25pm in spectral wavelength), this does show that a shift occurs.

Following from the investigations into altering the length of the slab representing the hole, the size of the nanoparticle was found to influence the location of the central valley, as seen in Fig. 3.20. Particle sizes of 10nm and 20nm were selected to investigate the lower boundary of anticipated nanoparticle sizes, arbitrarily chosen to provide a simple comparison for changes in particle size. This effect was observed to linearly increase with the nanoparticle size. A similar change in the magnitude of the smaller peak was observed, allowing for a comparison in both areas of the spectrum.

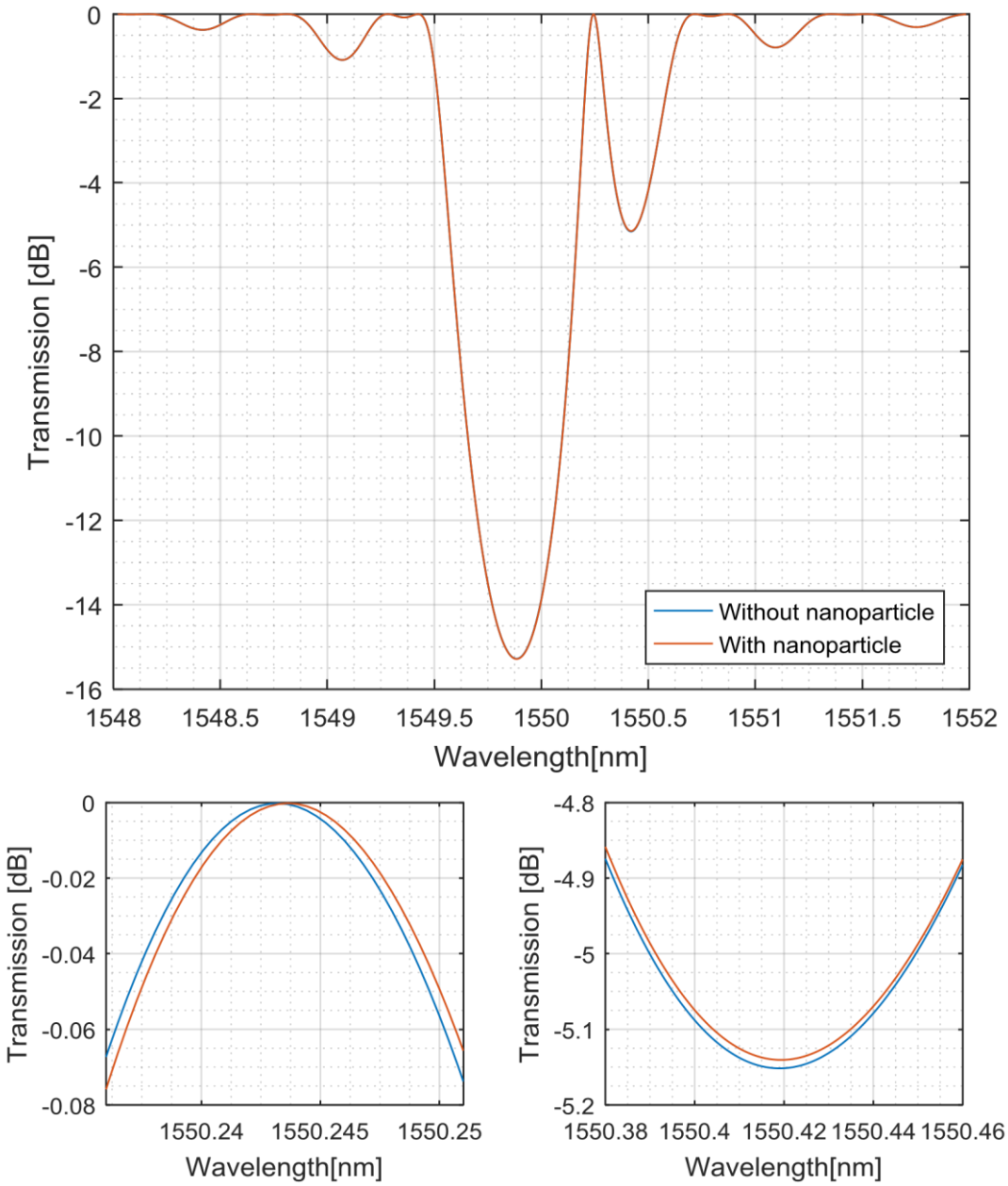

Fig. 3.19: a) A comparison between an acetone 1µm gap without (blue) and with (red) a 10nm nanoparticle of refractive index 1.4. Including a detailed look at; b) the location of the lowest point of the valley, c) the maximum of the smaller peak located by the valley.

As with the dependency on the gap medium's refractive index for a shift in the valley, altering the nanoparticle's refractive index results in a shift. This shift is based on the relative difference between the refractive indexes of the gap medium and nanoparticle, with the valley shifting to higher wavelengths if the nanoparticle has a higher refractive index, as seen in Fig. 3.21. Any particle refractive index below that of the gap medium shifts the valley's location to a lower wavelength whilst a higher refractive index shifts to a higher wavelength.

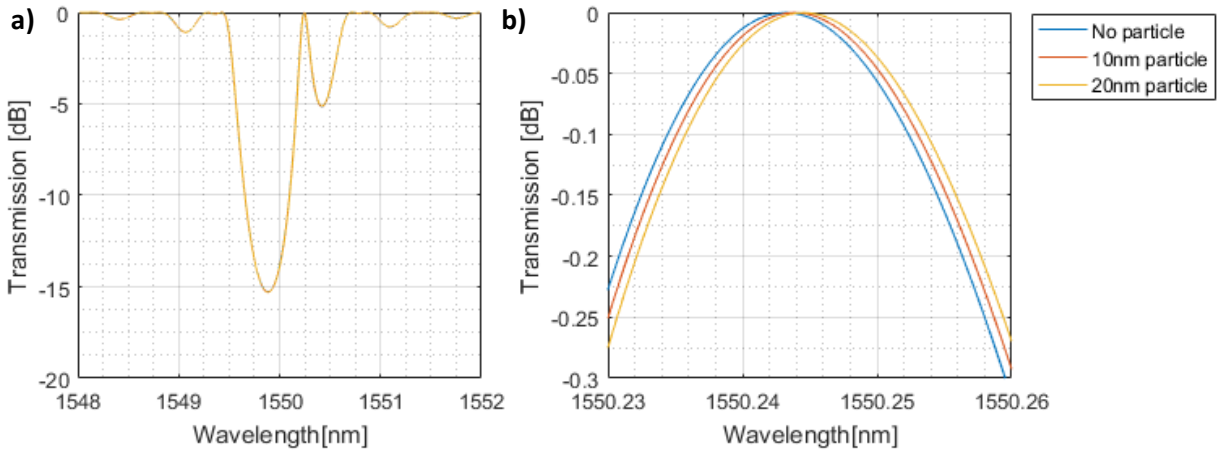

Fig. 3.20: a) Comparison of nanoparticle size in the same system as Fig. 3.19 without a nanoparticle. b) The same data, focussing on the base of the central valley, showing the shift in the valley's wavelength is dependent on the nanoparticle size.

Should a nanoparticle's refractive index exactly match that of the surrounding medium, then the system appears the same as if no nanoparticle was present. This is due to their effectively being no boundary to affect the transmitted light, leading to a spectrum matching that of the base system. This places a physical limit on the nanoparticle detection based on the refractive index of the particle and the medium it is contained within. In such a circumstance, an alteration of the surrounding medium will be required to detect the nanoparticle. Following this logic and the results displayed in Fig. 3.21, a maximised difference in refractive index between the nanoparticle and surrounding medium is highly beneficial as it increases the shift in the valley, increasing the likelihood of its detection in measurements.

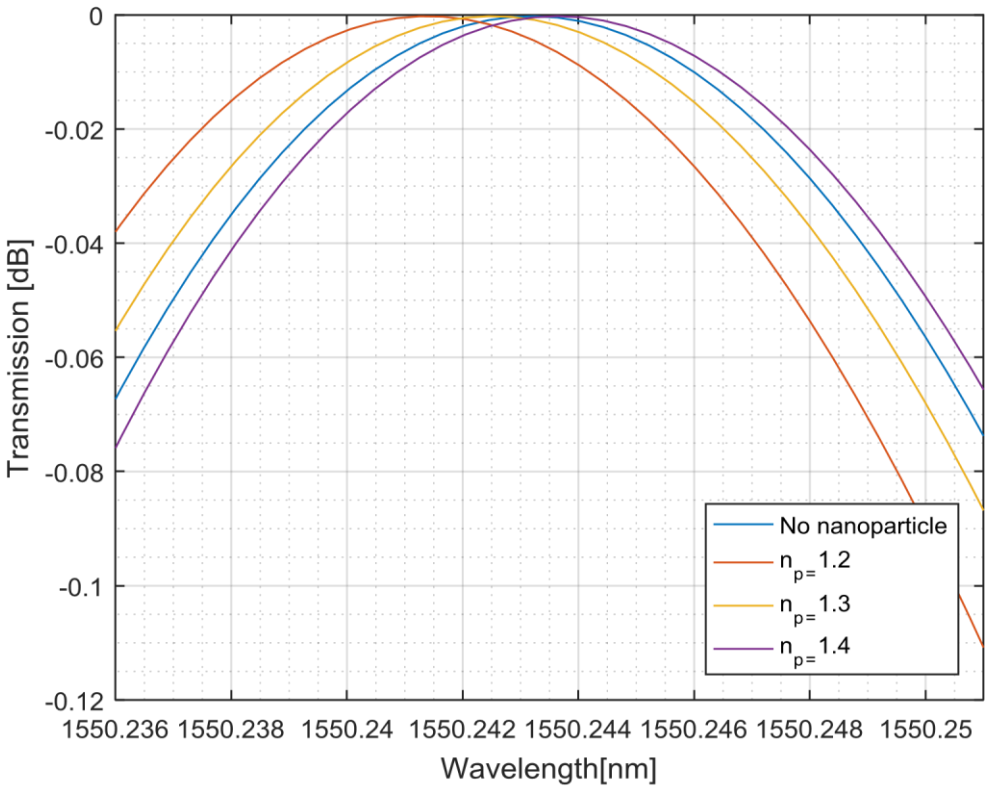

Fig. 3.21: The shift in the base of the central valley dependent on the refractive index of the nanoparticle, highlighting the significance of the difference in refractive index between the nanoparticle and the medium. Nanoparticle refractive indexes of 1.2, 1.3 and 1.4 were chosen to demonstrate the linear changes in shift.

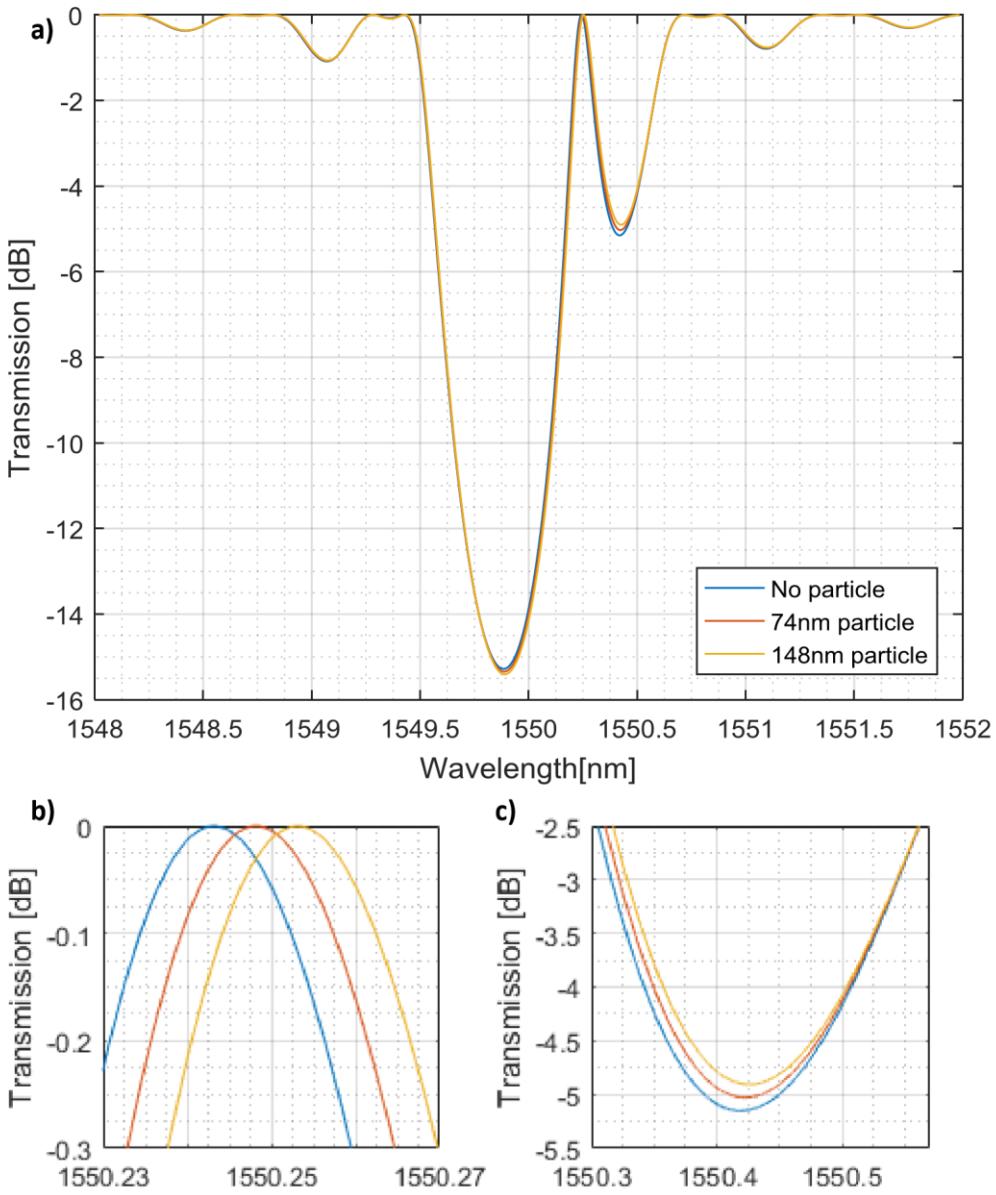

Fig. 3.22: The a) transmission plots for a nanoparticle of 74nm and 148nm length and refractive index of 1.42 compared to the same system with no nanoparticle. Including enlarged plots focussed on, b) the base of the central valley and c) the maximum of the smaller peak located by the valley. The surrounding medium considered for this plot is acetone (RI=1.36).

A detailed analysis of variations in this valley's shifts is present in section 3.7.4, observing the patterns in shift magnitude that have been mentioned within this section.

Continuing this investigation, the parameters of the nanoparticle were adjusted to match that of an example nanoparticle, a HIV virion. Measurements for a HIV virion have been recorded by Pang et al [81], with a particle radius of 74nm and an effective refractive index of 1.42. This is substantially larger than the 10nm nanoparticle tested above, with the size of the nanoparticle having been shown above to affect the magnitude of the valley shift. Given the refractive index's similarity to that of ethylene-glycol, it can be immediately noted that this surrounding medium would be a weaker candidate for measurement purposes, hence the use of acetone (RI=1.36) and methanol (RI=1.33) as a medium surrounding the nanoparticle within these simulations. Methanol has the added advantage in this particular example of having an effective refractive index in close proximity to that of blood [83], in which the HIV virion may be tested within in more physical simulations. Differences

in gap medium between methanol and blood do exist in terms of, for example, transmittance of spectra however, which must be considered in more advance simulations.

In order to observe the valley's shift at this scale of nanoparticle, particle lengths of 74nm and 148nm were tested, demonstrating particles simulated for both the radius and diameter of a HIV virion. These showed substantially larger shifts than for 10nm and 20nm nanoparticles, which may be observable with a LUNA optical vector analyser. Fig. 3.22 shows the transmission spectra for the larger nanoparticles, which is now observable without requiring an enlarged view

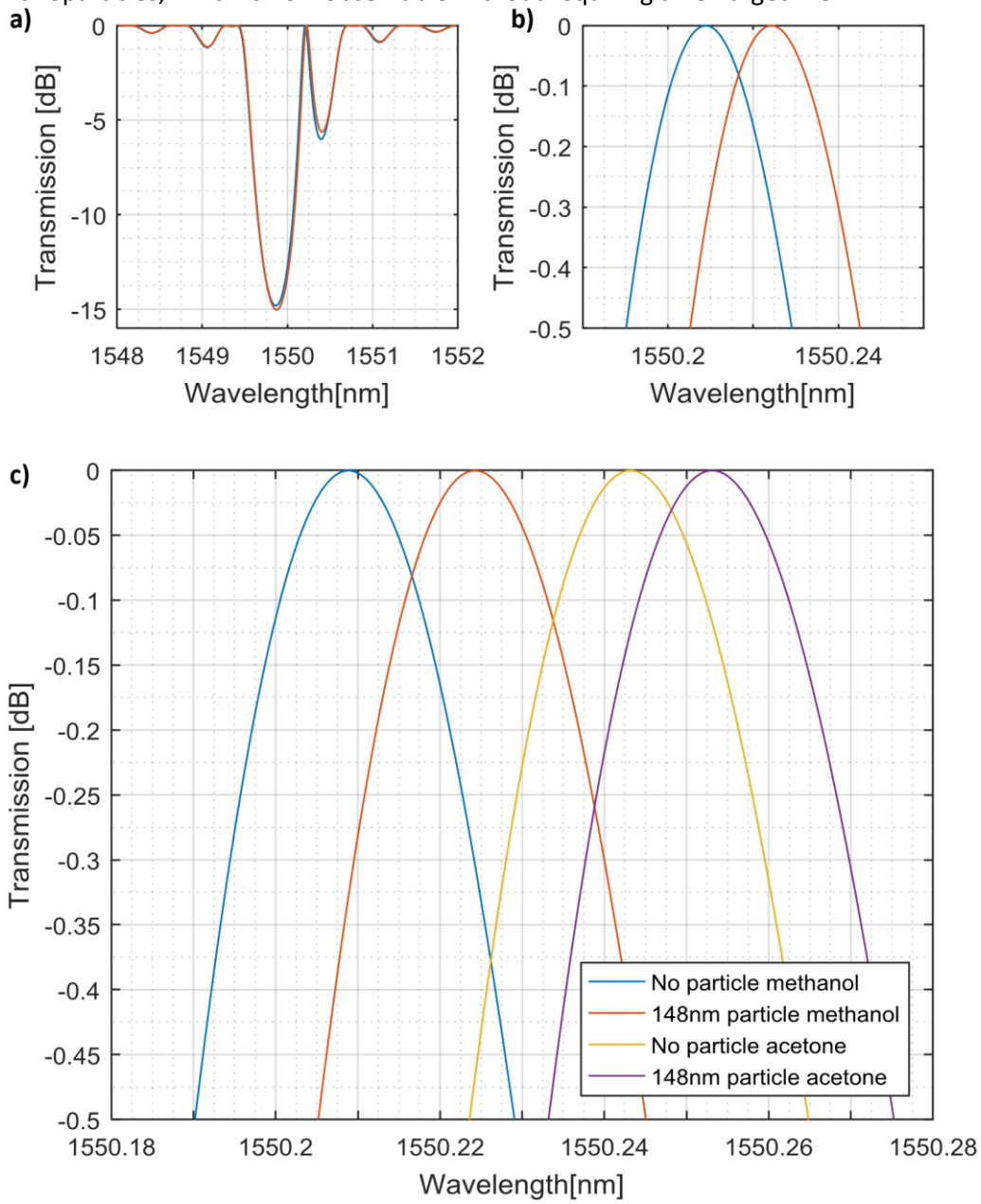

Fig. 3.23: a) The transmission plot for a system with a methanol gap with and without a virion-sized nanoparticle. b) The same plot focussing on the shift of the peak of the valley. c) A comparison of the valley shift for methanol and acetone in comparison to no nanoparticle presence.

At this scale of nanoparticle, the wavelength shift of the central valley has increased to 5pm for a 74nm particle and 9.9pm for a 148nm particle when contained within acetone. The maximum reflectivity of the smaller peak located by the valley has also reduced by 0.0088 and 0.0179 for a 74nm and 148nm particle. This shift size is observable on a LUNA OVA, with the maximum resolution providing four points over the shift for the 74nm particle. Though this resolution does not provide a

very precise representation for the shift, it is sufficient to observe the change and gain an idea of the size of a nanoparticle of known refractive index to around ±10nm. The development of more precise measurements along the spectral wavelength will assist with reducing this error and for the reliable detection of particles below 19nm in size.

In comparison, a shift of 15.4pm is achieved when the gap medium is changed to methanol, keeping other factors constant. This shows that the shift is substantially different when the refractive index of the gap medium is lower than that of the acetone example used in most simulations. Fig. 3.23 shows the shift due to a nanoparticle's presence for a methanol gap and a comparison is drawn between an acetone and methanol gap. This shows that the shift is slightly larger for a methanol gap than one comprised of acetone, making a more noticeable change in the spectrum. This demonstration of this change in shift due to a lower gap medium refractive index shows the sensitivity of changes in this variable for a nanoparticle similar to that of a HIV virion and the importance of knowing the effective refractive index of the gap medium carefully. Therefore, an importance is placed on this variable should the gap medium be of an organic material, such as blood. Using the criteria for a HIV virion, this suggests a minimum particle size of roughly 12nm for detection with a LUNA OVA when using methanol as the gap medium.

3.7.4. Variations in valley shifts

As can be seen in the figures above, the shifts in the valley caused by variations in the system are due to several aspects related to the effective refractive index and distances. In this section, an analysis of these variations is made, with the intention of highlighting the effects of each aspect on the location of the valley within the spectrum.

The variation in the magnitude of the valley shift due to the size of the nanoparticle, as shown by Fig. 3.20 and Fig. 3.22 displays immediately that this factor is of prominence. Similarly, the difference in effective refractive index requires careful consideration.

As can be seen from Fig. 3.24, an enlarged difference in refractive index between the nanoparticle and the gap medium has an increased effect on the magnitude of the valley's wavelength shift, enabling smaller nanoparticles to become observable with the resolution of the LUNA OVA. The 1.25pm threshold for detection with the OVA is only crossed for a nanoparticle in an ethylene-glycol gap for a particle greater than 124nm in size, in the area of seven times that for an acetone gap. Should a medium of a refractive index between acetone and methanol be used, presuming a low absorbance, then a wide range of particle sizes may be observable.

Fig. 3.25 displays the same test performed with gratings of varying reflection strengths. Grating coupling coefficients of 1040 (95.73% maximum reflectivity), 700 (78.66% maximum reflectivity) and 350 (24.67% maximum reflectivity) were used, repeating the same procedure as Fig. 3.24 employed. Each gap medium is represented with the same colour for each relevant data set.

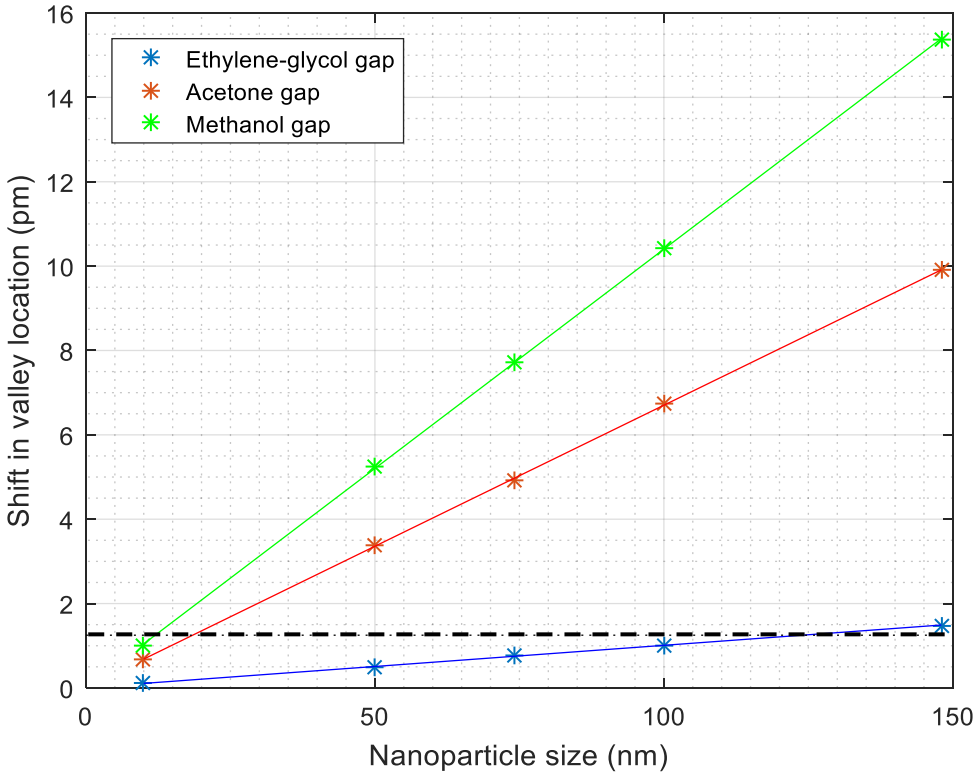

Fig. 3.24: A comparison of the magnitude of wavelength shifts for the lowest point of the valley for systems with a gap medium of ethylene-glycol, acetone and methanol. A shift of 1.25pm is observable using the present measurement system employing a LUNA OVA, marked with a black dotted line.

Focussing on the variations in shift value for different grating strengths, a weaker maximum reflectivity is shown to result in a smaller valley shift. In this case, the maximum reflectivity was reduced to 25%. In comparison to the 96% reflectivity grating system, the wavelength shifts for the valley's lowest point was reduced, being to a greater degree as the shift's magnitude increases (23% reduction for methanol, 20% reduction for acetone and 13% reduction for ethylene-glycol). This suggests that the strength of the grating affects the degree of the valley's shift.

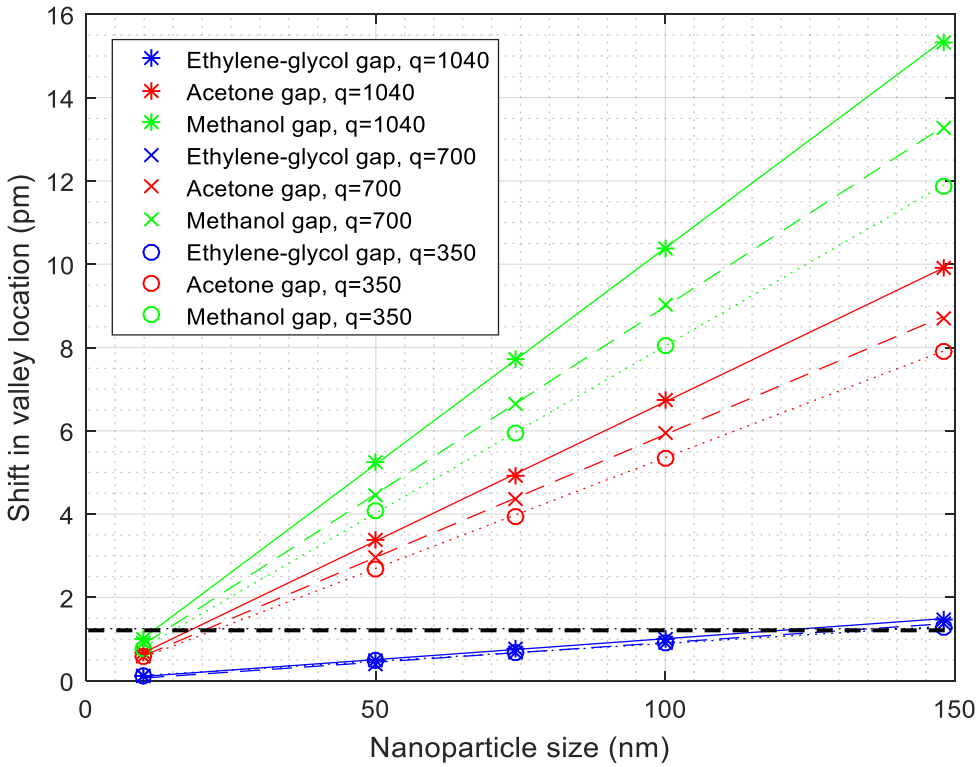

Fig. 3.25: A comparison of the magnitude of wavelength shifts for the lowest point of the valley for systems with a gap medium of ethylene-glycol, acetone and methanol with varying grating strengths. Starred points indicate data from a grating system with a coupling coefficient of 1040 (refl=95.73%), while points marked with a cross indicate data from a grating system with a coupling coefficient of 700 (refl=78.66%). Data points circled points indicate a coupling coefficient of 350 (refl=24.67%). A shift of 1.25pm is observable using the present measurement system employing a LUNA OVA, marked with a black dotted line.

The implications of the grating system's reflectivity on the magnitude of the shift in the valley's location creates the need to take this too into account in a physical system. Fig. 3.24 demonstrates that a side effect of this variable is that a weaker grating system strength requires larger nanoparticles to result in the same shift, therefore reducing the sensitivity of the detection system to smaller nanoparticles. Should the gap medium be chosen to maximise the difference in effective refractive index, then this reduction in sensitivity becomes less of an issue than for a poorly chosen medium (in the example of a HIV virion, the poor choice is ethylene-glycol, due to the refractive index difference of 0.027 in comparison to 0.117 for methanol. Though this may not always be the case for nanoparticles).

The simulations up to this point have demonstrated that the detection of a nanoparticle of this size is likely to be possible with two uniform gratings. The simulations have their limitations though, so replicating the setup on other software using the knowledge gained here should confirm whether a single particle, as opposed to a nanoparticle-sized length of medium can be detected as well. Details on this have been discussed in section 3.7.2.2.

3.7.5. Methods to fabricate the nanoparticle detection system

The process of generating a physical representation of the modelled system makes use of aspects already explored in literature. The fabrication of the initial grating system is easily possible using a simple manipulation of a uniform grating design to include a gap of the relevant size. This length, as explored in section 3.6, may be chosen to create a spectrum of a desired form, preferably a simpler Fabry-Perot form to simplify measurements.

Papers on the task of boring a hole into optical fibre have demonstrated the ability to carve structures into fibre in order to contain a fluid [77, 84], exploring a variety of forms for the microchannels. The technique employed makes use of translating a fibre sample though the path of a femtosecond laser beam, inscribing the desired channel length in one plane and repeating the process layer by layer through the fibre. Following inscription, the fibre is etched in an ultrasonic bath comprised of a 5% hydrofluoric acid solution. This second step selectively removes the areas modified by the femtosecond laser, physically creating the bored holes described above [77] and allowing the chosen medium to be inserted into the hole.

With present advancements in this area, an example bored hole is 5.6µm at one end and 2.9µm at the opposite end. This variation is due to the defocusing of the laser beam spot as it penetrates the curved surface of the fibre. By rotating the fibre by 180° and resuming the etching, this taper can be adjusted to reduce the impact of this defocusing, leaving a more acceptable minimum width at the centre point of the fibre. However, the more complex setup required to ensure an exact half rotation would require a setup specialised for the purpose of boring a micrometre sized hole through fibre. The impact of this effect was reduced in the literature by use of a flat glass slip in front of the fibre and an oil matching the index of the fibre cladding set between. This simulates a flat edge to the fibre, reducing the effect of transmission through a curved surface.

Within the simulation described in this chapter, the bored hole is assumed to be 1µm in diameter which is smaller than the sizes inscribed in literature. A focussed beam size of 1.5µm is described in [76], which suggests this diameter may be possible should the inscribing beam width be appropriately attained, though it is possible to make use of a larger diameter should a 1µm hole not be possible at the time of fabrication. A larger radius for the hole would simply make use of the above investigation into the width of the hole, considering the change in phase and the resulting shift in the base valley location in the spectrum. A diameter attaining a valley close to the design wavelength of the grating may not fall on an exact micrometre increment, though simulations of this length in the vicinity of the desired diameter will provide a good value for the variable.

3.7.6. Discussion of simulation results

The results described above follow the logic of the theory, with variations in both the medium of the hole and of the nanoparticle itself leading to a shift in the wavelength the central valley is located at. This in turn supports the use of such a system as a nanoparticle detector in the case that measurement equipment is available to detect the small shifts that result from the particles.

However, issues arise with regards to the accuracy of the calculations involved. As the simulation method is based on coupled mode theory and the transfer matrix method, the previously explained replication of the hole and nanoparticle as slabs leads to an unrealistic magnitude for the shift in the valley wavelength. A physical replication of the system would likely produce much smaller values for this shift, which may not be detectable with equipment like the LUNA optical vector analyser utilised in this thesis. As such, the use of this investigation is limited to proving a set of patterns with respect to how various parameter changes affects the valley shift relative to other parameter changes.

The demonstration that a nanoparticle of a given size creates a larger shift when there is a larger difference in refractive index between the particle and the surrounding medium is of value for inspecting later simulations that resolve the slab issue. As such, the trends in shift sizes overviewed in section 3.7.4 hold use in future investigations to guide models and as proof of the behaviour of the valley shifts as relative parameters change.

Other observations of interest include the increase in valley shift with the use of stronger FBGs in the surrounding grating system. The cause for this curious addition to the parameter list requires more research to fully determine and suggests that further aspects of the detection system that are considered to not have an effect on the valley shift may be worth consideration. This also reinforces the requirement to have a full representation of the base system's spectrum before a nanoparticle is presented. The use of a sample of the chosen gap medium without any nanoparticles would be ideal for this purpose not only for gaining a thorough representation of the medium itself but also as a counter to any change in the hole's form resulting from damage whilst cleaning.

The COMSOL simulations presented in section 3.7.2.2 show promise in enabling a more physically accurate representation of the area immediately surrounding the bored hole, allowing for mode calculations for a range of wavelengths to be acquired. The use of SMF28 fibre reduces this calculation to require only a single mode, simplifying the model and reducing runtime. The model presented in Appendix 4 itself is in need of further development, due to time constraints based on the trial version of COMSOL, and in its current state shows an alteration to the mode prior to its entrance of the bored hole. This may be the result of reflection or scattering from one side of the hole, though the focus of that particular model was on transmission, with no time to identify the root of the presumed reflection aspect of the model.

One aspect of interest to observe in a working model is the relationship between the nanoparticle size and the induced valley shift for a simulation more accurately modelling the physics, rather than relying on slabs. Given the different area and volume of a true nanoparticle in comparison to the slab employed in the MATLAB simulations, the shift will of course be of a much smaller scale, though given the relationship between radius, area and volume, the change in shift will no longer follow such a linear pattern. This may make smaller nanoparticles more difficult to observe whilst allowing for more informative measurements of larger particles with respect to smaller ones. This would also be of interest with non-spherical nanoparticles in terms of how their orientation affects the optical path and therefore the spectrum. Based on the expectations presented above, it may be more possible for larger nanoparticles to be used for observations such as for electromagnetic field detection.

The likelihood of a physical nanoparticle detection system using a LUNA OVA is therefore reduced due to the resolution possible with such a spectrum analyser. However, recent work within AIPT shows promise in spectral observations using ensemble-averaged homodyne detection [85]. The sub-picometre potential for resolution would greatly assist in observing the small shifts involved in this nanoparticle detector, with the added advantage of such a nanoparticle detector to demonstrate the capabilities of the new spectral analyser.

Together these two sets of simulations show that there is a pattern to the shift in the wavelength the valley appears at which is based on several factors including the relative refractive index difference between the nanoparticle and the surrounding medium as well as the size of the nanoparticle. While the pattern supports the theory presented above, the calculated numbers for the MATLAB model, with respect to the exact valley shift, is likely of an enlarged scale, requiring further investigation to find the true shift values beyond that of the general pattern observed. The COMSOL models require further time and work to ensure a true representation of the physics and to ensure its runtime efficiency is acceptable for repeated use.

3.7.7. Conclusion to nanoparticle detection system

The spectral changes resulting from a nanoparticle located within a fibre grating system's gap shows potential for being observed via the use of an optical vector analyser. The main candidate for observation is the lowest point in the valley that forms due to the Fabry-Perot effect between two gratings. Due to changes in the phase caused by an alteration in either the refractive index or length of the gap, as well as for distinct sections along a gap of a stable length, the wavelength of this valley shifts by a measurable amount, assuming the nanoparticle is above a certain size.

The minimum size for a nanoparticle to cause a detectable shift on a LUNA OVA within the described MATLAB simulation is in the region of 12nm, given a refractive index of 0.06 above the gap medium. This minimum size should vary depending on the difference in refractive index between the gap medium and the nanoparticle, with a smaller difference in refractive index requiring a larger nanoparticle to be observable. Given the range of sizes of the virion nanoparticles this system is seeking to test the detectability of being from 10nm to around 150nm, all but the smallest nanoparticles stand a good chance of detection with a gap medium of acetone or a medium of a smaller refractive index. The use of a gap medium with a lower refractive index, such as methanol, with lead to a relatively larger shift and therefore the ability to detect smaller particles. In the case of methanol, the minimum detectable size is reduced to 12nm, down from 19nm for an acetone gap. A potential method for measuring these small shifts was recently proposed, in which sub-picometre resolution was gained via ensemble-averaged homodyne detection [85]. This highlights one of the key issues with this method for nanoparticle detection; the requirement for highly sensitive spectral analysers which are often also highly expensive. The development of ensemble-averaged homodyne detection will likely be an expensive spectral analysis technique once it is complete and has been tested, though the resolution it provides is of key importance to this nanoparticle detection technique. The further development of high resolution spectral analysers will bring down this cost over time, though it remains an expensive requirement for the nanoparticle detection system's operation.

The change in sensitivity based on the relative refractive indexes of the gap medium and the nanoparticle shows the importance of knowing the refractive index of the medium precisely, which can be a challenge for biological media, such as blood. Publications on this topic have been made, but the refractive index of whole blood in a range including 1550nm has not yet been seen. As of

writing, values for within the ranges of 370-850nm [83] and 2-15µm [86] have been noted, with the measurements for between these two ranges being sought. Methanol was made use of in these simulations as its refractive index is in close vicinity of blood's effective refractive index for regions either side of 1550nm.

An alternative location for observing the changes in spectrum is the maximum of the smaller peak located beside the valley. This decreases as the lowest point of the valley moves further from the central wavelength of the grating system, though for small shifts on a physical fibre system, this may be difficult to ascertain whether this shift is due to a nanoparticle or from another source, as the maximum amplitude of this peak is dependent on more factors than the wavelength location of its peak. Due to this change being measured through the amplitude of the transmission or reflection spectrum rather than a wavelength shift, it is more observable with a logarithmic plot.

This chapter also defines a concept for resolving the issue of physical accuracy around the bored hole by strategic use of a different modelling method. Replication of the area surrounding the bored hole using a simulation package such as COMSOL will enable a physically realistic model of the transmission through the system and therefore the spectrum at a range of wavelengths. Care must be taken with this simulation though as at present, COMSOL is prone to taking extended periods of time to simulate short fibre sections, a task which is better fulfilled by the established MATLAB model the above research is mainly performed in. A combination of these methods will allow for a physically accurate representation of the detection system whilst reducing runtime issues that appear to be prevalent with COMSOL's fibre grating simulations. By defining an efficient and reliable method for transferring data between MATLAB and COMSOL, flexibility regarding the structure of the detection system will allow for more detailed replications of the physical setup and in variations in more parameters. This will also enable a thorough investigation of the effects of orientation of a non-spherical nanoparticle as well as the position of one or more nanoparticles.

Overall, it can be seen that a nanoparticle detector based on the form of a pair of gratings with a bored hole between them is feasible due to alterations to the form of the spectra. A particular location of interest, the valley that occurs within the area of what would be the central peak, is observed to undertake a wavelength shift dependant on variables in the bored hole and nanoparticle. A number of trends within the wavelength the central valley have been recorded based on the size of the nanoparticle, the difference in the relative refractive indexes of the nanoparticle and the medium within the hole it is suspended in as well as the strength of the gratings that forms part of the detection system. This last variable will remain constant for a physical replication of the simulations but is worth noting for each detector fabricated. The aspects demonstrated in this chapter lay down some foundations for future research into nanoparticle detectors via this technique and show promise in such a system being worth fabrication.

3.8. Chapter conclusion

This chapter has overviewed the processes employed to fabricate gratings described in this thesis as well as work undertaken for potential advancements not only to the fabrication system, but also for grating based systems for sensing applications.

A description of the fabrication system employed before the movement to new laboratories and how it has been improved for fabrication in the new location has been provided, focussing on aspects added over this interim period. The development of a feedback system to automatically detect errors in fabrication in comparison to the designed grating and to make alterations to correct

these errors will enable much more accurate gratings to be fabricated, matching desired spectral patterns. The inclusion of an alternate inscription head, itself on an extended translation stage will also increase the variety of gratings the system is capable of fabricating. Together, these two main areas of progression will increase both the potential gratings that can be produced for research and the quality of these gratings for improved results of the research they are used within.

Progress has also been made in the simulation of a potential nanoparticle detector. Although limitations in the simulations exist, observed patterns in the wavelength shift of a distinct area of the spectrum have been noted, with relative comparisons in these shifts showing promise for a physical nanoparticle detection system. Possible improvements to the simulations are also discussed, particularly to counter the limitations of the MATLAB simulation with respect to the shape of the bored hole within the fibre and the nanoparticles themselves. With the discussed adaptations to the simulation, a truly accurate representation of the transmitted spectra can be attained, which will guide the fabrication of such detectors and methods for gaining information on the nanoparticles.

Overall, progress in both the improvement of the fabrication system as well as in simulations for proposed applications that are possible with the improved fabrication system have been made. Advancements in the capabilities of the fabrication system will be of great use to a variety of research, providing varied gratings that are accurate to the designs and intended spectra with fewer iterations of the gratings required before this is met. The nanoparticle detector simulations highlight a potential new piece of research to test the capabilities of not only the fabrication system, but of other areas such as the precise boring of holes through an optical fibre.

4. Conclusions and future work

4.1. Suggested future work

Following the work presented in this thesis, a number of areas that present further attention and investigations are apparent. Primarily, these focus on a continuation of the concepts and work performed above, though a few additional points may also be made.

Whilst a method for simulating a nanoparticle detector based off the phase shift induced by a microchannel has been developed within this thesis, a number of improvements to it have been highlighted. Improvements to the simulation to more precisely model the effects of the microchannel and nanoparticle presence, in line with those investigated using COMSOL, would benefit the simulation and allow for a more reliable analysis of the effects of nanoparticle presence. An integration of a more physically accurate representation of the microchannel region with a swift calculation of the surrounding grating system would greatly benefit the prospect of such a nanoparticle detection technique though increased simulation accuracy. In addition, progression in more precise spectral interrogation techniques, such as the above mentioned Ensemble-averaged Homodyne detector, will be of use once a physical version of the simulated system can be tested. A spectral interrogation system of a lower cost would also be beneficial, as the present system's reliance on expensive measurement hardware is a present drawback.

With respect to the fabrication system, future work can be split into two sections: that which is in need of performing, and that which is suggested for continuation of research in this work. Aspects such as continued work on setting up the 1m inscription system, including control over the translation stage and integration of the interferometer inscription head, as well as final testing and integration of the inscription feedback system will be required regardless of suggestions made in this section. Regarding suggested progress of work performed in this thesis, optional aspects such as an automated process for aligning the interferometer head with respect to the fibre could be performed. The present control software for the rotation stages included in the interferometer head include an indicator for the beam overlap position, which may be made use of for such an addition.

Of interest for adding to the fabrication system is also the capability for reliably fabricating multi-core gratings which will, once the fabrication system is fully functional, likely require a small number of changes. These requirements include a method to ensure precise control over any rotation of the fibre, especially the twist in the fibre due to the respective rotation at either end. Such work has not been described in detail above, but may be required for future fabrications.

4.2. Thesis conclusion

The research covered within this thesis has developed the in-house FBG fabrication system through the addition of new aspects to the system. The development of a method to automate the monitoring of a grating during inscription, as part of a larger feedback system will enable the fabrication of gratings that more closely align to the original design. The minimising of random errors during inscription via monitoring of the grating's formation will also reduce the number of iterations required to fabricate a grating of a high enough quality for research purposes. The inclusion of an optional interferometer inscription head for use in place of the present phase mask inscription head in combination with the feedback system will also present the option for greater variety in potential gratings fabricated by this one system, with the advantages off the feedback process. Such an example is the mounting of the interferometer head on a translation stage that will allow for gratings of up to 1m in length, increasing from the previous maximum of 10cm. The

completion of the fabrication system's setup will enable testing of these aspects to begin and further development of these new functions to ensure a smooth integration of them into the existing system. Once fully tested, the system's capabilities will be able to be fully compared to that of the former system.

During the elongated time-frame for the setup of the new labs, an investigation was held into the potential for a nanoparticle detector that could be inscribed by the fabrication system upon its completion. Simulations of such a detector were performed, identifying key parameters that require attention in a physical detector of this form. Aspects such as the nanoparticle's radius and the refractive index difference between the nanoparticle and its surrounding medium were found to affect the shift of a valley within the transmission spectrum. Therefore, it can be concluded that the shift in this area of the spectrum can be used to identify the presence of a nanoparticle and information on its size or refractive index. Limitations within the simulation were identified, with possible resolutions of these being sought via the use of other software. In particular, the use of COMSOL for simulating the area in the vicinity of the system's microchannel showed potential. Future work on the nanoparticle detector simulations may revolve around the implementation of COMSOL for representing this section of the detector, combined with MATLAB's grating simulations, to provide the benefits of both whilst also tending to the weaknesses of both methods.

Together, the improvements to the fabrication system and the potential for a new nanoparticle detector will enable a development of the variety and quality of research topics within AIPT. Further research into the nanoparticle detection system in particular shows promise, in combination with research into higher resolution spectrum analysers, not only for simulation techniques but also for testing the capabilities of the improved fabrication system.

References

[1] K. O. Hill, Y. Fujii, D. C. Johnson, and B. S. Kawasaki, "Photosensitivity in optical fibre waveguides - Application to reflection filter fabrication," (in English), *Applied Physics Letters,* Article vol. 32, no. 10, pp. 647-649, 1978.

[2] J. Hecht, *City of light: the story of fiber optics*. Oxford University Press, 2004.

[3] S. W. Martin, *Historical facts about glass!* 2001.

[4] Y. Sasaki and Y. Ohmori, "Phase-matched sum-frequency light generation in optical fibers," (in English), *Applied Physics Letters,* Article vol. 39, no. 6, pp. 466-468, 1981.

[5] J. Stone, "Photorefractivity in GeO2-doped Silica fibres," (in English), *Journal of Applied Physics,* Article vol. 62, no. 11, pp. 4371-4374, Dec 1987.

[6] J. M. Senior and M. Y. Jamro, *Optical Fiber Communications: Principles and Practice*. Pearson Education, 2009.

[7] G. P. Agrawal, *Nonlinear Fiber Optics*. Academic Press Inc, 1989.

[8] R. Kashyap, *Fibre Bragg gratings*, 2nd ed ed. London, United Kingdom: Elsevier, 2010.

[9] T. Erdogan, "Cladding-mode resonances in short- and long-period fiber grating filters," (in English), *Journal of the Optical Society of America a-Optics Image Science and Vision,* Article vol. 14, no. 8, pp. 1760-1773, Aug 1997.

[10] A. Othonos, "Fiber Bragg gratings," (in English), *Review of Scientific Instruments,* Review vol. 68, no. 12, pp. 4309-4341, Dec 1997.

[11] R. I. Laming, M. N. Zervas, and E. Inst Elect, "Fibre Bragg gratings and their applications," in *11th International Conference on Integrated Optics and Optical Fibre Communications / 23rd European Conference on Optical Communications (IOOC-ECOC 97)*, Edinburgh, Scotland, 1997, EDISON: Inst Electrical Engineers Inspec Inc, 1997, pp. 81-83.

[12] T. Erdogan, "Fiber grating spectra," (in English), *Journal of Lightwave Technology,* Article vol. 15, no. 8, pp. 1277-1294, Aug 1997.

[13] J. Canning, "Fibre gratings and devices for sensors and lasers," *Laser & Photonics Reviews,* vol. 2, no. 4, pp. 275-289, Aug 2008.

[14] A. Othonos and K. Kalli, *Fibre Bragg Gratings: Fundamentals and applications in Telecommunications and Sensing*. Artech House, Inc, 1999.

[15] J. L. Archambault, L. Reekie, and P. S. J. Russell, "100-percent reflectivity Bragg reflectors produced in optical fibres by single eximer-laser pulses," *Electronics Letters,* vol. 29, no. 5, pp. 453-455, Mar 1993.

[16] L. Dong and W. F. Liu, "Thermal decay of fiber Bragg gratings of positive and negative index changes formed at 193 nm in a boron-codoped germanosilicate fiber," *Applied Optics,* vol. 36, no. 31, pp. 8222-8226, Nov 1997.

[17] T. Duthel, S. L. Jansen, M. Otto, P. M. Krummrich, and C. G. Schaffer, "Tunable all-fibre delay line filter for residual dispersion compensation in 40 Gbit/s systems," *Electronics Letters,* vol. 40, no. 20, pp. 1291-1293, Sep 2004.

[18] C. S. Cheung, "An investigation of chirped fibre Bragg gratings Fabry-Perot interferometer for sensing applications," PhD, Cranfield University School of Engineering, 2005.

[19] B. Snow *et al.*, "UV-written planar chirped Bragg gratings for use in dispersion management.," presented at the European Conference on Integrated Optics (ECIO) 2010, 2010.

[20] D. Tosi, "Review of Chirped Fiber Bragg Grating (CFBG) Fiber-Optic Sensors and Their Applications," *Sensors,* vol. 18, no. 7, Jul 2018, Art no. 2147.

[21] G. P. Agrawal and S. Radic, "Phase-shifted fibre Bragg gratings and their applications for wavelength demultiplexing," *Ieee Photonics Technology Letters,* vol. 6, no. 8, pp. 995-997, Aug 1994.

[22] Y. Liu, "Advanced fiber gratings and their applications," PhD, Aston University, 2001.

[23] D. Uttamchandani and A. Othonos, "Phase shifted Bragg gratings formed in optical fibres by post-fabrication thermal processing," *Optics Communications,* vol. 127, no. 4-6, pp. 200-204, Jun 1996.
[24] J. Canning and M. G. Sceats, "Pi-phase-shifted periodicdistributed structuresin optical fibres by UV processing," *Electronics Letters,* vol. 30, no. 16, pp. 1344-1345, Aug 1994.
[25] D. C. J. Reid, C. M. Ragdale, I. Bennion, D. J. Robbins, J. Buus, and W. J. Stewart, "Phase-shifted Moire grating fibre resonators," *Electronics Letters,* vol. 26, no. 1, pp. 10-11, Jan 1990.
[26] Y. Liu, "Advanced fiber grat ings and their applications," PhD, Aston University, 2001.
[27] L. Zhang, K. Sugden, I. Bennion, and A. Molony, "Wide-stopband chirped fibre Moire grating transmission filters," *Electronics Letters,* vol. 31, no. 6, pp. 477-479, Mar 1995.
[28] S. Legoubin *et al.*, "Formation of Moire grating in core of germanosilicate fibre by transverse holographic double exposure," (in English), *Electronics Letters,* Article vol. 27, no. 21, pp. 1945-1946, Oct 1991.
[29] R. Min, C. Marques, O. Bang, and B. Ortega, "Moire phase-shifted fiber Bragg gratings in polymer optical fibers," *Optical Fiber Technology,* vol. 41, pp. 78-81, Mar 2018.
[30] Y. Liu, L. Zhang, W. Zhang, J. A. R. Williams, and Bennion, I, "Investigation of H_2 in- and out-diffusion impact on long-period grating devices," presented at the *Conference on Lasers and Electro-Optics*, 1999.
[31] X. W. Shu, L. Zhang, and I. Bennion, "Sensitivity characteristics near the dispersion turning points of long-period fiber gratings in B/Ge codoped fiber," (in English), *Optics Letters,* Article vol. 26, no. 22, pp. 1755-1757, Nov 2001.
[32] C. Fernandez-Valdivielso, I. R. Matias, and F. J. Arregui, "Simultaneous measurement of strain and temperature using a fiber Bragg grating and a thermochromic material," (in English), *Sensors and Actuators a-Physical,* Article vol. 101, no. 1-2, pp. 107-116, Sep 2002, Art no. Pii s0924-4247(02)00188-7.
[33] J. G. Chen, Q. W. Liu, X. Y. Fan, and Z. Y. He, "Sub-Nano-Strain Multiplexed Fiber Optic Sensor Array for Quasi-Static Strain Measurement," (in English), *Ieee Photonics Technology Letters,* Article vol. 28, no. 21, pp. 2311-2314, Nov 2016.
[34] D. Tosi *et al.*, "Towards inline spatially resolved temperature sensing in thermal ablation with chirped fiber Bragg grating," in *IEEE International Symposium on Medical Measurements and Applications (MeMeA)*, Benevento, ITALY, 2016, 2016, pp. 441-446.
[35] D. Kinet *et al.*, "Proof of Concept for Temperature and Strain Measurements With Fiber Bragg Gratings Embedded in Supercontainers Designed for Nuclear Waste Storage," (in English), *Ieee Transactions on Nuclear Science,* Article vol. 63, no. 3, pp. 1955-1962, Jun 2016.
[36] Y. J. Rao, D. J. Webb, D. A. Jackson, L. Zhang, and I. Bennion, "Optical in-fibre Bragg grating sensor systems for medical applications," (in English), *Journal of Biomedical Optics,* Article vol. 3, no. 1, pp. 38-44, Jan 1998.
[37] C. A. F. Marques, A. Posproi, D. Sáez-Rodríguez, K. Nielson, O. Bang, and D. J. Webb, "Aviation Fuel Gauging Sensor Utilizing Multiple Diaphragm Sensors Incorporating Polymer Optical Fiber Bragg Gratings," vol. 16, ed. IEEE Sensors Journal: IEEE, 2016, pp. 6122-6129.
[38] J. X. Cai *et al.*, "49.3 Tb/s Transmission Over 9100 km Using C plus L EDFA and 54 Tb/s Transmission Over 9150 km Using Hybrid-Raman EDFA," (in English), *Journal of Lightwave Technology,* Article vol. 33, no. 13, pp. 2724-2734, Jul 2015.
[39] M. Stern, J. P. Heritage, and E. W. Chase, "Grating compensation of 3rd-order fibre dispersion," (in English), *Ieee Journal of Quantum Electronics,* Article vol. 28, no. 12, pp. 2742-2748, Dec 1992.
[40] J. A. R. Williams, I. Bennion, K. Sugden, and N. J. Doran, "Fiber dispersion compensation using a chirped in-fiber Bragg grating," (in English), *Electronics Letters,* Article vol. 30, no. 12, pp. 985-987, Jun 1994.

[41] R. Kashyap, S. V. Chernikov, P. F. McKee, and J. R. Taylor, "30ps chromatic dispersion compensation of 400fs pulses at 100Gbits/s in optical fibers using an all-fibre photoinduced chirped reflection grating," (in English), *Electronics Letters,* Article vol. 30, no. 13, pp. 1078-1080, Jun 1994.

[42] N. M. Litchinitser, B. J. Eggleton, and D. B. Patterson, "Fiber Bragg gratings for dispersion compensation in transmission: Theoretical model and design criteria for nearly ideal pulse recompression," (in English), *Journal of Lightwave Technology,* Article vol. 15, no. 8, pp. 1303-1313, Aug 1997.

[43] M. H. Asghari and B. E. D. K. I. R. D. A. N. a. H. D. Jalali, "Demonstration of Analog Time-Bandwidth Compression Using Anamorphic Stretch Transform," in *Frontiers in Optics 2013 Postdeadline*, Orlando, Florida, 2013: Optical Society of America, p. FW6A.2.

[44] M. H. Asghari and B. Jalali, "Anamorphic transformation and its application to time-bandwidth compression," (in English), *Applied Optics,* Article vol. 52, no. 27, pp. 6735-6743, Sep 2013.

[45] M. H. Asghari and B. Jalali, "Experimental demonstration of optical real-time data compression," (in English), *Applied Physics Letters,* Article vol. 104, no. 11, p. 4, Mar 2014, Art no. 111101.

[46] T. Maihara, F. Iwamuro, D. N. B. Hall, L. L. Cowie, A. T. Tokunaga, and A. J. Pickles, "An OH airglow suppressor spectrograph - Design and prospects," in *Conference on Infrared Detector and Instrumentation*, Orlando, Fl, 1993, vol. 1946, BELLINGHAM: Spie - Int Soc Optical Engineering, 1993, pp. 581-586.

[47] J. Bland-Hawthorn *et al.*, "A complex multi-notch astronomical filter to suppress the bright infrared sky," *Nature Communications,* vol. 2, 2011.

[48] J. Bland-Hawthorn, A. Buryak, and K. Kolossovski, "Optimization algorithm for ultrabroadband multichannel aperiodic fiber Bragg grating filters," (in English), *Journal of the Optical Society of America a-Optics Image Science and Vision,* Article vol. 25, no. 1, pp. 153-158, Jan 2008.

[49] S. G. Leon-Saval, T. A. Birks, J. Bland-Hawthorn, and M. Englund, "Multimode fiber devices with single-mode performance," (in English), *Optics Letters,* Article vol. 30, no. 19, pp. 2545-2547, Oct 2005.

[50] S. G. Leon-Saval, A. Argyros, and J. Bland-Hawthorn, "Photonic lanterns: a study of light propagation in multimode to single-mode converters," (in English), *Optics Express,* Article vol. 18, no. 8, pp. 8430-8439, Apr 2010.

[51] D. Noordegraaf, P. M. W. Skovgaard, M. D. Nielsen, and J. Bland-Hawthorn, "Efficient multi-mode to single-mode coupling in a photonic lantern," (in English), *Optics Express,* Article vol. 17, no. 3, pp. 1988-1994, Feb 2009.

[52] A. A. Gbadebo, E. G. Turitsyna, and J. A. R. Williams, "Fabrication of precise aperiodic multichannel fibre Bragg grating filters for spectral line suppression in hydrogenated standard telecommunications fibre," (in English), *Optics Express,* Article vol. 26, no. 2, pp. 1315-1323, Jan 2018.

[53] J. Skaar, "Synthesis and characterization of fiber Bragg gratings," PhD, Institute of Physical Electronics, 2000.

[54] A. V. Buryak and D. Y. Stephanov, "Correction of systematic errors in the fabrication of fiber Bragg gratings," *Optics letters,* vol. 27, no. 13, pp. 1099-1101, 2002.

[55] G. A. Miller, G. M. H. Flockhart, and G. A. Cranch, "Technique for correcting systematic phase errors during fibre Bragg grating inscription," (in English), *Electronics Letters,* Article vol. 44, no. 24, pp. 1399-1400, Nov 2008.

[56] A. A. Gbadebo, "Advanced method of fabricating fibre Bragg gratings," PhD, Aston Institute of Photonic Technologies, Aston University, 2015.

[57] G. Meltz, W. W. Morey, and W. H. Glenn, "Formation of Bragg gratings in optical fibres by a transverse holographic method," (in English), *Optics Letters,* Article vol. 14, no. 15, pp. 823-825, Aug 1989.
[58] P. Gasior, T. Osuch, and L. Lewandowski, "Inscription of fiber Bragg gratings with wavelength flexibility using phase mask interferometer in Talbot's configuration," in *14th Symposium on Photonics and Web Engineering*, Wilga, POLAND, 2004, vol. 5775, 2005, pp. 216-221.
[59] J. Albert *et al.*, "Photosensitivity in Ge-doped silica optical waveguides and fibers with 193-nm light from an ArF excimer laser," *Optics Letters,* vol. 19, no. 6, pp. 387-389, 1994/03/15 1994.
[60] M. Matsuhara and K. O. Hill, "Optical-Waveguide Band-Rejection Filters- Design," (in English), *Applied Optics,* Article vol. 13, no. 12, pp. 2886-2888, 1974.
[61] M. J. Cole, W. H. Loh, R. I. Laming, M. N. Zervas, and S. Barcelos, "Moving fibre/phase mask-scanning beam technique for enhanced flexibility in producing fibre gratings with uniform phase mask," *Electronics Letters,* vol. 31, no. 17, pp. 1488-1490, 1995.
[62] R. Kashyap, A. Swanton, and D. J. Armes, "Simple technique for apodising chirped and unchirped fibre Bragg gratings," *Electronics Letters,* vol. 32, no. 13, pp. 1226-1228, Jun 1996.
[63] Y. Liu, J. J. Pan, and C. Gu, "Novel fiber Bragg grating fabrication method with high-precision phase control," (in English), *Optical Engineering,* Article vol. 43, no. 8, pp. 1916-1922, Aug 2004.
[64] C. Sima *et al.*, "Phase modulated direct UV grating writing technique for ultra-wide spectrum planar Bragg grating fabrication," in *17th Photonics West Conference on Integrated Optics - Devices, Materials, and Technologies*, San Francisco, CA, 2013, vol. 8627, BELLINGHAM: Spie-Int Soc Optical Engineering, 2013.
[65] M. Gagne, S. Loranger, J. Lapointe, and R. Kashyap, "Fabrication of high quality, ultra-long fiber Bragg gratings: up to 2 million periods in phase," (in English), *Optics Express,* Article vol. 22, no. 1, pp. 387-398, Jan 2014.
[66] D. J. Mccarron. (2007, 20/02). *A guide to acousto-optic modulators* "http://jila1.nickersonm.com/papers/A%20Guide%20to%20Acousto-Optic%20Modulators.pdf".
[67] J. Sapriel, S. Francis, and B. Kelly, *Acousto-optics*. Wiley, 1979, p. 126.
[68] R. S. Dahiya and M. Valle, *Robotic Tactile Sensing*. Springer Netherlands, 2013.
[69] X. P. Zhang, Z. Guo, Y. Y. Shan, Z. H. Sun, S. Y. Fu, and Y. X. Zhang, "Enhanced Phi-OTDR system for quantitative strain measurement based on ultra-weak fiber Bragg grating array," (in English), *Optical Engineering,* Article vol. 55, no. 5, p. 6, May 2016, Art no. 054103.
[70] S. R. Abdullina and A. A. Vlasov, "Suppression of side lobes in the fiber Bragg grating reflection spectrum," *Optoelectronics, Instrumentation and Data Processing,* vol. 50, no. 1, pp. 75-86, 2014.
[71] M. Al-Khateeb, M. E. McCarthy, M. D. G. Pascual, F. Smyth, and A. D. Ellis, "Optimization of Parametric Comb Generation Using Interferometric Wavelength Selective Switch," in *Conference on Lasers and Electro-Optics*, San Jose, California, 2017: Optical Society of America, p. JW2A.31.
[72] N. M. Faiyaz, A. I. Omi, M. Faisal, and Ieee, "Optimization of Apodization Profile of Chirped Fiber Bragg Grating for Chromatic Dispersion Compensation Dispersion Compensation Using Chirped Apodized FBG," in *1st International Conference on Electrical Engineering and Information and Communication Technology (ICEEICT)*, Dhaka, BANGLADESH, 2014, NEW YORK: Ieee, 2014.
[73] M. Gagne and R. Kashyap, "Ultra-long and ultra high quality fibre Bragg gratings," in *Conference on Integrated Optics - Physics and Simulations*, Prague, CZECH REPUBLIC, 2013, vol. 8781, 2013.
[74] A. Gbadebo, E. G. Turitsyna, and J. A. R. Williams, "Experimental Demonstration of Real-time correction of writing errors during Fibre-Bragg grating fabrication," presented at the Bragg

Gratings, Photosensitivity and Poling in Glass Waveguides (BGPP) 2016, Sydney, Australia, 2016.
[75] (08/02/2019). *Metalaser BBO datasheet "https://www.meta-laser.com/uploads/20189763/BBO-Nonlinear-Crystal-Metalaser.pdf"*.
[76] G. C. B. Lee, C. Mou, K. Zhou, and K. Sugden, "Optimization and Characterization of Femtosecond Laser Inscribed In-Fiber Microchannels for Liquid Sensing," *Journal of Lightwave Technology,* vol. 33, no. 12, pp. 2561-2565, 2015.
[77] Y. Lai, K. Zhou, L. Zhang, and I. Bennion, "Microchannels in conventional single-mode fibers," *Optics Letters,* vol. 31, no. 17, pp. 2559-2561, Sep 2006.
[78] A. Layeghi and H. Latifi, "Magnetic field vector sensor by a nonadiabatic tapered Hi-Bi fiber and ferrofluid nanoparticles," (in English), *Optics and Laser Technology,* Article vol. 102, pp. 184-190, Jun 2018.
[79] J. F. Akki, A. S. Lalasangi, K. G. Manohar, P. Raikar, T. Srinivas, and U. S. Raikar, "Detection and determination of manganese concentration in water using a fiber Bragg grating coupled with nanotechnology," *Applied Optics,* vol. 50, no. 32, pp. 6033-6038, Nov 2011.
[80] C. F. Bohren and D. R. Huffman, *Absorption and scattering of light by small particles*. New York: Wiley-Interscience, 2007.
[81] Y. J. Pang, H. N. Song, and W. Cheng, "Using optical trap to measure the refractive index of a single animal virus in culture fluid with high precision," (in English), *Biomedical Optics Express,* Article vol. 7, no. 5, pp. 1672-1689, May 2016.
[82] (30/08/2018). *Corning SMF28 specifications: "http://www.princetel.com/datasheets/smf28e.pdf"*.
[83] H. Li, L. Lin, and S. S. Xie, "Refractive index of human whole blood with different types in the visible and near-infrared ranges," in *Conference on Laser-Tissue Interaction XI - Photochemical, Photothermal, and Photomechanical*, San Jose, Ca, 2000, vol. 3914, BELLINGHAM: Spie-Int Soc Optical Engineering, 2000, pp. 517-521.
[84] G. C. B. Lee, C. B. Mou, K. M. Zhou, and K. Sugden, "Optimization and Characterization of Femtosecond Laser Inscribed In-Fiber Microchannels for Liquid Sensing," (in English), *Journal of Lightwave Technology,* Article; Proceedings Paper vol. 33, no. 12, pp. 2561-2565, Jun 2015.
[85] S. Sugavanam, A. Gbadebo, and E. G. Turitsyna, "Characterization of Disorder Induced Resonances in Fiber Bragg Gratings with Sub-picometer Resolution using Ensemble-averaged Homodyne Detection," presented at the Bragg Gratings, Photosensitivity and Poling in Glass Waveguides and Materials 2018, Zurich, Switzerland, 2018.
[86] D. J. Rowe, D. Smith, and J. S. Wilkinson, "Complex refractive index spectra of whole blood and aqueous solutions of anticoagulants, analgesics and buffers in the mid-infrared," (in English), *Scientific Reports,* Article vol. 7, p. 9, Aug 2017, Art no. 7356.

Appendix

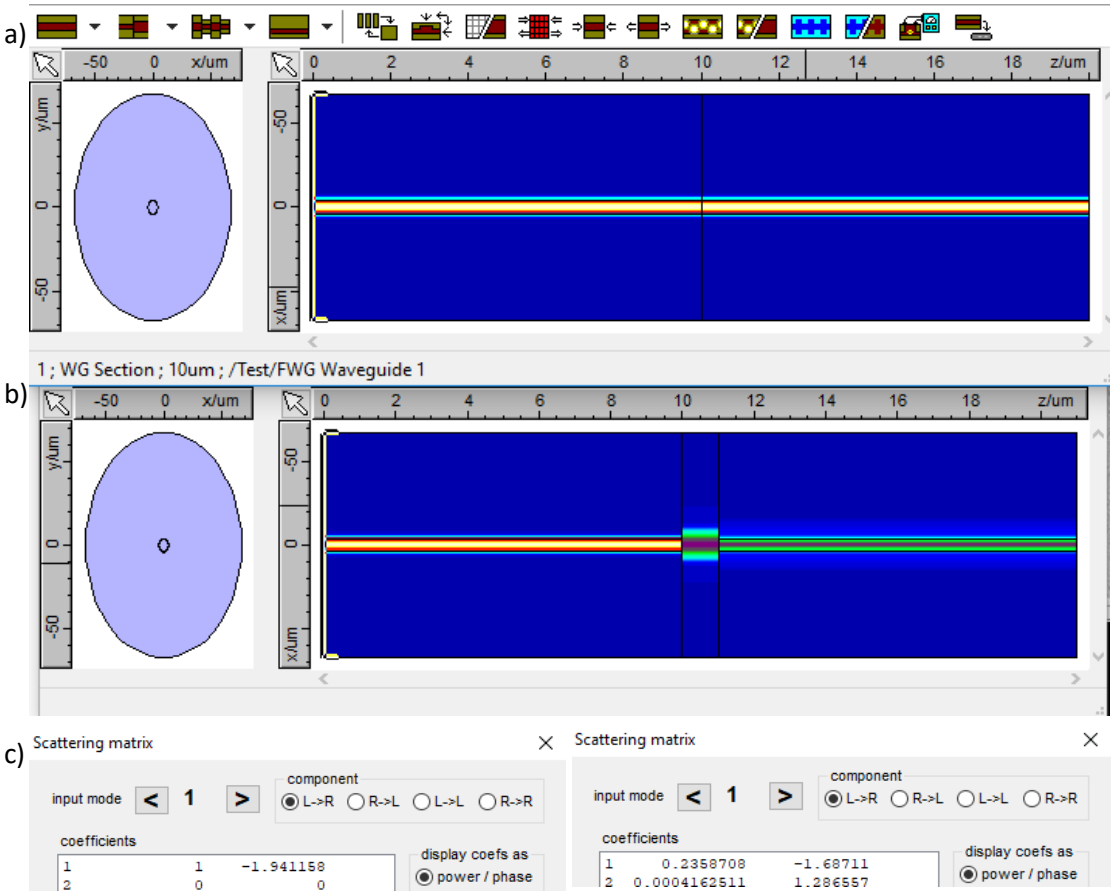

Appendix 1: Visualisation of field profile of a) SMF28 fibre and b) SMF28 fibre with a gap of n=1.61. c) The scattering matrices for the two simulations for transmission from the left of the figures to the right. The first mode displayed shows the normalised transmission (1 for A and 0.236 for B).

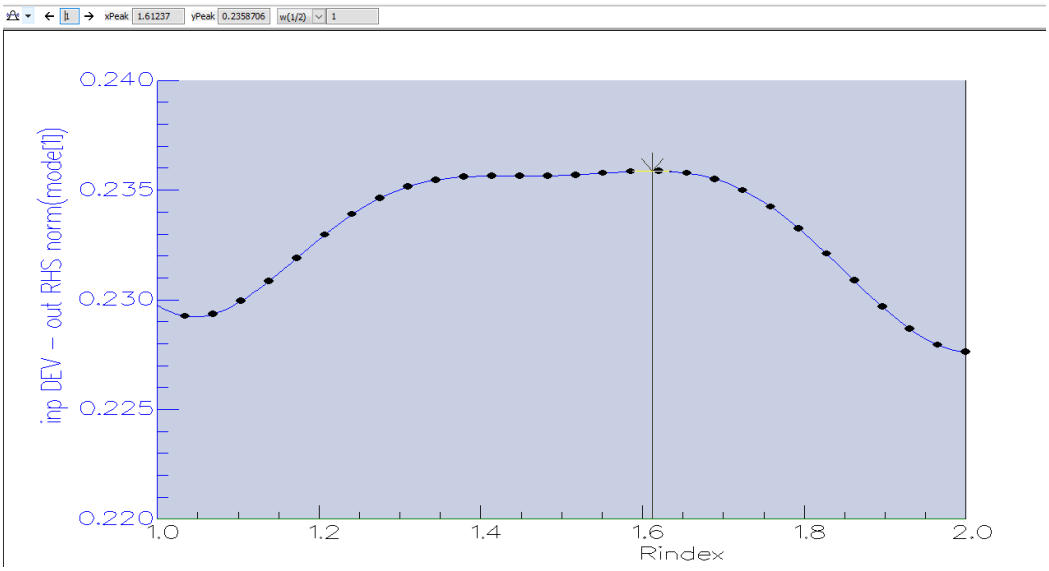

Appendix 2: Plot of transmission values across a gap of varying refractive index. The two peaks are located at 1.61 (marked) and 1.40.

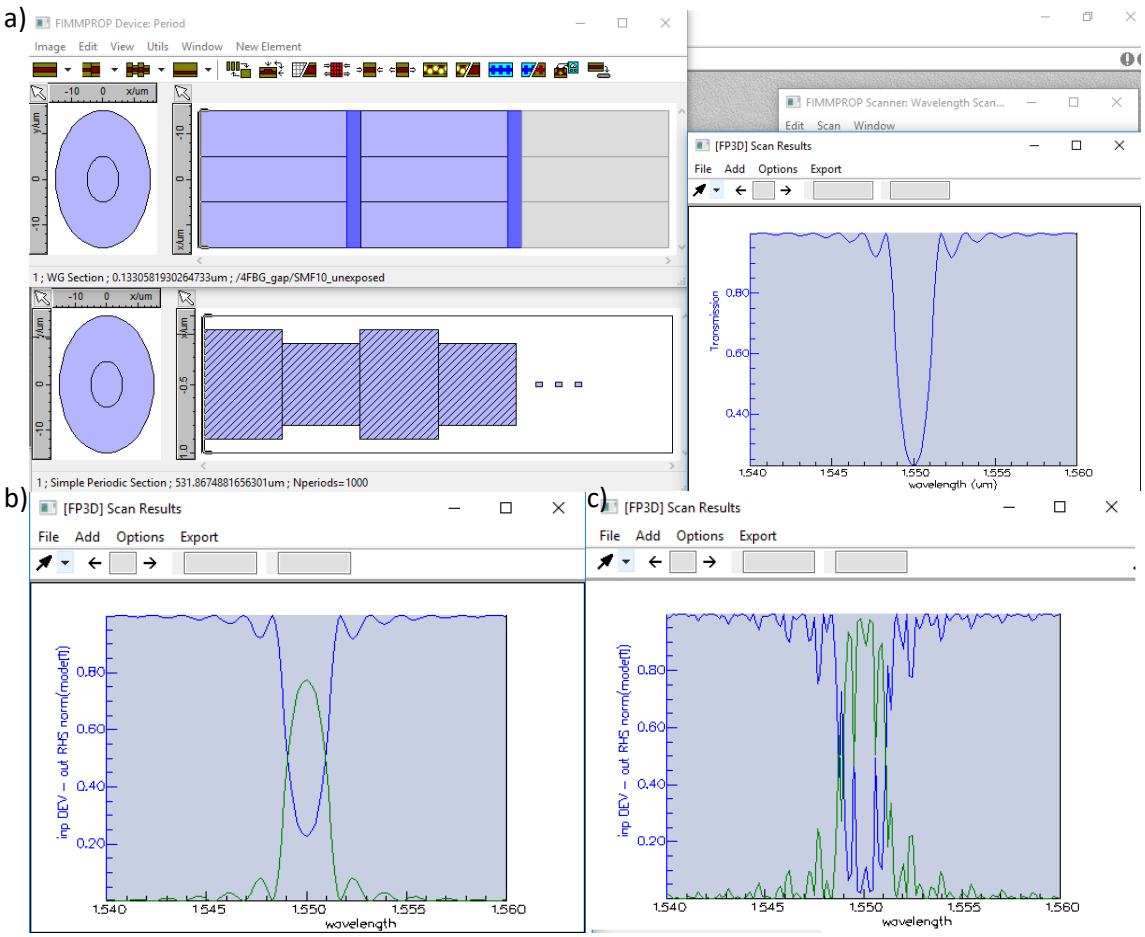

*Appendix 3: Simulated example FBG based on a repetition of (Nperiods * period section). a) Example of a single period (half of an unexposed section, followed by a full exposed section, followed by the second half of an unexposed section. Designed such so that an unexposed section will be at either end of the full system). Below this is FIMMWAVE's display for a repeated period and a transmission profile to the right. b) The transmission (blue) and reflection (green) profiles for a simple FBG as displayed in a). c) The transmission (blue) and reflection (green) profiles for a pair of the previous FBGs placed 1067.38µm (two periods) apart.*

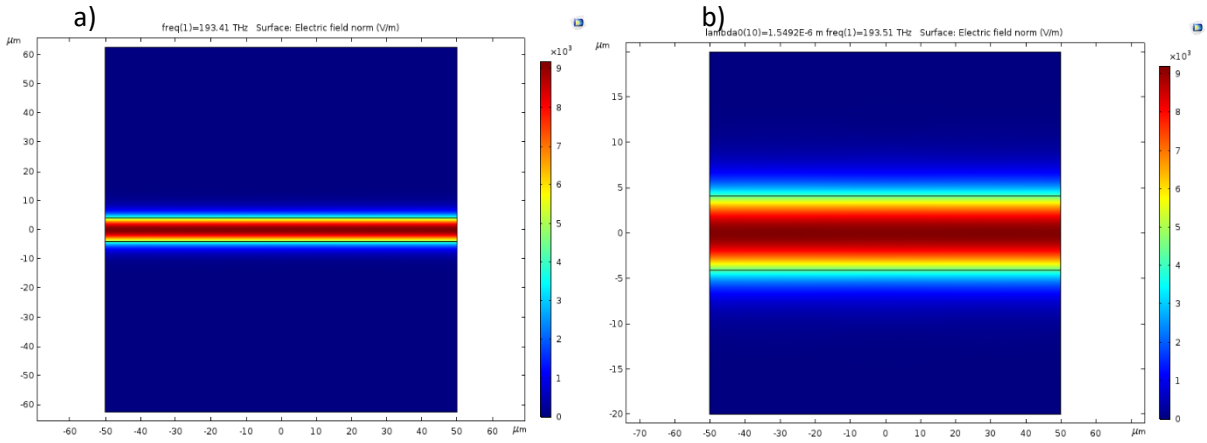

Appendix 4: A simulation of propagation using COMSOL, showing limitation of propagation to the core of the fibre. a) Modelling an SMF28 fibre with the same core and cladding radius as given by the Corning specifications.. b) The same simulation with the cladding radius reduced to 20µm, resulting in a runtime reduction of 87%.